2019 International Symposium of
Research Institute for Electronic Science (RIES)
Hokkaido University &
Center for Emergent Functional Matter Science (CEFMS)
National Chiao Tung University

3-4 December 2019
Hokkaido University International Conference Hall

ABSTRACTS

Jiunn-Yuan LIN

Professor
Institute of Physics
National Chiao Tung University (NCTU)
1001, Ta Hsueh Rd.
Hsinchu 300, TAIWAN
Phone: +886-3-5731653
Email: ago@cc.nctu.edu.tw
Website: http://cpanel-199-19.nctu.edu.tw/~super/

He is a professor of Institute of Physics at National Chiao Tung University (NCTU). He received his Ph.D. in Physics from Stony Brook University in 1995. After working at National Sun Yat-Sen University in Taiwan as a research associate, he joined the faculty of NCTU in 1997. His current research focus on the discovery, creation, and understanding of novel quantum matter.

Selected Publications

1. J.-Y. Lin, Y. S. Hsieh, D. A. Chareev, A. N. Vasiliev, Y. Parsons, and H. D. Yang, "Low temperature specific-heat measurements of a coexistence of isotropic and extended s-wave order parameters in superconducting FeSe single crystals", Physical Review B **84**, 220507(R) (2011).

2. Thanh-Tra Vu, Jhih-Wei Chen, Po-Cheng Huang, Bo-Chao Huang, Ye Cao, Chao-Hui Yeh, Heng-Jui Liu, Eugene A. Eliseev, Anna N. Morozovska, Jiunn-Yuan Lin, Yi-Chun Chen, Ming-Wen Chu, Po-Wen Chiu, Ya-Ping Chiu, Long-Qing Chen, Chung-Lin Wu,* and Ying-Hao Chu, "Ferroelectric control of the conduction at the $LaAlO_3/SrTiO_3$ hetero-interface", Advanced Materials, **25**, 3357-3364 (2013).

3. Y.-J. Chen, M. G. Jiang, C. W. Luo, J.-Y. Lin, K. H. Wu, J. M. Lee, J. M. Chen, Y. K. Kuo, J. Y. Juang, and C. Y. Mou, "Doping evolution of Zhang-Rice singlet spectral weight: A comprehensive examination by x-ray absorption spectroscopy", Physical Review B **88**, 134525 (2013).

4. J. He, P. Shafer, T. R. Mion, V. T. Tra, Q. He, J. Kong, Y.-D. Chuang, W. L. Yang, M. J. Graf, J.-Y. Lin, Y. H. Chu, A. Arenholz, and R.-H. He,* "Observation of a three-dimensional quasi-long-range electronic supermodulation in $YBa_2Cu_3O_{7-x}/La_{0.7}Ca_{0.3}MnO_3$ heterostructure", Nature Communications 7, 10852 (2016).

5. Chih-Wei Luo,* P. C. Cheng, S.-H. Wang, J.-C. Chiang, Jiunn-Yuan Lin, Kaung-Hsiung Wu, Jenh Yih Juang, Dmitriy Chareev, Olga Volkova, and Alexander Vasiliev, "Unveiling the hidden nematicity and spin subsystem in FeSe", npj Quantum Materials **2**, 32 (2017).

6. P. C. Cheng, W. Y. Tzeng, Y. J. Chu, C. W. Luo, A. A. Zhukov, J. Whittaker, J.-Y. Lin, K. H. Wu, J. Y. Juang, M. Liu, I. V. Morozov, A. I. Boltalin and A. N. Vasiliev, "3D visualizations of nanoscale phase separation and ultrafast dynamic correlation between phases in $(Na_{0.32}K_{0.68})_{0.95}Fe1.75Se2$", Physical Review Materials **3**, 034802 (2019).

An Emergent Metallic State IL01

Jiunn-Yuan Lin

Institute of Physics, National Chiao Tung University, Hsinchu 30010, Taiwan
E-mail: ago@cc.nctu.edu.tw

Two-dimensional (2D) CuO_2 planes play a key role in high-T_c cuprates. In the present study, ultrathin (1-20 uc) tetragonal $SrCuO_2$ (SCO) films were successfully layer-by-layer grown on TiO_2-terminated $SrTiO_3$ substrates using pulsed-laser-deposition technique. The structure of $SrCuO_2$ ultrathin films can be controlled. The thickness-dependent structural transformation of the $SrCuO_2$ films was studied by polarized x-ray absorption spectroscopy (XAS) at the Cu *L*-edge, and synchrotron-based x-ray diffraction and Laue diffraction. With the fabrication technology available, we demonstrate a new concept on inducing a 2D metallic phase in the $SrCuO_2/SrTiO_3$ structure via the oxygen sublattice and interface engineering. The electrical transport properties of this new state are studied by the electrical and Hall measurements.

Atsushi TAGUCHI

Associate Professor
Research Institute for Electronic Science
Hokkaido University
Kita 20-Nishi 10, Sapporo
Hokkaido 001-0020, JAPAN
Phone/Fax: 011-706-9395
Email: taguchi@es.hokudai.ac.jp

Notable Awards and Honors

• Optics Awards for Excellent Papers, Optical Society of Japan, 2016
• FANUC FA & Robot Foundation, Best Paper Award (Special Prize), 2005
• Numata Memorial Paper Award, Japan Society for Precision Engineering, 2004

Selected Publications

1. Correlative force and tip-enhanced Raman microscopy
   APL Photon. 2019, **4**, 021301 (Selected as "Featured Article").

2. Deep-Ultraviolet Biomolecular Imaging and Analysis
   Adv. Opt. Mater. 2019, **7**, 1801099.

3. Tip-enhanced Raman spectroscopy – from early developments to recent advances
   Chem. Soc. Rev. 2017, **46**, 4077–4110.

4. Nano-Raman scattering microscopy: Resolution and enhancement
   Chem. Rev. 2017, **117**, 4983–5001.

5. Optical antennas with multiple plasmonic nanoparticles for tip-enhanced Raman microscopy
   Nanoscale 2015, **7**, 17424–17433.

6. Indium for deep-ultraviolet surface-enhanced resonance Raman scattering
   ACS Photon. 2014, **1**, 598– 603.

7. Plasmon-enhanced UV photocatalysis
   Appl. Phys. Lett. 2014, **104**, 061108.

8. Tailoring plasmon resonances in the deep-ultraviolet by size-tunable fabrication of aluminum nanostructures
   Appl. Phys. Lett. 2012, **101**, 081110.

9. Deep-UV tip-enhanced Raman scattering
   J. Raman Spectrosc. 2009, **40**, 1324–1330.

10. Oxygen-assisted shape control in polyol synthesis of silver nanocrystals
    Chem. Phys. Lett. 2008, **462**, 92–95.

Plasmonics in Deep UV for Nanoimaging

Atsushi Taguchi[1]

[1]*Research Institute for Electronic Science, Hokkaido University, N20, W10, Sapporo, Hokkaido 001-0020, Japan*

Localizing and enhancing light at the nanoscale, plasmonics has been one of the hottest topics in the field of nanophotonics [1,2]. Gold and silver are the predominant choice of metal for plasmonics in visible and near-infrared wavelength region, however in the deep UV (DUV) region, these metals behave as absorptive dielectrics but not as metals. Therefore, no much attention has been paid to UV and DUV in plasmonics research. However, we found DUV is attractive in views of nano-imaging, spectroscopy, and industry applications.

In this presentation, I will discuss plasmonics in DUV from principles, materials and applications. We found that aluminum and indium are promising materials as plasmonic metals in DUV [3–5]. We have experimentally demonstrated that aluminum nanoparticles with a diameter of 50 nm exhibit localized plasmon resonance at a wavelength of 270 nm in DUV [4]. We applied an aluminum nanoparticle array to enhance photocatalytic activity of TiO_2 having a bandgap energy in UV [6]. We also fabricated plasmonic metal tip with aluminum nanoparticles attached to the apex and applied it to plasmonic tip-enhancement of resonance Raman scattering of adenine molecules excited with a wavelength of 266 nm [3]. We showed that metal grains on plasmonic tip act as an optical nano-antenna for high enhancement [7]. We developed a reflection objective that is compatible with DUV light with an N.A. as high as 0.9 [8].

References
1. S. Kawata, Y. Inouye, and P. Verma, *Nature Photon.*, **2009**, 3, 388–394.
2. T. Deckert-Gaudig, A. Taguchi, S. Kawata, and V. Deckert, *Chem. Soc. Rev.*, **2017**, 46, 4077–4110.
3. A. Taguchi, N. Hayazawa, K. Furusawa, H. Ishitobi, and S. Kawata, *J. Raman Spectrosc.*, **2009**, 40, 1324–1330.
4. A. Taguchi, Y. Saito, K. Watanabe, S. Yijian, and S. Kawata, *Appl. Phys. Lett.*, **2012**, 101, 081110.
5. S. Kawata, T. Ichimura, A. Taguchi, and Y. Kumamoto, *Chem. Rev.*, **2017**, 117, 4983–5001.
6. M. Honda, Y. Kumamoto, A. Taguchi, Y. Saito, and S. Kawata, *Appl. Phys. Lett.*, **2014**, 104, 061108.
7. A. Taguchi, J. Yu, P. Verma, and S. Kawata, *Nanoscale*, **2015**, 7, 17424–17433.
8. "Reflective objective lens and observation method," JP2017/031447, EP17848654.4, US16/331,466, Patent Pending.

Jiun-Tai CHEN

Professor
Department of Applied Chemistry
National Chiao Tung University (NCTU)
1001, Ta Hsueh Rd., Hsinchu 300, TAIWAN
Phone: ++886-3-5731631
Email: jtchen@mail.nctu.edu.tw
Website: http://www.jtchen.com

Education/Career

2017-present	*Associate Dean of Student Affairs,* National Chiao Tung University
2016-present	*Secretary in General,* The Polymer Society, Taipei (PST)
2016-present	*Professor,* National Chiao Tung University
2013-2016	*Associate Professor,* National Chiao Tung University
2010-2013	*Assistant Professor,* National Chiao Tung University
2008-2010	*Postdoctoral Fellow,* The University of Texas at Austin
2003-2008	*Ph.D.,* University of Massachusetts Amherst
1999-2001	*M. S.,* National Chiao Tung University
1995-1999	*B. S.,* National Chiao Tung University

Awards and Honors

2019	*Outstanding Polymer Research Award,* The Polymer Society, Taipei
2017	*Research Distinguished Professor Award,* LCY Education Foundation
2016	*Outstanding College Teaching Award,* Association of Science Education in Taiwan
2016	*Ta-You Wu Memorial Award,* Ministry of Science and Technology
2015	*Distinguishing Teaching Award,* National Chiao Tung University
2015	*Young Investigator Award of Polymer Technology,* The Polymer Society, Taipei
2014	*DuPont Young Professor Award*, DuPont
2013	*Young Chemists Award,* The Chemical Society Located in Taipei

Research Interests

Polymer Surfaces and Interfaces, Conducting Polymers, Polymer Nanostructures, Electrospinning

Selected Publications

1. C.W. Chang, M. H. Chi, H. W. Ko, C. W. Chu, Z. X. Fang, Y. H. Tu and **J. T. Chen**,* *Polym. Chem.*, **2017**, *8*, 3399.

2. C.W. Chu, Y. Higaki, C. H. Cheng, M. H. Cheng, C. W. Chang, **J. T. Chen**,* and A. Takahara,*, *Polym. Chem.,* **2017**, *8*, 2309.

3. M. H Chi, C. W. Chang, H. W. Ko, C. H. Su, C. W. Lee, C. H. Peng, and **J. T. Chen**,* *Macromolecules*, **2015**, *48*, 6241.

4. **J. T. Chen**,* P. H. Lee, H. F. Tseng, Y. J. Chiu, Y. H. Kao, K. S. Jeng, C. T. Liu, and C. C. Tsai, *ACS Macro Lett.*, **2015**, *4*, 721.

5. **J. T. Chen**,* T. H. Wei, C. W. Chang, H. W. Ko, C. W. Chu, M. H. Chi, and C. C. Tsai , *Macromolecules*, **2014**, *47*, 5227.

6. M. H. Chi, T. H. Wei, C. W. Lee, and **J. T. Chen**,* *Nanoscale*, **2014**, *6*, 1340.

7. Y. C. Huang, P. W. Fan, C. W. Lee, C. W. Chu, and **J. T. Chen**,* *ACS Appl. Mater. Interfaces*, **2013**, *5*, 3134.

8. P. W. Fan, W. L. Chen, T. H. Lee, Y. J. Chiu, and **J. T. Chen**,* *Macromolecules*, **2012**, *45*, 5816.

9. D. Chen, S. Park, **J. T. Chen**, E. Redston, and T. P. Russell,*, *ACS Nano*, **2009**, *3*, 2827.

10. **J.T. Chen**, M.F. Zhang, and T. P. Russell,* *Nano Lett.*, **2007**, *7*, 183.

Polymer Nanostructures by Wetting Nanopores in Anodic Aluminum Oxide Templates

Jiun-Tai Chen[1,2]

[1]*Department of Applied Chemistry, National Chiao Tung University, Hsinchu, Taiwan 30010,* [2]*Center for Emergent Functional Matter Science, National Chiao Tung University, Hsinchu, Taiwan 30010*

We study the fabrication and characterization of different polymer-related nanomaterials by wetting porous templates. The templates we choose are anodic aluminum oxide (AAO) templates because of the regular pore distribution, high pore density, and high aspect ratio of the pores. Different nanomaterials such as amorphous carbon nanotubes, amphiphilic block copolymer nanostructures, and porous inorganic materials are fabricated by using these templates. We also investigate the morphology transitions of polystyrene-block-polydimethylsiloxane (PS-*b*-PDMS) nanorods confined in the nanopores of AAO templates. The nanorods are formed by solvent-assisted template wetting, and the morphologies are compared to those in the bulk state. By blending PS-*b*-PDMS with homopolystyrene (hPS), the morphologies of the nanorods can be controlled because of the changes of the effective volume fractions. PS-*b*-PDMS micelle solutions are also used to prepare micelle nanostructures, and the critical parameters affecting the morphologies are determined. Micelle nanorods, micelle nanospheres, and multi-components nanopeapods can be prepared by wetting AAO templates with the micelle solutions. Rayleigh-instability-driven transformation is discovered to play an important role in controlling the morphologies of the micelle nanostructures. Zwitterionic polymer-grafted AAO templates are also prepared by surface-initiated atom transfer radical polymerization (SI-ATRP) and the geometric effect on the polymer chain growth in the confined nanopores are investigated.
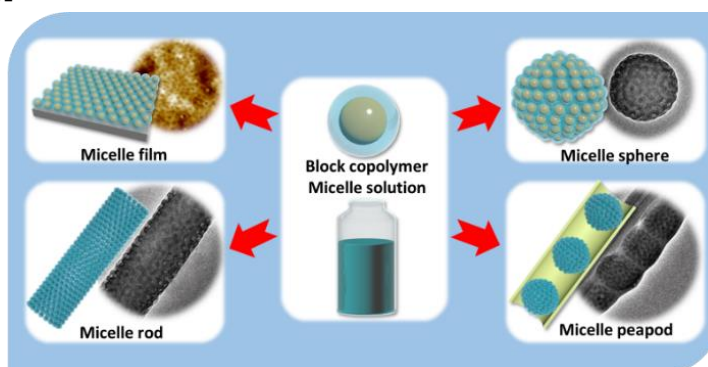
References

1. H. Bayat, C. H. Lin, M. H. Cheng, M. Steuber, J. T. Chen,* and H. Schonherr,* *ACS Appl.Nano Mater,* **2018,** *1,* 200-208.
2. C. W. Chu, Y. Higaki, C. H. Cheng, M. H. Cheng, C. W. Chang, J. T. Chen,* and A Takahara,* *Polym..Chem.,* **2017,** *8,* 2309.
3. M. H. Cheng, Y. C. Hsu, C. W. Chang, H. W. Ko, P. Y. Chung, and J. T. Chen,* *ACS Appl. Mater. Interfaces,* **2017,** *38,* 1600689.
4. H. W. Ko, T. Higuchi, C. W. Chang, M. H. Cheng, K. Isono, M. H. Chi, H. Jinnai,* and J. T. Chen,* *Soft Matter,* **2017,** 13, 5428.
5. C.W. Chang, M. H. Chi, H. W. Ko, C. W. Chu, Z. X. Fang, Y. H. Tu and J. T. Chen,* *Polym. Chem.,* **2017,** *8,* 3399.
6. H. W. Ko, M. H. Chi, C. W. Chang, C. W. Chu, K. H. Luo, and J. T. Chen,*, *ACS Macro Lett.,* **2015,** *4,* 717.
7. M. H. Chi, C. W. Chang, H. W. Ko, C. H. Su, C. W. Lee, C. H. Peng, and J. T. Chen,* *Macromolecules,* **2015,** *48,* 6241

Tomoya OSHIKIRI

Assistant Professor
Research Institute for Electronic Science
Hokkaido University
Kita 21-Nishi 10, Sapporo
Hokkaido 001-0021, JAPAN
Phone/Fax: 011-706-9338
Email: oshikiri@es.hokudai.ac.jp

Notable Awards and Honors

CSJ Student Presentation Award

Research interests

Plasmonic chemistry, Photochemical reaction, Artificial photosynthesis, Energy conversion, Supramolecular chemistry

Selected Publications

1. Ammonia photosynthesis via an association pathway using a plasmonic photoanode and a zirconium cathode
   Green Chem., 21, 4443-4448 (2019).

2. Efficient hot-electron transfer under modal strong coupling conditions with sacrificial electron donors
   ChemNanoMat, 5, 1008-1014 (2019). (Double first author, Selected as Cover Picture)

3. Manipulation of the dephasing time by strong coupling between localized and propagating surface plasmon modes
   Nat. Commun., 9, 48 (2018).

4. 4. Enhanced water splitting under modal strong coupling conditions
   Nat. Nanotechnol., 13, 953-958 (2018).

5. 5. Toward a translational molecular ratchet: face-selective translation coincident with deuteration in a pseudo-rotaxane
   Sci. Rep., 8,8950 (2018).

6. Selective dinitrogen conversion to ammonia using water and visible light via plasmon-induced charge separation
   Angew. Chem. Int. Ed., 55, 3942-3946 (2016).

7. Plasmon-induced ammonia synthesis through nitrogen photofixation with visible light irradiation
   Angew. Chem. Int. Ed. 53, 9802-9805 (2014). (Hot paper, Highlighted in *Nature Nanotechnol.*)

8. Plasmon-assisted water splitting using two sides of the same $SrTiO_3$ single-crystal substrate: conversion of visible light to chemical energy
   Angew. Chem. Int. Ed. 53, 10350-10354 (2014). (Hot paper)

Ammonia Photosynthesis Using Plasmon-induced Charge Separation under Visible Light Irradiation

Tomoya Oshikiri[1], Xu Shi[1], Kosei Ueno[2], Hiroaki Misawa[1,3]

[1]Research Institute for Electronic Science, Hokkaido University
[2]Department of Chemistry, Faculty of Science, and Graduate School of Chemical Sciences and Engineering, Hokkaido University
[3]Center for Emergent Functional Matter Science, National Chiao Tung University

Previously, we have demonstrated a localized surface plasmon resonance (LSPR)-induced water splitting system that operated under irradiation by visible light; the system was based on the excitation of plasmonic photoanode whose surface was loaded with gold nanoparticles (Au-NPs).[1-3] According to a similar method of the water splitting system, we have also successfully constructed the artificial photosynthesis system that produced the ammonia by a photofixation of a nitrogen molecule based on visible light irradiation.[4, 5] However, the reaction efficiency in the plasmon-induced artificial photosynthesis is still low.

In this study, we employed two approaches to improve efficiency. First, we reconstructed the photosynthetic device to enhance the ion and electron transport path. Furthermore, we investigated a quantitative evaluation of the plasmon-induced ammonia synthesis, such as bias effect, pH effect, stoichiometry, and intermediate. Based on these results, we propose the plasmon-induced NH_3 synthesis on Zr proceeds via an associative pathway in which N_2 is hydrogenated by protons.[6]

Second, the LSPR mode was coupled with the other optical mode.[7-9] We found that a Au-NPs/TiO_2-film/Au-film (ATA) photoanode with a modal strong coupling between the Fabry–Pérot nanocavity mode of the TiO_2 thin-film/Au-film and the LSPR mode of the Au-NPs extraordinarily enhanced water splitting efficiency as compared to that of Au-NPs/TiO_2 photoanode because the modal strong coupling shows the large and broad absorptivity in all visible region based on the split hybrid energy state. We will also introduce the ammonia photosynthesis using the ATA photoanode.

References

1. Y. Zhong, K. Ueno, Y. Mori, X. Shi, T. Oshikiri, K. Murakoshi, H. Inoue and H. Misawa, *Angew. Chem. Int. Ed.*, 2014, **53**, 10350-10354.

2. Y. Zhong, K. Ueno, Y. Mori, T. Oshikiri and H. Misawa, *J. Phys. Chem. C*, 2015, **119**, 8889-8897.

3. R. Takakura, T. Oshikiri, K. Ueno, X. Shi, T. Kondo, H. Masuda and H. Misawa, *Green Chem.*, 2017, **19**, 2398-2405.

4. T. Oshikiri, K. Ueno and H. Misawa, *Angew. Chem. Int. Ed.*, 2014, **53**, 9802-9805.

5. T. Oshikiri, K. Ueno and H. Misawa, *Angew. Chem. Int. Ed.*, 2016, **55**, 3942-3946.

6. T. Oshikiri, K. Ueno and H. Misawa, *Green Chem.*, 2019, **21**, 4443-4448.

7. X. Shi, K. Ueno, T. Oshikiri, Q. Sun, K. Sasaki and H. Misawa, *Nat. Nanotechnol.*, 2018, **13**, 953-958.

8. J. Yang, Q. Sun, K. Ueno, X. Shi, T. Oshikiri, H. Misawa and Q. Gong, *Nat. Commun.*, 2018, **9**, 4858.

9. Y. Cao, T. Oshikiri, X. Shi, K. Ueno, J. Li and H. Misawa, *ChemNanoMat*, 2019, **5**, 1008-1014.

Chi-Shen LEE

Professor
Department of Applied Chemistry
National Chiao-Tung University
1001 Univ Rd, Hsinchu
Hsinchu 30010, TAIWAN
Phone/Fax: 1-886-3-5131332
Email: chishen@mail.nctu.edu.tw

Selected Publications

1. Metal Substituted Pyrochlore Phase $Li_xLa_{2-x}Ce_{1.8}Ru_{0.2}O_{7-\Delta}$ (X = 0.0–0.6) as an Effective Catalyst for Oxidative and Auto-Thermal Steam Reforming of Ethanol.
   Catalysis Science & Technology **2019**, *9*, 1406–1419.

2. Hydrogen Production From Oxidative Steam Reforming of Ethanol on Nickel-Substituted Pyrochlore Phase Catalysts.
   International Journal of Hydrogen Energy **2017**, *42* (5), 2849–2860.

3. $Ba_3TM_2Se_9$ (TM = Nb, Ta): Synthesis and Characterization of New Polyselenides.
   Inorg Chem **2014**, *53* (1), 80–84.

4. Autothermal Steam Reforming of Ethanol Over $La_2Ce_{2-x}Ru_xO_7$ (X = 0–0.35) Catalyst for Hydrogen Production.
   Applied Catalysis B: Environmental **2013**, *134-135*, 359–366.

5. Multinary Selenides with Unusual Coordination Environment of Bismuth.
   Inorg Chem **2012**, *51* (24), 13328–13333.

6. Enhanced Catalytic Activity of $Ce_{1-x}M_xO_2$ (M = Ti, Zr, and Hf) Solid Solution with Controlled Morphologies.
   Chem. Commun. **2010**, *46* (19), 3286.

Catalysts of Metal substituted Pyrochlores $A_2B_2O_7$ (A = Alkali/Alkaline Earth/Rare Earth elements; B = Ce/Ru/Ni) for Oxidative Steam Reforming of Ethanol

Ho-Chen Hsieh[1, 3], Sheng-Feng Weng[1], Ping-Wen Tsai[1], Yuan-Chia Chang[1], and Chi-Shen Lee[1, 2]

[1]*Department of Applied Chemistry, National Chiao Tung University, 1001 University Rd., Hsinchu 30010, Taiwan*
[2]*Center for Emergent Functional Matter Science, National Chiao Tung University, Hsinchu 30010, Taiwan*
[3]*Graduate Degree Program of Science and Technology of Accelerator Light Source, National Chiao Tung University, Hsinchu 30010, Taiwan*

Oxidative steam reforming of ethanol to produce hydrogen or syngas (H_2/CO) is an important process for fuel cell applications. To achieve high conversion of ethanol and yield of hydrogen, a stable catalyst that is active on ethanol conversion is desired. In this presentation, I will summarize our efforts to develop new oxide catalysts for OSRE process. Metal substituted pyrochlores $A_2B_2O_{7-\delta}$ (A = Alkali/Alkaline Earth/Rare Earth elements; B = Ce/Ru/Ni) were synthesized and used as catalysts for oxidative steam reforming of ethanol. The solid solution phases were prepared via the sol-gel process. The substituted metal cations are active to OSRE and distributed evenly in the pyrochlore structure. The as-prepared samples were characterized and the influence of substituted metal cations on the activity of OSRE was investigated. PXRD Rietveld analysis and elemental analysis (ICP-AES) support the formation of a pyrochlore-type structure (space group Fd-3m) with the distorted coordination environment. The catalytic performances were tested with varied temperatures, metal ion contents, carbon-to-oxygen ratios and long-term stabilities. In general, the OSRE activity is depending on the active metal cations in B sites of pyrochlore structure. Under the conditions of nearly 100% ethanol conversion, optimized hydrogen selectivity's are 99(1) for Ru-substituted catalyst $La_2Ce_{1.8}Ru_{0.2}O_7$. For Ni^{2+}-substituted pyrochlore $La_2Ce_{2-x}Ni_xO_{7-\delta}$, performance on ethanol conversion is affected by the Ni content and the H_2 selectivity reaches to the highest value 82.6(1) % for sample of x=0.45. Further studies were extended to metal substitution on A sites with alkali, alkaline earth, and rare earth elements. Pyrochlore phase $Li_xLa_{2-x}Ce_{1.8}Ru_{0.2}O_{7-\delta}$ (x = 0.0 - 0.6) [LLCRO] substituted by Li and Ru in A and B sites supported by LZO exhibited average ethanol conversion and hydrogen selectivity of 90(3)% and 71(4)%, respectively. Alkaline earth metal substitutions on the A-site of pyrochlore oxide $xLa_{2-x}Ce_{1.8}Ru_{0.2}O_{7-\delta}$ (M = Mg, Ca) showed optimized catalysts $Mg_{0.3}La_{1.7}Ce_{1.8}Ru_{0.2}O_{7-\delta}$ and $Ca_{0.2}La_{1.8}Ce_{1.8}Ru_{0.2}O_{7-\delta}$ with H_2 selectivity 101(1)% and 91(2)% under OSRE. The substitution of cations in A-sites affect the oxidation states of $Ce^{4+/3+}$ and Run+ ions and create oxygen vacancies. Catalysts supported on $La_2Zr_2O_7$ showed stable OSRE/ATR performance and low carbon deposition compared to catalysts supported on Al_2O_3. We ascribe the enhanced activity to well-dispersed alkaline earth metal and Ru ions in a solid solution structure, synergistic effects of $(Li, Mg, Ca)^{2+}/Ce^{3+,4+}/Ru^{n+}$ ions, and strong catalyst-support interaction that optimized the ethanol conversion and hydrogen production.

References

1. S.-F. Weng , Y.-H. Wang, and C.-S. Lee, *Appl. Catal. B.*, **2013**, 134-135, 359–366.
2. S.-F. Weng , H.-C. Hsieh, and C.-S. Lee, *Int. J. Hydrog. Energy*, **2017**, 42, 2849–2860.
3. H.-C. Hsieh, Y.-C. Chang, P.-W. Tsai, Y.-Y. Lin, Y.-C. Chuang, H.-S. Sheu and C.-S. Lee, *Catal. Sci. Technol.*, **2019**, 9, 1406–1419.

Ken-ichi YUYAMA

Assistant Professor
Research Institute for Electronic Science &
Graduate School of Environmental Science
Hokkaido University
Kita 20-Nishi 10, Sapporo
Hokkaido 001-0020, JAPAN
Phone/Fax: 011-706-9416
Email: yuyama@es.hokudai.ac.jp

Notable Awards and Honors

• Japanese Photochemistry Association Award for Young Scientists, 2019
• The Japanese Association for Crystal Growth, The 35th Best Paper Award, 2018
• The Japan Society of Applied Physics, The Best Presentation Award in Spring Meeting, 2010

Selected Publications

1. In-situ reflection imaging and microspectroscopic study on three-dimensional crystal growth of L-phenylalanine under laser trapping
   Appl. Phys. Express 2019, **12**, 112008.

2. Mixed-halide perovskite synthesis by chemical reaction and crystal nucleation under an optical potential
   NPG Asia Mater. 2019, **11**, 31.

3. Crystallization of methylammonium lead halide perovskites by optical trapping
   Angew. Chem. Int. Ed. 2018, **57**, 13424–13428.

4. Crystal growth and dissolution dynamics of L-phenylalanine controlled by solution surface laser trapping
   Cryst. Growth Des. 2018, **18**, 7079–7087.

5. A single spherical assembly of protein amyloid fibrils formed by laser trapping
   Angew. Chem. Int. Ed. 2017, **56**, 6739–6743.

6. Two-dimensional growth rate control of L-phenylalanine crystal by laser trapping in unsaturated aqueous solution
   Cryst. Growth Des. 2016, **16**, 953–960.

7. Optical trapping-formed colloidal assembly with horns extended to the outside of a focus through light propagation
   Nano Lett. 2016, **16**, 3058–3062.

8. Laser trapping and crystallization dynamics of L-phenylalanine at solution surface
   J. Phys. Chem. Lett. 2013, **4**, 2436–2440.

9. Formation, dissolution, and transfer dynamics of a millimeter-scale thin liquid droplet in glycine solution by laser trapping
   J. Phys. Chem. C 2012, **116**, 6809–6816.

10. Millimeter-scale dense liquid droplet formation and crystallization in glycine solution induced by photon pressure
    J. Phys. Chem. Lett. 2010, **1**, 1321–1325.

# Optically-Controlled Synthesis and Modification of Lead Halide Perovskites under Laser Trapping

Ken-ichi Yuyama,[1,2] Md Shahjahan,[2] Md Jahidul Islam,[2] Vasudevanpillai Biju[1,2]

[1]Research Institute for Electronic Science, Hokkaido University, N20W10, Sapporo, Hokkaido 001-0020, Japan, and [2]Graduate School of Environmental Science, Hokkaido University, N10W5, Sapporo, Hokkaido 060-810, Japan

Ever since Ashkin demonstrated a single-beam gradient force optical trap (optical tweezers), it has played innovative roles in manipulating dielectric micro-objects without mechanical contact. In chemistry, this technique was applied to smaller objects, such as nanoparticles, quantum dots, polymers, proteins, and amino acids, confining and assembling those in the focal volume. Despite the spatio-temporal preparation of assemblies and crystals, the potential of laser trapping technique for chemical reactions remains unexplored. Here, we present optically-controlled synthesis and modification of lead halide perovskites, which results from chemical reactions in the precursor solutions through local concentration increase under laser trapping.

For the synthesis of perovskite crystals, a precursor solution prepared by dissolving MAX and PbX_2 ($MA = CH_3NH_3^+$, X = Br & Cl) in a mixture of DMSO/DMF was placed in a handmade sample chamber. Figure 1a shows crystallization behavior under the laser irradiation (1.0 W) at the surface of a precursor solution of $MAPbBr_{1.0}Cl_{2.0}$. The crystallization was similarly induced from the focal spot in the unsaturated precursor solutions of other compositions, $MAPbBr_nCl_{3-n}$ (n = 0, 0.5, 1.5, 2.0, 2.5, 3.0). Different from spontaneous formation of multiple crystals in saturated precursor solutions, laser irradiation creates one single crystal with a high chloride composition in a spatio-temporally controlled manner, which is through local concentration increase of precursor complexes and their de-solvation in optical potential.[1,2]

For the site-specific modification of a perovskite crystal, a $MAPbBr_{3.0}$ micro-rod was prepared with a chemical approach in a sample chamber, followed by the addition of a reaction solution [MAI (250 μM) in isopropyl alcohol:hexadecane (1:100, v:v)]. Figure 1b shows photoluminescence (PL) images before and after the laser irradiation to the center of the micro-rod. Before the irradiation, the whole $MAPbBr_{3.0}$ micro-rod showed green emission due to its intrinsic property [panel (i) of Fig. 1b]. After the irradiation, the green emission was gradually changed into first yellow and finally red [panel (ii) of Fig. 1b]. This is due to local halide exchange reaction of $MAPbBr_{3.0}$ with MAI, which leads to the formation of $MAPb(Br \cdot I)_{3.0}$ of a lower bandgap. Such bandgap modification was possible in multiple positions by shifting the laser focus after the first irradiation, which is due to local concentration increase in MAI under laser trapping.
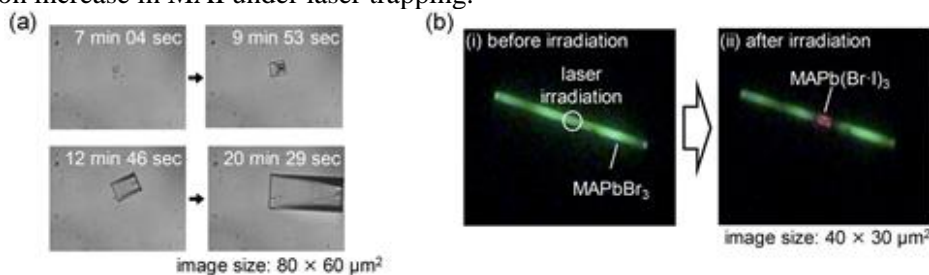
Figure 1. (a) Optical micrographs around the focal spot under the laser irradiation to the precursor solution of $MAPbBr_{1.0}Cl_{2.0}$. (b) PL images of a $MAPbBr_{3.0}$ micro-rod before and after the laser irradiation.

References

1. K. Yuyama, Md J. Islam, K. Takahashi, T. Nakamura, V. Biju, *Angew. Chem. Int. Ed.,* **2018**, *57*, 13424−13428.
2. Md J. Islam, K. Yuyama, K. Takahashi, T. Nakamura, K. Konishi, V. Biju, *NPG Asia Mater.,***2019**, *11*, 31.

Yu-Miin SHEU

Assistant Professor
Department of Electrophysics
National Chiao Tung University
1001, Ta Hsueh Rd, Hsinchu 300, TAIWAN
Phone: +886-3-571-2121(ext 56121)
FAX: +886-3-572-5230
E-Mail: ymsheu@nctu.edu.tw

Education & Work Experience

2014-2015	Postdoctoral research associate, CEMS, RIKEN, Japan
2010-2014	Postdoctoral research associate, CINT, Los Alamos National Lab, USA
2010-2010	Visiting research investigator, The University of Michigan (Ann Arbor), USA
2004-2009	PhD, Department of Physics, The University of Michigan (Ann Arbor), USA

Award & Honor

- Junior Investigator Research Awards, College of Science, National Chiao Tung University, 2019.
- Outstanding Mentor Award of National Chiao Tung University, 2019.
- Outstanding Mentor Award of National Chiao Tung University, 2018.
- Distinguished Outstanding-Mentor Award of National Chiao Tung University, 2017.
- Talents Recruit Award of Ministry of Science and Technology, Taiwan, 2015, 2016, 2017.
- Distinguished Postdoctoral Publication Award of Los Alamos National Lab, 2015.

Selected Publications:

1. **Y. M. Sheu**[*], Y. M. Chang, C. P. Chang, Y. H. Li, K. R. Babu, G.Y. Guo, T. Kurumaji, and Y. Tokura, "Picosecond creation of switchable optomagnets from a polar antiferromagnet with giant photoinduced Kerr rotations", **Physical Review X 9**, 031038 (2019).
2. **Y. M. Sheu**[*], N. Ogawa, Y. Tokunaga, H. C. Chan, and Y. Tokura, "Selective probe of coherent polar phonon and quasiferromagnetic resonance modesin multiferroic $GdFeO_3$" **Physical Review B: Rapid Communications 98**, 100301(R) (2018).
3. **Y. M. Sheu**[*], S. A. Trugman, A. Chen, Q. X. Jia, A. J. Taylor, and R. P. Prasankumar, "Unraveling thickness-dependent spin relaxation in colossal magnetoresistance manganite films" **Applied Physics Letters 113,** 012402 (2018).
4. **Y. M. Sheu*,** N. Ogawa, Y. Kaneko, and Y. Tokura, " Photocreating supercooled spiral-spin states in a multiferroic manganite ", **Physical Review B: Rapid Communications 94,** 081107(R) (2016).
5. **Y. M. Sheu**[*], S. A. Trugman, L. Yan, Q. X. Jia, A. J. Taylor, and R. P. Prasankumar[*], "Using ultrashort optical pulses to couple ferroelectric and ferromagnetic order in an oxide heterostructure", **Nature Communications** 5:5832 (2014).
6. **Y. M. Sheu**[*], S. A. Trugman, L. Yan, J. Qi, Q. X. Jia, A. J. Taylor, and R. P. Prasankumar[*], "Polaronic transport induced by competing interfacial magnetic order in a $La_{0.7}Ca_{0.3}MnO_3/BiFeO_3$ heterostructure", **Physical Review X 4**, 021001 (2014).
7. **Y. M. Sheu**[*], S. A. Trugman, L. Yan, C.-P. Chuu, Q. X. Jia, A. J. Taylor, and R. P. Prasankumar[*], "Photo-induced stabilization and enhancement of the ferroelectric polarization in $Ba_{0.1}Sr_{0.9}TiO_3$ /$La_{0.7}Ca(Sr)_{0.3}MnO_3$ thin film heterostructures", **Physical Review B: Rapid Communications** 88, 020101(R) (2013).
8. **Y. M. Sheu**[*], Y. J. Chien, C. Uher, S. Fahy, and D. A. Reis, "Free-carrier relaxation and lattice heating in photoexcited bismuth", **Physical Review B 87**, 075429 (2013).
9. **Y. M. Sheu**[*], S. A. Trugman, Y.-S. Park, S. Lee, H. T. Yi, S.-W. Cheong, Q. X. Jia, A. J. Taylor, and R. P. Prasankumar[*], "Ultrafast carrier dynamics and radiative recombination in multiferroic $BiFeO_3$", **Applied Physics Letters 100**, 242904 (2012).

Picosecond Creation of Switchable Optomagnets from a Polar Antiferromagnet with Giant Photoinduced Kerr Rotations IL07

Yu-Miin Sheu

Department of Electrophysics, National Chiao Tung University, Hsinchu 300, Taiwan

On-demand spin orientation with long polarized lifetime and easily detectable signal is an ultimate goal for spintronics. However, there still exists a trade-off between controllability and stability of spin polarization, awaiting a significant breakthrough. Here, we demonstrate switchable optomagnet effects in $(Fe_{1-x}Zn_x)_2Mo_3O_8$, from which we can obtain tunable magnetization, spanning from -40% to 40% of a saturated magnetization that is created from zero magnetization in the antiferromagnetic state without magnetic fields. It is accomplishable via utilizing circularly-polarized laser pulses to excite spin-flip transitions in polar antiferromagnets that have no spin canting, traditionally hard to control without very strong magnetic fields. The spin controllability in $(Fe_{1-x}Zn_x)_2Mo_3O_8$ originates from its polar structure that breaks the crystal inversion symmetry, allowing distinct on-site *d-d* transitions for selective spin flip. By chemical doping, we exploit the phase competition between antiferromagnetic and ferrimagnetic states to enhance and stabilize the optomagnet effects, which result in long-lived photoinduced Kerr rotations. The present study, creating switchable giant optomagnet effects in polar antiferromagnets, sketches a new blueprint for the function of antiferromagnetic spintronics.
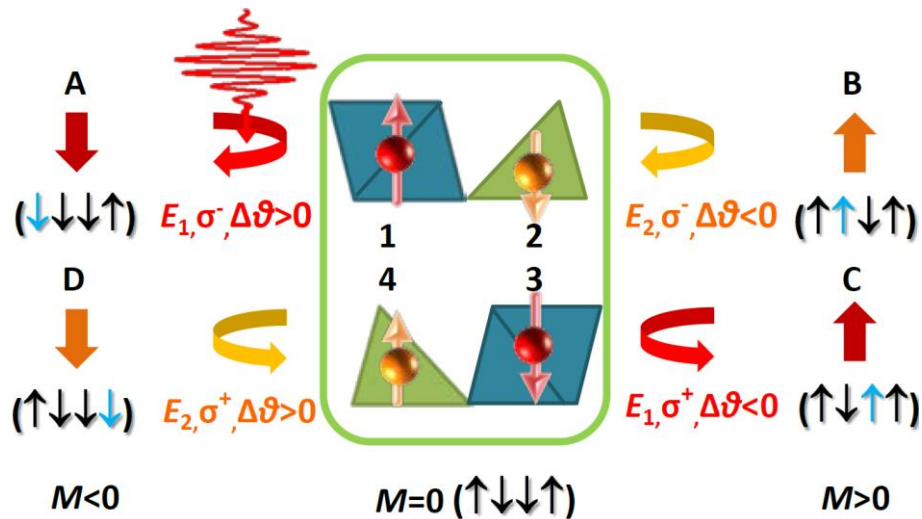
Fig. 1. Illustration of optomagnets created by optical helicities in a magnetic basis. Four distinct spin quantum states A, B, C, D can be selectively created from the zero-magnetization (M=0) state by flipping one of the sublattice spin moments $(1,2,3,4) = (\uparrow\downarrow\downarrow\uparrow)$ with the flipped moment color coded in each unique configuration. This optomagnet can be made possible through the on-site d-d optical transitions with combinations of pump photon energies $E_{1,2}$ and circularly polarized pumps $\sigma^\pm$. Combining the resultant magneto-optical Kerr rotations $\Delta\theta$, we can unambiguously discern the four distinct microscopic states that lead to two switchable magnetization directions macroscopically.
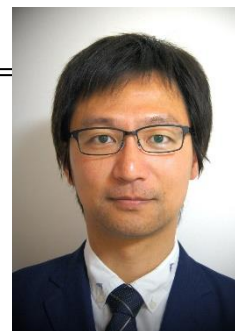
Reference:

1. Y. M. Sheu, Y. M. Chang, C. P. Chang, Y. H. Li, K. R. Babu, G.Y. Guo, T. Kurumaji, and Y. Tokura, *Physical Review X* **9**, 031038 (2019).

Ichiro HISAKI

Associate professor
Research Institute for Electronic Science &
Graduate School of Environmental Science
Hokkaido University
Kita 20-Nishi 10, Sapporo
Hokkaido 001-0020, JAPAN
Phone/Fax: 011-706-9418
Email: hisaki@es.hokudai.ac.jp

Notable Awards and Honors

- SHGSC Japan Award of Excellence 2019 on 17th Symposium on Host-Guest and Supramolecular Chemistry, Japan 2019
- Young Scientist Award on Polymer Science Meeting in Kobe, Japan, 2017
- Award for Encouragement of Research on 26rd Annual Meeting on MRS-J, Japan, 2016

Selected Publications

1. Designing Hydrogen-bonded Organic Frameworks (HOFs) with Permanent Porosity
   Angew. Chem. Int. Ed. **2019**, 58, 11160‑11170. (Minireview)

2. Acid Responsive Hydrogen-bonded Organic Framework
   J. Am. Chem. Soc. **2019**, 141, 2111–2121.

3. Docking Strategy to Construct Thermostable, Single-crystalline, Hydrogen-bonded Organic Framework with Large Surface Area
   Angew. Chem. Int. Ed. **2018**, 57, 12650–12655.

4. Hydrogen-bonded Hexagonal Buckybowl Framework
   Angew. Chem. Int. Ed. **2017**, 56, 15294–15298.

5. Hexaazatriphenylene-Based, Hydrogen-Bonded Organic Framework with Permanent Porosity and Single-Crystallinity
   Chem. Eur. J. **2017**, 23, 11611–11619.

6. Alignment of Paired Molecules of C_{60} within a Hexagonal Platform Networked through Hydrogen-Bonds
   Chem. Commun. **2016**, 52, 9781–9784.

7. A Series of Layered Assemblies of Hydrogen-Bonded, Hex-agonal Networks of C_3-Symmetric π-Conjugated Molecules: A Potential Motif of Porous Organic Materials
   J. Am. Chem. Soc. **2016**, 138, 6617–6628.

8. C3-Symmetric Macrocycle-Based, Hydrogen-Bonded, Multi-Porous Hexagonal Network as Motif of Porous Molecular Crystals
   Angew. Chem. Int. Ed. **2015**, 54, 3008–3012.

Hydrogen-bonded Organic Frameworks

Ichiro Hisaki[1,2]

[1]*Graduate School of Environmental Science, Hokkaido University, N10W5, Sapporo, Hokkaido 060-810, and* [2]*Research Institute for Electronic Science, Hokkaido University, N20, W10, Sapporo, Hokkaido 001-0020, Japan*

Among porous molecular crystals, those constructed through preorganized hydrogen bonding, named Hydrogen-bonded Organic Frameworks (HOFs), recently attract much attention as a new class of porous organic materials because of their high crystallinity, potential designability, regenerability, and facile construction process.[1] HOFs, however, have been regarded as relatively fragile framework and their current designing strategy is still insufficient compared with other porous materials such as MOFs and COFs because of weakness of H-bonds. In connection with this, we have demonstrated that various C_3-symmetric π-conjugated molecules possessing *o*-bis(4-carboxyphenyl)aryl groups in their periphery successfully gave H-bonding low-density networked structures, which effectively gave stable HOFs with permanent porosity by activation (see Figure).[2] The obtained HOFs show significant thermal stability over 300 °C and permanent porosity with the Brunauer–Emmett–Teller surface area values up to 1288 m^2g^{-1}.[3] Moreover, optoelectronic properties of π-conjugated systems applied for the building blocks enabled to provide multifunctional HOFs such as acid-responsive HOFs with permanent porosity.[4] Our strategy for constructing functional HOFs contribute to developing a new field of porous organic materials.
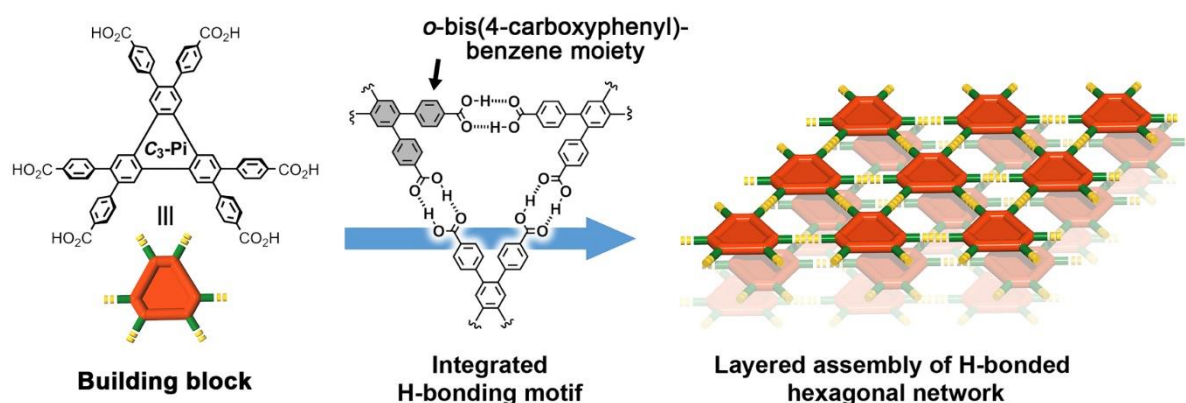
Figure. Formation of layered HOFs via H-bonding of C_3-symmetric π-conjugated molecules.

References
1. Lin, R.-B.; He, Y.; Li, P.; Wang, H.; Zhou, W.; Chen, B. *Chem. Soc. Rev.* **2019**, 48, 1362–1389. (b) Hisaki, I.; Chen, X.; Takahashi, K.; Nakamura, T. *Angew. Chem. Int. Ed.* **2019**, 58, 11160–11170.
2. Hisaki, I.; Nakagawa, S.; Ikenaka, N.; Imamura, Y.; Katouda, M.; Tashiro, M.; Tsuchida, H.; Ogoshi, T.; Sato, H.; Tohnai, N.; Miyata, M. *J. Am. Chem. Soc.* **2016**, 138, 6617–6628.
3. Hisaki, I.; Suzuki, Y.; Gomez, E. Tohnai, N.; Douhal, A. *Angew. Chem. Int. Ed.* **2018**, 57, 12650–12655.
4. Hisaki, I.; Suzuki, Y.; Gomez, E. Ji, Q.; Tohnai, N.; Nakamura, T.; Douhal, A. J. *Am. Chem. Soc.* **2019**, 141, 2111–2121.

Bor-Ran LI

Assistant Professor
Institute of Biomedical Engineering,
National Chiao Tung University
Room 468, Engineering Building VI
No. 1001 University Road, Hsinchu 300, Taiwan
Tel: 03-5712121-54051
Email: liborran@g2.nctu.edu.tw

Notable Awards and Honors

• 16th National Innovation Award (2019)

• MOST FutureTech Demo and Breakthrough Award (2019)

• MOST Assistant Researcher Scholar Fellowship (2014-2016)

• Academia Sinica Postdoctoral Fellowship (2012 – 2014)

• EaStCHEM Prize Postgraduate Full Studentship (2005 – 2008)

Selected Publications

1. Chiu PL, Chang CH, Lin YL, Tsou PH, Li BR* Rapid and safe Isolation of Human peripheral Blood B and T Lymphocytes through spiral Microfluidic Channels. 2019 May *Sci. Rep.* 9 (1), 8145

2. Yang CH, Hsieh YL, Tsou PH, Li BR* Thermopneumatic suction integrated microfluidic blood analysis system. *PLOS ONE*. 2019 Mar 14 (3), e0208676

3. Chang CY, Lin HJ, Li BR*, Li YK* A novel metallo-β-lactamase involved in the ampicillin resistance of Streptococcus pneumoniae ATCC 49136 strain *PLOS ONE*. 2016 May 23;11(5):e0155905

4. Chang CY, Li BR*, Li YK*. An l-ascorbate-6-phosphate lactonase from Streptococcus pneumoniae ATCC 49136 strain reveals metallo-β-lactamase activity. *Int. J Antimicrob. Agents.* 2016, 47 (5): 416–418

5. Shen MY, Li BR*, Li YK*. Nano-scale field-effect-transistor based biosensors: from sensitive to ultra-sensitive. *Biosens. Bioelectron.* 2014 Mar 14; 60: 101-111

6. Li BR, Shen MY, Yu SH, Li YK. Rapid construction of an effective antifouling layer on a Au surface via electrodeposition. *Chem. Comm.* 2014 Apr 17; 50 (51), 6793-6796

7. Li BR, Chen CC, Kumar UR, Chen YT. Advances in nanowire transistors for biological analysis and cellular investigation. *Analyst.* 2014 Feb 6; (139) : 1589-1608.

8. Li BR, Hsish YJ, Chung YT, Shiu YH, Pan CY, Chen YT. A nanowire-transistor biosensor for ultra-sensitively detecting dopamine released under hypoxic stimulation from living PC12 cells. *J. Am. Chem. Soc.*, 2013 Oct 14; (135): 16034−16037.

9. Li BR, Chen CW, Yang WL, Lin TY, Pan CY, Chen YT. Biomolecular recognition with a sensitivity enhanced nanowire-transistor biosensor. *Biosens. Bioelectron.* 2013 July 15; (45): 252–259.

10. Lin TY, Li BR, Tsai ST, Chen CW, Chen CH, Chen YT, Pan CY. Improved silicon nanowire field-effect transistors for fast protein-protein interaction screening. *Lab Chip.* 2013 Jan 22; 13(4): 676-684.

Design Microfluidic Chips for Clinical Use

BorRan Li[1,2,]

[1]*Institute of Biomedical Engineering, National Chiao Tung University*
[2]*Center for Emergent Functional Matter Science, CEFMS, National Chiao Tung University*

A biosensor is generally defined as an analytical device, which converts the biochemical responses into the quantifiable electronic signals. Its extensive utilities in medical diagnosis, toxicity testing, chemical analysis, food industry, and many other areas for quantitative assessments has appeared. Quartz crystal microbalance and field-effect transistor-based devices have been demonstrated to possess exceptional characteristics and outstanding performance while conjugated with the advanced nanotechnology. However, both devices still have to face the nonspecific binding issue, which is a headache for researchers on all biosensor platforms. In our research, we have efficaciously reduced 95% nonspecific binding *via* immobilize the zwitterionic layer on the surface of the chip. Moreover, we integrate microfluidics, nanoparticles, rapid surface modification on several bio-sensing platforms to efficiently pretreat specimens and detect target bio-molecules. In addition, a series advanced microfluidic chips are designed for lymphocyte isolation, active sperm sorting, and nanoparticle synthesis.
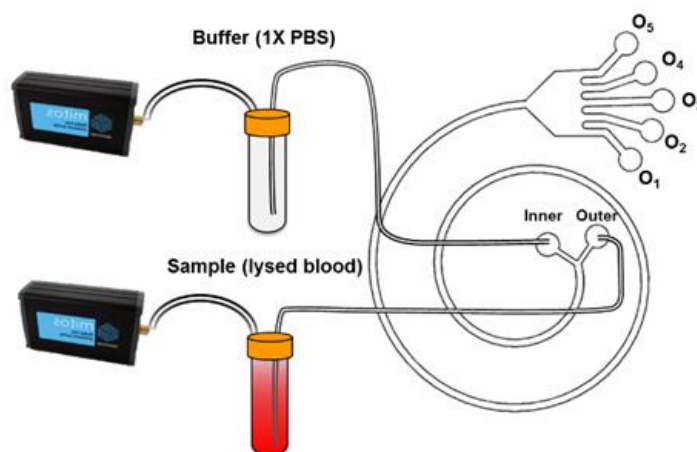
Fig. 1 Illustration of the setup of spiral microfluidic channels for isolating human PBL rapidly and safely.

References

1. D. M. Jang, K. Park, D. H. Kim, J. Park, F. Shojaei, H. S. Kang, J-P. Ahn, J. W. Lee, and J. K. Song, *Nano Lett.,***2015**, *15*, 5191−5199.

2. BR Li, YJ Hsieh, YX Chen, YT Chung, CY Pan, YT Chen *JACS*, **2013** 135 (43), 16034-16037

3. BR Li, MY Shen, H Yu, YK Li *Chemical Communications* **2014** 50 (51), 6793-6796

4. MY Shen, BR Li, YK Li *Biosensors and Bioelectronics* **2014** 60, 101-111

5. CY Chang, HJ Lin, BR Li, YK Li *PloS ONE* **2016** 11 (5), e0155905

6. PL Chiu, CH Chang, YL Lin, PH Tsou, BR Li *Scientific Report*, **2019** 9, 8145

Hiroshi TERAMOTO

Associate Professor
Research Institute for Electronic Science &
Department of Mathematics
Hokkaido University
Kita 20-Nishi 10, Sapporo
Hokkaido 001-0020, JAPAN & JST, PRESTO,
Department of Research Promotion, Tokyo, 102-0076, Japan.
Phone/Fax: 011-706-9435
Email: teramoto@es.hokudai.ac.jp

Notable Awards and Honors
• JST, PRESTO Sakigake, 2016 -

Selected Publications

1. Classification of Hamiltonians in neighborhoods of band crossings in terms of the theory of singularities, J. Math. Phys. 2017, **58**, 073502.

2. Spectral-clustering approach to Lagrangian vortex detection, Phys. Rev. E 2016, **93**, 063107.

3. Deciphering Time Scale Hierarchy in Reaction Networks, J. Phys. Chem. B, 2016, **120**, 1961.

4. Understandings of chemical reaction dynamics in terms of dynamical systems theory, AIP Conf. Proc., 2015, **1702**, 090042.

5. Mechanism and Experimental Observability of Global Switching Between Reactive and Nonreactive Coordinates at High Total Energies, Phys. Rev. Lett., 2015, **115**, 093003.

6. Breakdown mechanism of normally hyperbolic invariant manifolds in terms of unstable periodic orbits and homoclinic/heteroclinic orbits in Hamiltonian systems, Nonlinearity 2015, **28**, 2677

7. Local-heterogeneous response and transient dynamics of cage breaking and formation in colloidal fluids, J. Chem. Phys. 2014, **141**, 104907.

8. A New Method to Improve Validity Range of Lie Canonical Perturbation Theory, Theor. Chem. Acc., 2014, **133**, 1571.

9. Detecting Invariant Manifolds as Stationary Lagrangian Coherent Structures in Autonomous Dynamical Systems", Chaos, 2013, **23**,043107.

10. A Dynamical Switching of a Reaction Coordinate to Carry the System Through to a Different Product State at High Energies, Phys. Rev. Lett., 2011, **106**, 054101

Type of Singularity that can Appear in Pareto Set   IL10

Hiroshi Teramoto[1], Yutaro Kabata[2], Kenta Hayano[3], and Naoki Hamada[4]

[1]*Research Institute for Electronic Science, Hokkaido University, N20, W10, Sapporo, Hokkaido 001-0020, Japan,* [2]*Institute of Mathematics for Industry, Kyushu University, Fukuoka, 819-0395, Japan,* [3]*Department of Mathematics Faculty of Science and Technology, Keio University, Yokohama, 223-8522, Japan,* [4]*Artificial Intelligence Laboratory, Fujitsu Laboratories Ltd., Kawasaki, 211-8588, Japan*

We consider a minimization problem minimizing p objective functions $f_i \colon \mathbb{R}^n \to \mathbb{R}$ $(i = 1, \cdots, p)$ depending on n state variables. Pareto set is a set of points in $\mathbb{R}^n$ at which, for any $i \in \{1, \cdots, p\}$, one cannot decrease i-th objective function without increasing any one of the other objective functions. Pareto front is the image of Pareto set mapped by $f = (f_1, \cdots, f_p)$. In general, if p is greater than 1, the objective functions cannot be minimized simultaneously and thus it is important to understand structures of the Pareto set and front, which are the set of the best compromise solutions and their image by f, respectively.

Under the assumption that n is equal to or greater than p and the objective functions are smooth, the first order necessary condition implies that the Pareto set is a subset of singular points, where the singular points of a map $f \colon \mathbb{R}^n \to \mathbb{R}^p$ is the set of points at which the rank of the Jacobi matrix is less than p. We introduce an equivalence relation among maps and classify local geometries of Pareto set and Pareto front up to diffeomorphism. Below, we show the Pareto set and Pareto front of two of the equivalence classes of codimension 0 in case $p = 2$. Roughly speaking, in case $p = 2$, the Pareto front consists of a pieces of curves ending at points and the class corresponding to the left figure appears in the middle of such curves whereas one corresponding to the right figure appears on the edge of such curves. In this presentation, we will provide a comprehensive list of possible local geometries of Pareto sets and Pareto fronts for $n \geq p$ and for the pairs (n, p) in the nice region [1] up to diffeomorphism [2].
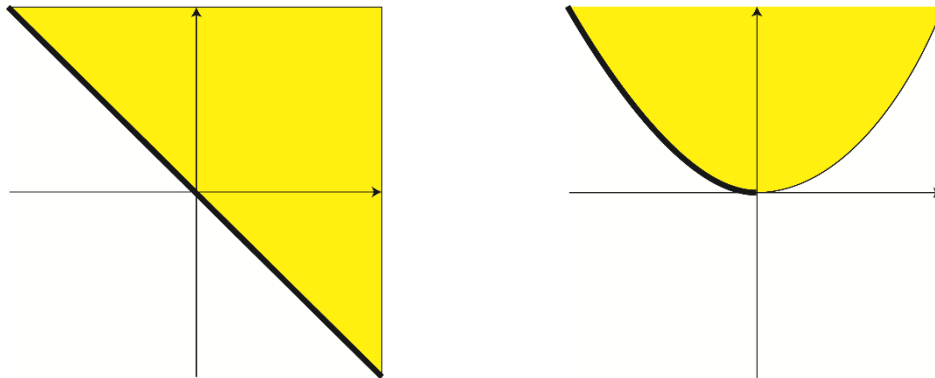
Figure (left, right): The image of f is indicated in yellow whereas its Pareto front is indicated in the thick black lines in the space $\mathbb{R}^p$.

In this analysis, we have obtained a comprehensive list of local geometries of Pareto sets and Pareto fronts for $n \geq p$ and for the pairs (n, p) in the nice region up to diffeomorphism. First of all, this analysis may be useful to understand all the possible trade-off relationships between mutually conflicting objectives. Second, this list may provide some insight on designing benchmark problems.

References
1. Mather, J. Lecture Notes in Mathematics, 192:207 (1971).
2. Teramoto, H. et al. in preparation.

Oxidative Steam Reforming of Ethanol over $M_xLa_{2-x}Ce_{1.8}Ru_{0.2}O_{7-\delta}$ (M = Mg, Ca) Catalysts: Effect of Alkaline Earth Metal Substitution and Support on Stability and Activity

Ho-Chen Hsieh,[1,3] Ping-Wen Tsai,[1] Yuan-Chia Chang,[1] Sheng-Feng Weng,[1] Hwo-Shuenn Sheu,[3,4] Yu-Chun Chuang,[4] Chi-Shen Lee[1,2*]

[1]Department of Applied Chemistry, National Chiao Tung University, 1001 University Rd., Hsinchu 30010, Taiwan, [2]Center for Emergent Functional Matter Science, National Chiao Tung University, Hsinchu 30010, Taiwan, [3]Graduate Degree Program of Science and Technology of Accelerator Light Source, National Chiao Tung University, Hsinchu 30010, Taiwan, [4]National Synchrotron Radiation Research Center, Hsinchu, 30010, Taiwan

Alkaline earth metal substitutions on the A-site of pyrochlore oxide $M_xLa_{2-x}Ce_{1.8}Ru_{0.2}O_{7-\delta}$ (M = Mg, Ca) were studied as catalysts for oxidative/autothermal steam reforming of ethanol (OSRE/ATR). The as-prepared oxides were synthesized by a combustion method and characterized using Powder X-ray diffraction (PXRD), X-ray photoelectron and absorption spectroscopy (XPS and XAS). PXRD Rietveld analysis and elemental analysis (ICP-AES) support the formation of a pyrochlore-type structure (space group Fd-3m) with the distorted coordination environment. The substitution of Mg^{2+} and Ca^{2+} ions affect the oxidation states of $Ce^{4+/3+}$ and Ru^{n+} ions and create oxygen vacancies, which leads to enhanced catalytic activity and reduced ethylene selectivity. A long-term stability test showed optimized catalysts $Mg_{0.3}La_{1.7}Ce_{1.8}Ru_{0.2}O_{7-\delta}$ and $Ca_{0.2}La_{1.8}Ce_{1.8}Ru_{0.2}O_{7-\delta}$ with $S_{H2} = 101(1)\%$ and $S_{H2} = 91(2)\%$ under OSRE. The initial operation temperatures were lower than that of the unsubstituted catalyst $La_2Ce_{1.8}Ru_{0.2}O_{7-\delta}$. Catalysts supported on $La_2Zr_2O_7$ showed stable OSRE/ATR performance and low carbon deposition compared to catalysts supported on Al_2O_3. We ascribe the enhanced activity to well-dispersed alkaline earth metal and Ru ions in a solid solution structure, synergistic effects of $(Mg, Ca)^{2+}/Ce^{3+,4+}/Ru^{n+}$ ions, and strong catalyst-support interaction that optimized the ethanol conversion and hydrogen production.

References
1. G. A. Deluga, J. R. Salge, L. D. Schmidt and X. E. Verykios, *Science*, 2004, **303**, 993-997.
2. S.-F. Weng, Y.-H. Wang and C.-S. Lee, *Appl. Catal., B*, 2013, **134-135**, 359-366.
3. H.-C. Hsieh, Y.-C. Chang, P.-W. Tsai, Y.-Y. Lin, Y.-C. Chuang, H.-S. Sheu and C.-S. Lee, *Catal. Sci. Technol.*, 2019, **9**, 1406-1419.

Fabrication of Porous Polyimide and Carbon Nanotubes Using Anodic Aluminum Oxide Templates

Hung-Chieh He[1], Yi-Hsuan Tu[1], Jia-Wei Li[1], Yu-Liang Lin[1], and Jiun-Tai Chen[1, 2]

[1] *Department of Applied Chemistry, National Chiao Tung University, Hsinchu 30010, Taiwan, and* [2] *Center for Emergent Functional Matter Science, National Chiao Tung University, Hsinchu 30010, Taiwan*

Polyimides (PIs) have good mechanical properties, excellent thermal stability, and good chemical resistance. In this work, we use anodic aluminum oxide (AAO) templates to prepare porous PI and carbon nanomaterials. AAO templates have regular nanochannels and the diameters and lengths of the nanochannels can be easily controlled. First, polyamic acid (PAA) solutions are used as precursors and infiltrated into the nanochannels of AAO templates, forming PAA nanotubes. Next, the PAA nanotubes are annealed in tetrahydrofuran (THF) and *N, N*-dimethylformamide (DMF) solvent vapors to fabricate porous PAA nanotubes; the pore lengths can be controlled by solvent vapors and annealing times. After the imidization processes at 300 °C, porous PI nanotubes can be obtained. Finally, the porous PI nanotubes can be further converted to porous carbon nanotubes by carbonization processes, which have potential applications in areas such as gas separation, capacitors, and energy storage devices.
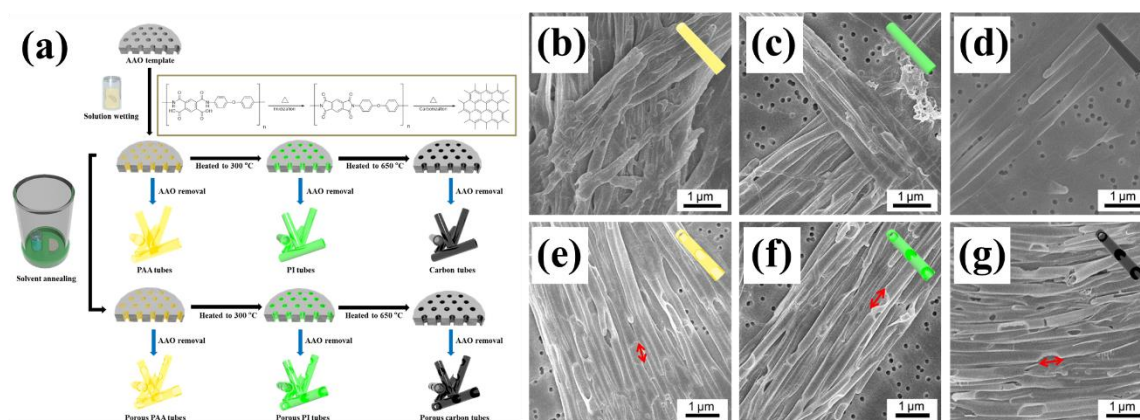
Figure 1. (a) Schematic illustration of the experimental processes. (b-d) SEM images of nonporous PAA, PI, and carbon nanotubes. (e-g) SEM images of porous PAA, PI, and carbon nanotubes.

The experimental processes to fabricate the nonporous and porous PAA, PI, and carbon nanotubes are illustrated in Figure 1a. Figure 1b-d shows the SEM images of the nonporous PAA, PI, and carbon nanotubes. After the solvent-annealing-induced transformation process using THF vapors at 40 °C for 24 h, porous PAA nanotubes can be observed (Figure 1e). After the imidization and carbonization processes, porous PI and carbon nanotubes can be formed (Figure 1f, g).

References

1.   H. C. He, Y. H. Tu, J. W. Li, Y. L. Lin, and J. T. Chen, *Macromol. Mater. Eng*, **2019**, *304*, 1800700.

# A Passive Driven Microfluidic Droplet Array for Optical Quantitative PCR Analysis

Pei-Heng Lin[1,2], Bor-Ran Li[1,3*]

[1]*Institute of Biomedical Engineering, College of Electrical and Computer Engineering, National Chiao Tung University, Hsinchu, Taiwan,*
[2]*Department of Electrical and Computer Engineering, College of Electrical and Computer Engineering, National Chiao Tung University, Hsinchu, Taiwan,*
[3]*Center for Emergent Functional Matter Science, National Chiao Tung University, Hsinchu, Taiwan.*

Traditional real-time fluorescence quantitative PCR has been recognized as a very useful and widely technique for amplifying and detecting target DNA and suitable for digital PCR analysis in applied to clinical and point-of-care testing(POCT) applications[1,2]. Here, we report an effective technology for optical quantitative PCR with passive driven microfluidic droplet-based assay. Such device is made by polydimethylsiloxane(PDMS) with outer channel and the reaction chamber. According to the gas permeability of PDMS, the microfluidic channel is covered with a waterproof layer and supporting layers in order to prevent water loss during the PCR heating reaction. Also, mineral oil is injected into the channel through the oil inlet that supplant adequate buffer out reserving PCR reagent in the reaction chamber. This passive assay only requires hand pipetting for the entire experimental process and external power system is not necessary. With designed microfluidic channel, buffer can be easily exchanged in the reaction chamber. Human mutant EGFR mRNA solution isolated from H1975 cell line is used as template to verify the accuracy of this method. Such simple, portable and self-priming microfluidic PCR biochip can be potentially widely used in clinical application as a real POCT technique.
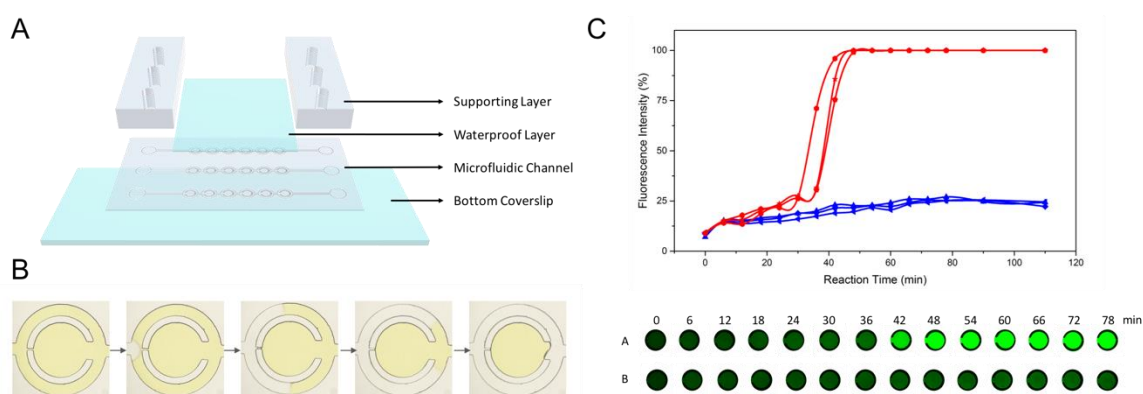
Figure. (A) Schematic diagram of the designed PCR biochip, showing different layers with different functions. (B) The oil cover process during the mineral oil injecting through hand pipetting. (C) the result and optical fluorescence image of detecting target mRNA (mutant EGFR) through passive driven microfluidic droplet array.

References

1. Park, S., Zhang, Y., Lin, S., Wang, T. H., & Yang, S. Biotechnology advances, 2011, 29(6), 830-839.
2. Zhang, L., Ding, B., Chen, Q., Feng, Q., Lin, L., & Sun, J. TrAC Trends in Analytical Chemistry, 2017, 94, 106-116.

Sequential Syntheses of Three-dimensional Flower-like Graphene–MnO₂–WO₃ Nanometer Architectures and Their use in Supercapacitors

Shih-Yu Huang[1,3], Sumanta Kumar Sahoo[1], Phuoc-Anh Lea[1], Po-Jen Yen,a
Yi-Chun Lu[1], Po-Wen Chiu[3], Tseung-Yuen Tseng[4], Kung-Hwa Wei[1,2]

[1]*Department of Materials Science and Engineering, National Chiao Tung University, 30010 Hsinchu 30010, Taiwan, and* [2]*Center for Emergent Functional Matter Science, National Chiao Tung University, 30010 Hsinchu 30010, Taiwan, and* [3]*Institute of Electronics Engineering, National Tsing Hua University, Hsinchu 30013, Taiwan, and* [4]*Institute of Electronics, National Chiao Tung University, Hsinchu 30010, Taiwan*

In this study, we synthesized new 10–300-nm graphene nanosheets–MnO₂–WO₃ (G/MnO₂/WO₃) architectures through electrochemical induced cathodic plasma formation in one batch at low temperature (70 ℃) for a short time (2 hours) as compared to those in a hydrothermal method. We first obtained 100-nm leaf-like graphene nanosheets (G), then 150-nm long and 10-nm diameter petiole-like MnO₂ nanowires on G, and finally 280-nm petal-like WO₃ on MnO₂/G—thereby forming the G/MnO₂/WO₃ architectures—as evidenced using scanning electron microscopy and transmission electron microscopy. The G/MnO₂/WO₃ architecture has surface area of 291 m2 g^{-1}—much higher than that of G/MnO₂ of 241 m^2 g^{-1} and of G of 59 m^2 g^{-1}— that provides suitable surface area for ions diffusion during the charging and discharging process. As a result, the electrode incorporating G/MnO₂/WO₃ architectures exhibits excellent specific capacitance of 620 F g^{-1}—45% and 200% higher than those of G/MnO₂ and G electrodes (421 and 189 F g^{-1}, respectively)—at a current density of 0.5 A g^{-1}. Moreover, the G/MnO₂/WO₃ electrode exhibits good cycling stability with 90% capacitance retention over 5000 cycles at 1 A g^{-1}. Such new G/MnO₂/WO₃ structures not only provide high-performance electrode applications but also provide a potential way to obtain high surface area, resulting in other high-performances.
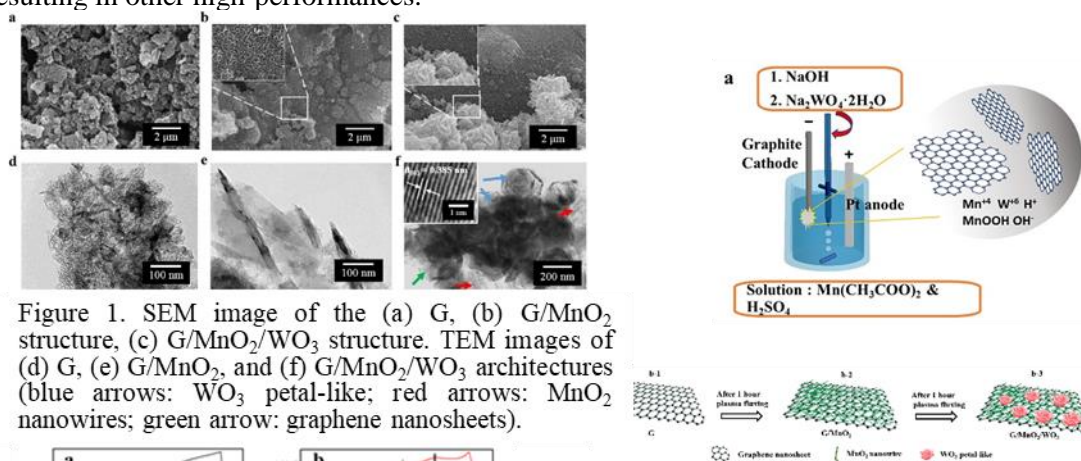

Figure 1. SEM image of the (a) G, (b) G/MnO₂ structure, (c) G/MnO₂/WO₃ structure. TEM images of (d) G, (e) G/MnO₂, and (f) G/MnO₂/WO₃ architectures (blue arrows: WO₃ petal-like; red arrows: MnO₂ nanowires; green arrow: graphene nanosheets).

Figure 2. (a) Schematic representation of the CPF method. (b) Syntheses of (b-1) G, (b-2) G/MnO₂, and (b-3) G/MnO₂/WO₃.
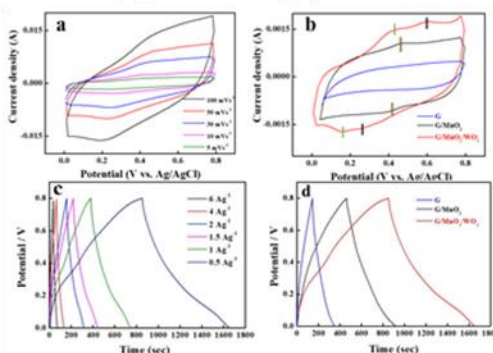

Figure 3. CV curves of (a) G/MnO₂/WO₃ recorded at scan rates of 5, 10, 30, 50, and 100 mV s^{-1} and (b) G, G/MnO₂, and G/MnO₂/WO₃ recorded at 5 mV s^{-1}. (c) GCD curves of G/MnO₂/WO₃ recorded at current densities of 0.5, 1, 1.5, 2, 4, and 6 A g^{-1}. (d) GCD curves of G, G/MnO₂, and G/MnO₂/WO₃ recorded at 0.5 A g^{-1}.

Block Copolymer/AAO Hybird Substrates for Surface-Enhanced Raman Scattering

Yu-Liang Lin[1], Ming-Hui Shen[1], Yi-Fan Chen[1], Jiun-Tai Chen[1]

[1]*Department of Applied Chemistry, National Chiao Tung University, Hsinchu 30010, Taiwan, E-mail: jtchen@mail.nctu.edu.tw*

Surface-enhanced Raman scattering (SERS) substrates with three-dimensional porous nanostructures have been developed for sensitive and reproducible approaches. In this work, a novel hybrid substrate with a spongy-like pore system of block copolymer layer supported on self-organized nanocavity arrays of anodic aluminum oxide (AAO) template is prepared. Gold nanoparticles (AuNPs) with an average size of 13 nm are anchored on the as-prepared porous hybrid substrates.
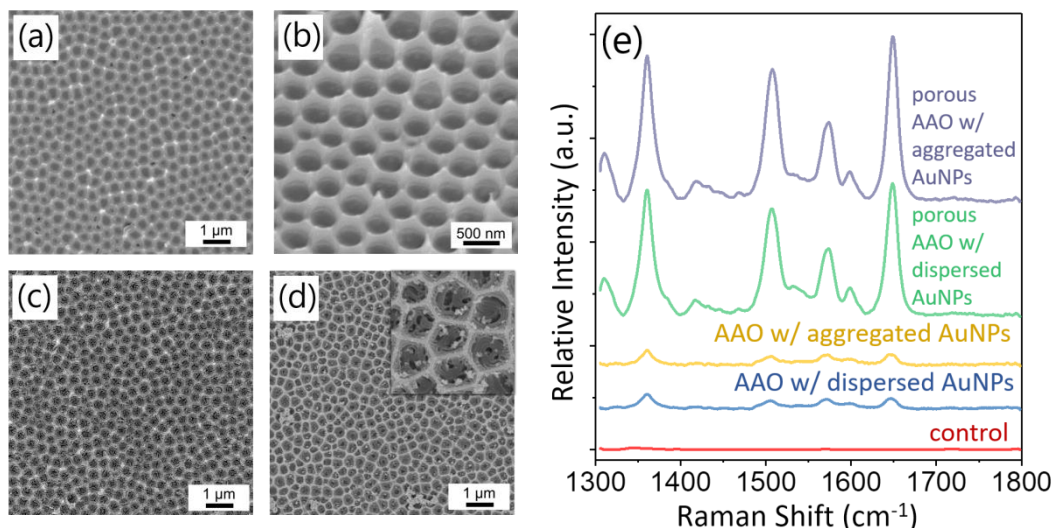
Figure 1. SEM images of the underlying concaved AAO templates: (a) Top-view and (b) 45◦ tilt-view. SEM images of the porous hybrid substrates: (c) before and (d) after anchoring with AuNPs. (e) SERS spectra of different substrates anchored with dispersed or aggregated AuNPs. The concentration of R6G molecules and the size of the AuNPs are 10^{-4} M and 13 nm, respectively.

Figure 1a and 1b show the SEM images of the AAO templates with self-organized nanocavity arrays fabricated by a traditional two-step anodization method. To generate a spongy-like pore system of the block copolymer layer, we apply the UV irradiation and the selective removal processes (Figure 1c). Also, the citrate-stabilized AuNPs can be anchored on the top of the porous block copolymer layer successfully, as shown in Figure 1d. The SERS spectra of the as-prepared substrates are displayed, and the bare AAO templates without a porous block copolymer layer are also shown for comparison in Figure 1e. The results reveal that the increase of the surface area and the generation of hot-spots resonance effects can strongly enhance the signal intensities.

In conclusion, we have successfully prepared a porous hybrid SERS substrate using PS-*b*-PMMA and AAO template. In comparison with bare AAO templates and flat surfaces, our porous hybrid substrate shows high-intensity enhancement because of strong near-field interaction induced by nanostructure. The enhancement factor (EF) is $\sim 10^4$ and the relative standard deviation (RSD) is less than 10%. This work may open a new avenue for the preparation of large-area and reliable SERS substrates.

Optical Transport of Fluorescent Nanodiamonds Inside a Tapered Glass Capillary

Christophe Pin[1], Ryohei Otsuka[1], Keiji Sasaki[1]

[1]*Research Institute for Electronic Science, Hokkaido University, N20, W10, Sapporo, Hokkaido 001-0020, Japan*

Optical forces result from the transfer of momentum from an incident light to a material object. Most famous for its application in optical tweezers[1], optical forces have also gain much attention for it could provide an efficient way to sort nanoparticles and molecules based on their optical properties[2-5]. However, in usual experimental conditions optical forces acting on nanoparticles are too weak or too localized to allow for efficient optical sorting of a large ensemble of nanoparticles dispersed in a liquid solution.

In order to address this issue, we investigate in this work the fabrication and the use of tapered glass capillaries for nanoparticle optical manipulation and sorting applications. We first report on the fabrication of micro- and sub-micrometer scale glass capillaries by heating and pulling method. After filling a tapered capillary with an aqueous colloidal dispersion of red-fluorescent nanodiamonds, a 532 nm green laser light is coupled into the capillary. The tapered capillary acts thus both as a microfluidic channel and as an optical waveguide. This allows for enhanced light-nanoparticle interactions over a distance reaching few millimeters. We used an incident laser power of few tens of milliwatts to demonstrate optical transportation of 100 nm nanodiamonds inside few-micrometer-large capillaries. Particle velocities reaching few tens of micrometers per second were achieved. After investigating the power-dependence of the optical transport, a quantitative analysis of the optical force and the hydrodynamical drag force acting on the propelled nanodiamonds is performed. Nanoparticle sorting is also demonstrated by balancing the optical transport of the nanodiamonds with a liquid flow in the opposite direction. Our results evidence how thin tapered glass capillaries can advantageously be used to sort nanoparticles according to their size.

Owing to their unique geometry, the use of tapered glass capillaries as optofluidic platforms is expected to enable further investigation and progress in optofluidics.

References
1. A. Ashkin, J. M. Dziedzic, J. E. Bjorkholm, and S. Chu, *Opt. Lett.,* **1986**, *11*, 288−290.
2. T. Imasaka, Y. Kawabata, T. Kaneta, and Y. Ishidzu, *Anal. Chem.,* **1995**, *67*, 1763−1765.
3. S. E. S. Spesyvtseva, S. Shoji, and S. Kawata, *Phys. Rev. Appl.,* **2015**, *3*, 044003.
4. Y. Shi, S. Xiong, L. K. Chin, J. Zhang, W. Ser, J. Wu, T. Chen, Z. Yang, Y. Hao, B. Liedberg, P. H. Yap, D. P. Tsai, C.-W. Qiu, and A. Q. Liu, *Sci. Adv.,* **2018**, *4*, eaao0773.
5. G. Tkachenko, E. Brasselet, *Nat. Commun.,* **2014**, *5*, 3577.

Plasmonic Optical Trapping of Molecular Nano-aggregates   P07

Kenji Setoura, Yu Kitamura, Yohei Nishikawa, Keiji Sasaki

Research Institute for Electronic Science, Hokkaido University, N20, W10, Sapporo, Hokkaido 001-0020, Japan

Optical trapping has attracted much attention as a non-contact method for capturing and analyzing micron-sized objects. Optical forces acting on the small object under light illumination can be divided into the following three terms[1]; gradient force (F_{grad}), scattering force (F_{sca}), and absorption force (F_{abs}). As shown in Figure 1a, F_{grad} acts as attractive force to the object and traps it at a focal point of a tightly focused Gaussian laser beam, while F_{sca} and F_{abs} slightly push the object along the axis of laser propagation. To make the optical trapping stable, one needs to minimize the laser focal spot as small as possible because F_{grad} is proportional to spatial gradient of light intensity. For this purpose, use of localized surface plasmon (LSP) has been proposed recently[2,3]. As LSP is evanescent fields on noble metal nanostructures, the gradient of light intensity is free from restriction of diffraction limit, enabling F_{grad} stronger. Therefore, optical trapping with plasmonic nanostructures may offer opportunities for capturing nanometer-sized objects in solution.

In the present work, we examined optical trapping of molecular nano-aggregates using plasmonic nanostructures, and modulation of their emission behavior with the optical forces. As a molecule, we used hexaphenylsilole (HPS). This molecule is non-emissive while dissolved in solution, and turns into emissive when aggregated because of restriction of intramolecular rotations[4]; the emission behavior could be modulated with the optical forces. For the optical trapping, we fabricated a dimer structure of gold nanosquares on a glass cover slip with electron beam lithography, as shown in Figure 1b. The length of the square is 140 nm and the gap distance between the dimer is ca. 10 nm. This nanostructure exhibits the gap-mode plasmon resonance at a wavelength of 1064 nm. In the poster session, we will present results on the plasmonic optical trapping of HPS in a binary solution of water and tetrahydrofuran (THF).
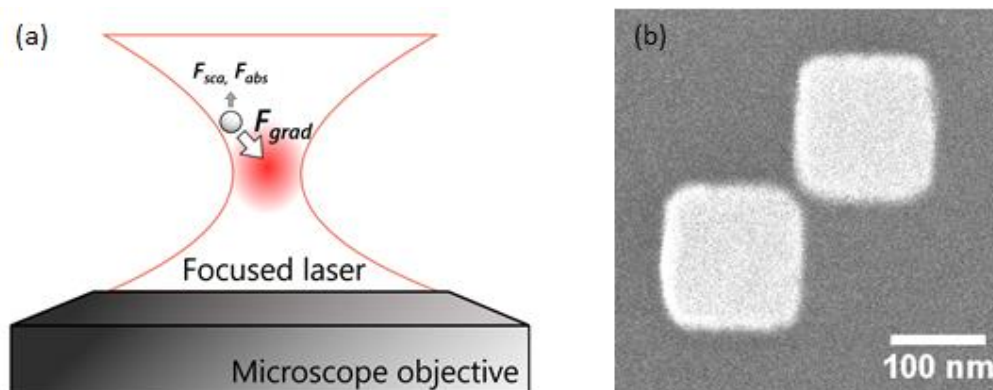

Figure 1. (a) Schematic representation of the optical forces.
(b) Scanning electron microscopy image of the gold dimer nanostructure.

References
1. A. Ashkin, *IEEE J. Selected Topics Quantum Electronics*, **2000**, *6*, 841−856.
2. M. L. Juan et al., *Nature Photonics*, **2011**, 5, 349-356.
3. Y. Tanaka, K. Sasaki, *Opt. Express*, **2011**, 19, 17462-17468.
4. Y. Hong et al., *Chem. Soc. Rev.*, **2011**, 40, 5361-5388.

Particle Tracking of Individual Nanoparticles Using Chemical Fingerprint

Han Wen[1], Tomoko Inose[1], Tatsuya Ogawa[1], Beatrice Fortuni[2], Susana Rocha[2], Kenji Hirai[1], Hiroshi Uji-i[1,2]

[1]*Research Institute for Electronic Science, Hokkaido University, N20, W10, Sapporo, Hokkaido 001-0020, Japan,* [2]*KU Leuven, Celestjinenlaan, 200 F 3001, Heverlee, Belgium*

Single nano-particle tracking (SPT) in both time and spatial domain is highly desired in modern biology[1]. Based on different principles, nanoparticles such as semiconductor quantum dots, and nonfluorescent surface-enhanced Raman scattering (SERS) nanoparticles have been used to achieve SPT. Comparatively, SERS possesses higher molecular sensitivity, which enables the development of so-called SERS barcoding. SPT can be achieved by decoding SERS signal of the SERS reporter-encoded nanoparticles.

Cancer metastasis is essentially cell migration and proliferation, in which the integrin-mediated adhesion plays a crucial role. It is believed that altered integrin expression is related to many kinds of cancer, however, the specific role of integrin is still unrevealed[2]. To track integrin, SERS reporter-marked nanoparticle can be introduced. The nanoparticle can be connected to integrin through specific peptide, and the integrin tracking can be indirectly achieved by tracking the nanoparticle. However, most of the SERS reporter molecules are harmful to cell, and the complicated intracellular environment could also interfere the detection of target nanoparticle. In this research, mesoporous silica (MS) coating is applied to the SERS reporter-functionalized nanoparticles (Au nanostar), as shown in figure 1, aiming to track the integrin with low cytotoxicity and high sensitivity.

In the SERS reporter functionalization part, 4 chemicals, including 4-mercaptobenzoic acid (4-MBA), 2-naphthalenethiol, 5,5'-dithiobis-(2-nitrobenzoic acid) (DTNB), and $H_{12}SC_6O$-azobenzene were selected. The spectra of them are shown respectively in red, blue, pink, and purple in figure 2. Obviously, these chemicals possess high Raman activity, and their spectra have different characteristic peaks. After SERS reporter functionalization, the MS coating has been achieved. One of the innovative points of this project is the SERS activity after MS coating. The SERS signal can be detected after coating, shown as the orange spectrum in figure 3, which convinces the feasibility of this project.
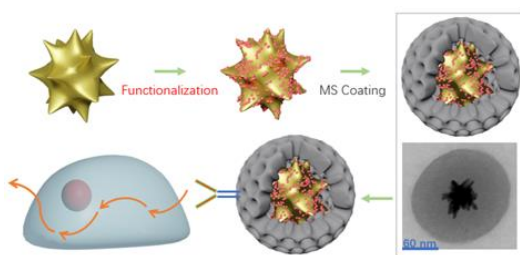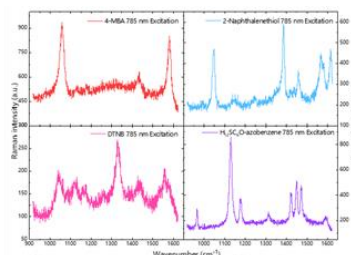

Fig. 1. Research Scheme

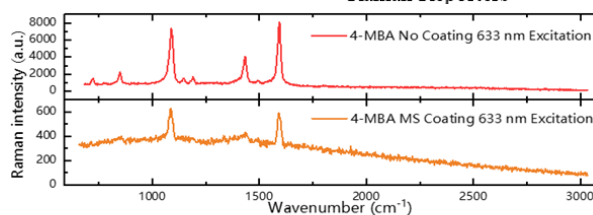Fig. 2. SERS Spectra of Various Raman Reporters

Fig. 3. SERS Spectra of 4-MBA with and without MSNP Shell

In conclusion, this project mainly consists of four parts, including the synthesis of gold nanostar, the SERS reporter functionalization, the MS coating and intracellular tracking. Until now, the first three parts have been covered. In future research, the single particle tracking will be carried out in order to study the migration of integrin under both time and spatial dimension.

References

1. D. Lasne, G. A. Blab, and S. Berciaud, et al, *Biophysical Journal.*,**2006**, *91*, 4598-4604.
2. J. S. Desgrosellier, D. A. Cheresh, *Nat Rev Cancer.*,**2010**, *10*, 9-22.

Intracellular Time-lapse Observation of Mesoporous Silica Nanoparticles

Ibuki Kotani[1], Tomoko Inose[1], Beatrice Fortuni[2], Indra Van Zundert[2], Kenji Hirai[1], Hiroshi Uji-i[1,2]

[1]RIES, Hokkaido University, Sapporo, 001-0020, Japan
[2]KU Leuven, Celestijnenlaan 200F 3001 Leuven, Belgium

Anti-cancer drugs used in cancer chemotherapy act not only on cancer cells but also on normal cells, leading to various side effects. To address this issue, drug delivery systems (DDS) has been developed as a technique to concentrate a required amount of anticancer agents mainly at the targeted sites. In recent years, mesoporous silica nanoparticles (MSNP) has attracted attention as drug.

We have developed the surface modification of MSNP with polyethyleneimine (PEI) and hyaluronic acid (HA) to target lung cancer cells. Confocal fluorescence microscopy has been used to visualize uptake and distribution of the surface-modified MSNP inside the cancer cells. However, the diffusion of MSNP inside and outside the cells has not been clarified. Therefore, in this study, we decided to observe uptake dynamics of MSNP using fluorescent microscopy.

MSNP was synthesized by biphase method using tetraethylorthosilicate (TEOS), cetyltrimethylammonium chloride (CTAC), triethanolamine (TEA) and 1-octadecene. Rhodamine B as a fluorescent dye and Doxorubicin (Dox) as an anticancer agent were added to MSNP dispersion and stirred overnight. Layer by layer method was used for surface modification of MSNP. Positively charged polyethylenimine (PEI) was coated on the negatively charged MSNP surface by electrostatic interaction. Then, hyaluronic acid (HA) that is a ligand for the CD44 receptor overexpressed in specific cancer cells were bound to the peptide bond using the EDC (1-Ethyl-3-(dimethylaminopropyl)carbodimer) coupling. These MSNPs were added to A549 cells and fluorescence observation was performed using a confocal microscope.

Time lapse observation by confocal microscopy revealed that MSNP adhered to the cell membrane after 15 minutes and began to be taken in the cell. It was revealed that after 90 minutes many particles accumulated in the cell nucleus (Fig. 1).
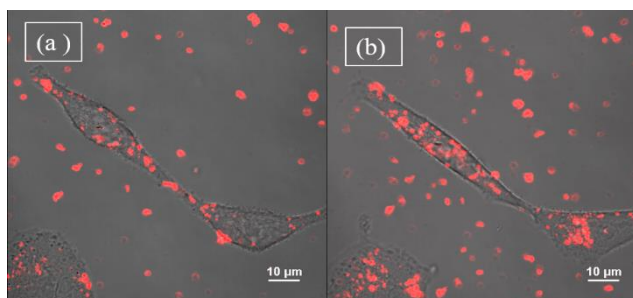
In contrast, when Dox was directly added to the cells, fluorescence was observed from the cell nucleus and the whole cytoplasm after 3 hours. The fluorescence from the nucleus was quenched after 24 hours (Fig. 2). On the other hand, when MSNP containing Dox was added to the cells, fluorescence from the cell nucleus was not observed neither 3 hours nor 24 hours (Fig. 3).

Fig. 1 State of intracellular diffusion of MSNP. (a) 15 minutes and (b) 90 minutes after addition of MSNP

In conclusion, we successfully observed the intracellular diffusion of MSNP containing Rhodamine B. The microscopic observation indicated that MSNP carried Dox to the cancer cell and slowly released Dox near the nucleus of the cancer cell. These results suggest that anticancer drugs delivered by MSNP can suppress the side effects.
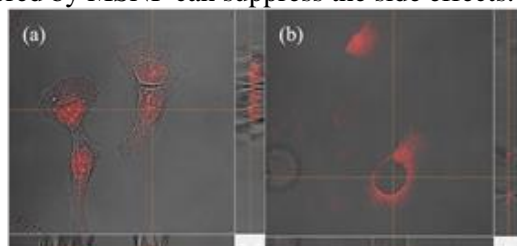

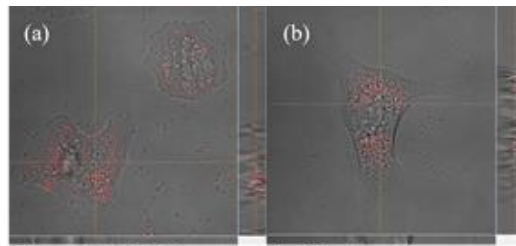Fig. 2 CLSM images of cells. (a) 3 hours after addition of Dox (b) 24 hours after addition of Dox

Fig. 3 CLSM images of cells. (a) 3 hours after addition of MSNP_Dox (b) 24 hours after addition of MSNP_Dox

Coating of Metal Nanowire with Metal-organic Framework for Size-selective Surface-Enhanced Raman Scattering

Taku Murasugi[1], Kenji Hirai[1], Tomoko Inose [1], Hiroshi Ujii [1,2,]

[1]RIES, Hokkaido University, Sapporo, 001-0020, Japan
[2]KU Leuven, Celestijnenlaan 200F 3001 Leuven, Belgium

In order to unveil the behaviors of cells, it is important to detect specific molecules in living cells with high spatial resolution. Surface-enhanced Raman scattering (SERS) by metal nanomaterials is a promising way to analyze a tiny amount of molecules. Recently, we developed a technique to insert metal nanowires into living cells to obtain SERS spectrum of the molecules therein.[1] However, it is still difficult to analyze the specific molecules from SERS spectra consisting of the mixtures of various molecules. To address the issue, we fabricated metal nanowires coated with metal-organic framework (MOF) [2] [3]. Specific molecules are selectively adsorbed by MOF and diffuse to the surface of metal nanowires. Thanks to the synergy of selective adsorption by MOF and molecular detection by metal nanowire, MOF-coated nanowires enable to obtain SERS spectra of only the molecules that can pass through the micropores of MOF.
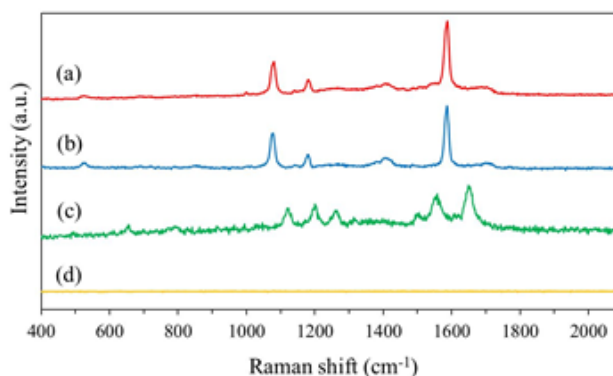
Silver nanowires (AgNW) were synthesized by the polyol method. The obtained AgNW was heated in chloroauric acid (Au-AgNW). After that, Au-AgNW was stirred with ethanol solution of 2-methylimidazole and zinc acetate dihydrate in an ice bath to coat ZIF-8 on the surface of Au-AgNW (Au-Ag@ZIF-8NW).

Au-Ag@ZIF-8NW was observed by scanning electron microscope (SEM). The elemental mapping of Ag, Au and Zn by energy dispersive X-ray spectrometry (EDX) suggests Au-etched Ag nanowire was coated with ZIF-8 composed of Zn^{2+}.

Fig. 1. Raman spectra of (a) 4-MBA on Au-AgNW and (b) 4-MBA on Au-Ag@ZIF-8NW, (c) GSH on Au-AgNW and (d) GSH on Au-Ag@ZIF-8NW.

The crystals of ZIF-8 grown on metal Au-AgNW was also observed by scanning transmission electron microscope (STEM). powder X-ray diffraction (XRD) patterns of Au-Ag@ZIF-8NWs corresponds to the superposition of Ag and ZIF-8, indicating that crystals grown on nanowires are ZIF-8. These results indicate that Au-Ag@ZIF-8NWs were successfully obtained.

SERS spectra of 4-MBA were obtained by both of Au-AgNW and Au-Ag@ZIF-8; however, SERS spectrum of GSH was obtained by only Au-AgNW (**Fig. 1**). ZIF-8 can adsorb 4-mba but cannot absorb larger GSH; thus only 4-mba was detected by Au-Ag@ZIF-8.

In this work, we succeeded to obtain the SERS signal of only the molecules that can pass through the pores of ZIF-8. It is expected that various molecules can be selectively detected by coating nanowires with MOF suitable for the target molecules.

References

1. G. Lu *et al. Adv. Mater.* **26**, 5124 (2014)
2. M. Kondo et al. Angew. Chem. Int. Ed. **36**,1725 (1997)
3. H. Lietal. J. Am. Chem. Soc. **120**, 8571 (1998)

Tip-enhanced Raman Spectroscopy on Chemically Unzipped Carbon Nanoribbon

Shoji Sugioka, Tomoko Inose, Shinnosuke Hara, Shuichi Toyouchi, Peter Walke,
Kenji Hirai, Yasuhiko Fujita, Hirofumi Tanaka, Hiroshi Uji-i

[1]RIES,-Hokkaido-University,-Sapporo,-001-0020,-Japan
[2]KU-Leuven,-Celestijnenlaan-200F-3001-Leuven,-Belgium

Graphene is a graphite layer with a thickness of one atom, which shows excellent carrier mobility, mechanical strength, and flexibility. Graphene is usually a conductor without a band gap. However, when the sheet-like graphene is changed to a fine ribbon-like graphene nanoribbon (GNR), a band gap could formed by a quantum confinement effect while keeping the physicochemical properties of graphene. GNR is thus a promising candidate for next-generation semiconductor materials. Such GNR can be produced using chemically unzipped GNR[1]. The purpose of this work is to elucidate the electronic state and edge structure of chemically unzipped GNR using a Tip-enhanced Raman scattering(TERS) microscope capable of obtaining molecular information at nanosclae..

  GNRs were obtained by chemically unzipped double-walled carbon nanotubes (DWNTs) with diameters of 3–15 nm. Shortly, the DWNTs were annealed at 500 °C to induce defects and then dispersed in 1,2-dichloroethane containing poly(m-phenylenevinylene-co-2,5-dioctoxy-p-phenylenevinylene) (PmPV). The solution was sonicated for 5 h at 600 W to obtain unzipped single-layered GNRs (sGNRs). Then the solution was ultracentrifuged at 50300 G for 2 h to remove any unzipped nanotubes as well as the amorphous carbon-like impurities. The supernatant was then spin-cast onto a Au(111) substrate and the substrate was annealed at 350 °C for 1.5 h to remove PmPV prior to TERS measurement. TERS measurements were performed on an Omegascope™ with a home-made Raman scattering spectroscopic platform. Laser light from a He-Ne laser (632.8 nm) was focused onto the sample/tip for TERS mapping experiments.

  From one DWNT, two GNRs will be produced, namely from outer and inter nanotubes. Generally, the width of GNR from outer nanotube is greater than that of inner nanotube. Figure (a) shows an AFM image of y-shaped GNRs, in which two-layered GNR, single layer of outer and inner GNRs are visible at bottom, upper left, and upper right of the image, respectively. Figure (c) displays TERS spectrum on doubled GNR. The spectrum shows the prominent peaks of GNRs, D-band (~ 1580 cm^{-1}) and G-band (~1600 cm^{-1}). TERS

Figure. AFM image of GNR dispersed on an Au(111) substrate. (b) TERS mapping image of GNR. (c) TERS spectrum obtained on GNR.

mapping of corresponding peaks is shown in Figure (b). The image was merged with the D-, G-band maps in magenta and blue, respectively, with arbitrary intensities. The TERS mapping clearly indicates that the D-band was observed only on the outer GNR, while G-band was observed on the inner GNR. From this result, we expect that first annealing process of DWNTs induce defects on the surface of outer DWNT, while less defects were induced on the surface of inner DWNTs.

  TERS mapping of y-shaped GNR indicate that D-band was mainly observed only from GNRs from outer layer of DWNT, while GNR from inner nanotube shows mainly G-band, indicating good quality of GNR without defects. Since D-band corresponds to the chemical and physical defect of GNR, we can conclude first annealing process of DWNT induce many defects on outer nanotubes but not on inner nanotubes. As such, TERS measurements allow us to reveal the reaction mechanism of unzipping process of DWNT at nanoscale. In future, chemical/physical condition of GNR will be investigated using TERS.
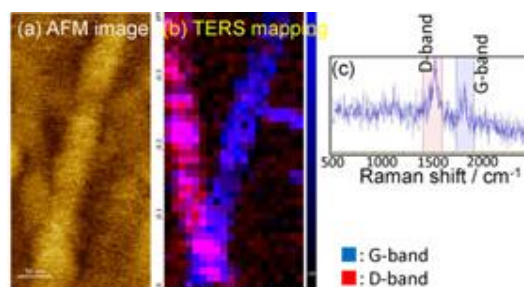
References

1. H. Tanaka et al., Sci. Rep. 5, 12341 (2015).

End-shape Engineering on Metal Nanowires

Taiki Akashi [1], Tomoko Inose[1], Shuichi Toyouchi[2], Kenji Hirai[1], Hiroshi Uji-i[1,2]

[1]*RIES, Hokkaido University, Sapporo, 001-0020, Japan*
[2]*KU Leuven, Celestijnenlaan 200F 3001 Leuven, Belgium*

Silver nanowires (AgNWs) are one of the most interesting and useful metal nanostructures due to their unique electronic, thermal, and optical properties. The development of AgNWs synthesis has been incentivized. However, less attention has been paid to control of the end morphology. In this contribution, we introduce an active engineering of AgNW end
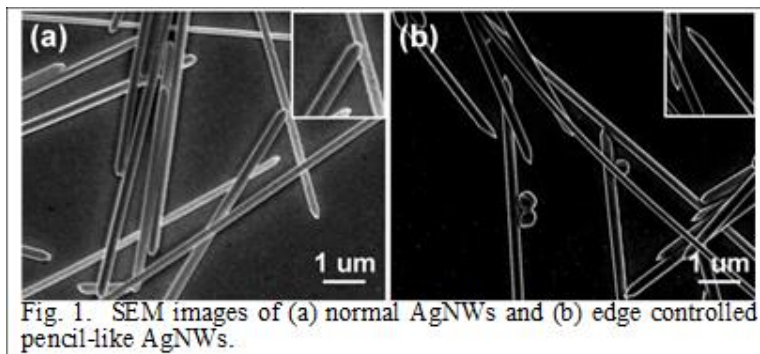
Fig. 1. SEM images of (a) normal AgNWs and (b) edge controlled pencil-like AgNWs.

morphology to enhance and control NLO response.[1] We will show a critical effect of a trace amount of water added in the polyol reaction on end morphology. An appropriate amount of water in the synthesis provides AgNWs with very sharp end morphology in the yield over 90%. Briefly, ethylene glycol (EG) were refluxed with Polyvinylpirrolidone K30 (PVP). CuCl2 EG solution was then added to this solution followed by adding of silver nitrate ($AgNO_3$) EG solution and stirring . After the solution color turns greenish, of $AgNO_3$ EG solution was added drop-wise, and the reaction mixture was further refluxed. After the reaction, the mixture was cooled down to room temperature under ambient condition. After the process, the mixture was washed with ethanol by centrifuged the solution. For the investigation of the effect of milli-Q during the reaction, small amount of milli-Q water were added in EG during the synthesis. All the solution preparation and synthesis were performed at humidity of ~ 20%. First, we performed a standard polyol synthesis of AgNWs. Briefly, $AgNO_3$ EG solution was added drop-wise at an injection rate of 100 µL/min into a pre-refluxed EG solution of PVP in the presence of $CuCl_2$. The reaction solution was further kept after injecting all the $AgNO_3$ solution. We obtained AgNWs with a typical length of 10 to 50 µm and averaged diameter of 200 ± 48 nm (Fig. 1(a)). In the second synthesis, a small amount of Milli-Q water was mixed with EG in advance, and this mixed solvent was used for all the precursor solutions. Except for adding water, the synthesis protocol was identical to the first synthesis. As seen in the SEM image of AgNWs synthesized in the presence of 0.2 % (v/v) water (Fig. 1(b)), most of AgNWs possess very sharp end morphology. We estimated to be more than 90 % of AgNWs with sharp-end and less than 10 % with trapezoid-like morphology. NLO response is sensitive to nanoscale structural change. Since the end morphology of AgNWs is successfully controlled, we investigated dependence of end morphology on SHG properties of AgNWs.

In conclusion, synthesis of AgNWs with sharp ends has been developed through the slight modification of the well-known polyol synthesis. We found that water content in the solvent in the synthesis is the key to control end morphologies of AgNWs. The end shape can be controlled by varying the amount of water in the reaction solution. Appropriate amount of water (0.2 ~ 0.4% (v/v)) together with proper reaction time (1 hour) provide pencil-like AgNWs with sharp end morphology in excellent yield over 90%. As an application, nonlinear optical effect, i.e. SHG, on the sharp nanowires was investigated. The SHG can be remotely generated through propagating plasmons on AgNWs. SHG emitted from a nanowire end shows uni-directional Poynting vector along the long axis of AgNWs. We suggest that the sharp-end AgNWs are suitable for nonlinear plasmonic applications, such as super resolution nonlinear optical microscopy and spectroscopy.

References

1. T. Inose, S. Toyouchi, G. Lu, K. Umemoto, Y. Tezuka, B. Lyu, A. Masuhara, E. Fron, Y. Fujita, K. Hirai, H. Uji-i, *Chem. Commun.*, **2019**, *55*, 11630.

Deposition of Gold Nanoparticles on Silver Nanowires for Nano-

Heat Source

Yusuke Nakao[1], Toyouchi Shuichi[2], Kenji Hirai[1], Tomoko Inose[1], Hiroshi Uji-i[1,2]

[1]RIES, Hokkaido University, Sapporo, 001-0020, Japan
[2]KU Leuven, Celestijnenlaan 200F 3001 Leuven, Belgium

Under illumination at the plasmonic resonance wavelength, gold nanoparticles (AuNPs) absorb the incident light and turn the photon energy into heat, so-called photothermal effect[1]. One way to utilize the photothermal effect of AuNPs for nano-heat source is to deposit AuNPs on nanowires so that the spatial position of AuNPs is controlled by manipulating the nanowires. The spatial control of AuNPs enable to deliver the heat to the desired positions. In this work, we demonstrate a facile means to fabricate AuNPs on silver nanowires (AgNWs) using photoreduction of AuNPs. The laser (488nm) focused on AgNW facilitates photoreduction of gold ions to form AuNPs on AgNWs. The resulting AuNPs on AgNWs convert the photon energy to heat. The increase of temperature is visualized by formation of bubbles in water, indicating the temperature to reach the boiling point.

AgNWs were synthesized by polyol method[2]. For fabrication of AuNPs on AgNW, 3 µM aqueous solution of tetrachloroauric(III) acid (pH = 11) were dropped on the glass substrate where AgNWs were dispersed. AuNPs were fabricated on AgNWs in aqueous solution of tetrachloroauric(III) acid under irradiation of laser (488nm). AuNPs deposited on AgNWs were clearly observed by scanning electron microscope (SEM) (**Fig. 1a**). Mapping of energy dispersive X-ray spectra (EDX) showed gold deposited at the position where the laser was focused (**Fig. 1b**). The laser (633 nm) was irradiated at AuNPs on AgNWs to excite the plasmon resonance of AuNPs. The bubble was formed soon after the laser was irradiated on AuNPs (**Figs. 1c**), indicating the temperature reached the boiling point of water (100 °C) by heating from AuNPs. This is because AuNPs on AgNWs converted the light energy to heat.
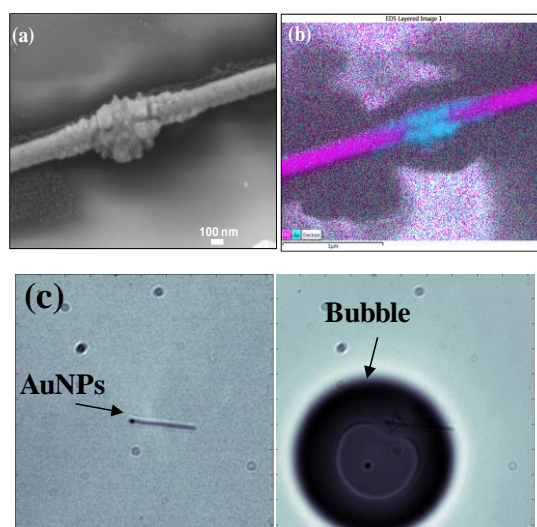
Fig. 1 (a)SEM image of AuNPs on AgNW, (b)EDX mapping: superposition of Au and Ag, (c)Microscopic images of AuNPs on AgNWs (left) and after laser irradiation (right).

References

1. Ndukaife, J. C., Shalaev, V. M. and Boltasseva, *A. Plasmonics-turning loss into gain.* 334, 6271 (2016).

2. Korte, K. E., Skrabalak, S. E. and Xia, Y., *J. Mater. Chem.*, 18, 437-441 (2018).

SERS-based pH Sensors with Highly Reduced Cytotoxicity P14

Qiang Zhang[1], Kiri Watanabe[1], Ibuki Kotani[1], Beatrice Fortuni[2], Taemaitree Farsai[3], Hitoshi Kasai[3], Johan Hofkens[2], Kenji Hirai[1], Tomoko Inose[1], Hiroshi Uji-i[1,2]

[1]RIES, Hokkaido Univ., [2] KU Leuven, [3] IMRAM, Tohoku Univ.

Intracellular pH plays an important role in cell functions, such as apoptosis, endocytosis, etc.[1] Understanding and manipulation of pH may have considerable potential in therapy and the reliable and sensitive local cellular pH sensing is required for this end. Surface-enhanced Raman scattering (SERS) has been widely used for pH sensing. Silver nanoparticles are ideal SERS substrate since chemical enhancement is required. However, silver nanoparticles suffer from the cytotoxicity. We have developed a simple method to coat silver nanoparticles with very thin gold layer on a polydimethylsiloxane film, which shown strong SERS activity at visible light frequency.[2] Here, we applied this coating method to silver nanoflowers (AgNFs) to realize local pH sensing with low toxicity in live cell, employing 4-mercaptobenzoic acid (4-MBA). We successfully obtained AgNFs with good dispersity in aqueous solution. The SEM image confirmed the flower-like morphology. (Fig. 1A) Gold coated silver nanoflowers (AuAgNFs) was obtained by adding L(+)-ascorbic acid at pH 11 to suppress the silver nanoparticles induced toxicity. SEM image revealed AuAgNFs maintained the flower-like morphology. (Fig. 1B) The enhancement factors of SERS activity for both AgNFs and AuAgNFs achieved 10^5(Fig. 2A), revealing the AuAgNFs possessed strong SERS activity at visible light region. Cell viability of A549 cells incubated with AgNFs and AuAgNFs for 24 h was investigated, 38.5 ± 3.0 % for AgNFs, 98.9 ± 3.1 % for AuAgNFs, revealing the AuAgNFs have a
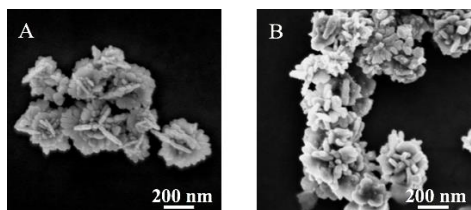

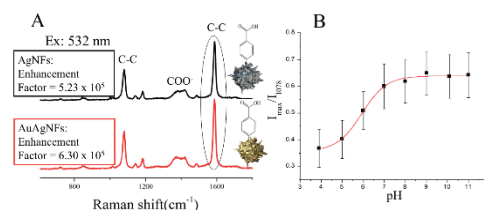Fig. 1 SEM images of Ag NFs (A) And AuAgNFs (B).

Fig. 2 SERS activities of AgNFs and AuAgNFs. (A) pH calibration curve by 4-MBA-AuAgNFs. (B)

very low toxicity. We investigated the pH responses for 4-MBA functionalized AuAgNFs (4-MBA-AuAgNFs) and gold coated silver nanoparticles (4-MBA-AuAgNPs), in PBS buffer solution. It was found that the pH-sensitive COO^- stretching band shown two components in SERS spectra at higher pH level for both AuAgNPs and AuAgNPs, in which the first component is bounded and the second component is unbounded. The calibration curve to calculate intracellular pH was constructed using the ratio between the maximum intensities of the pH-sensitive COO^- stretching band and the pH-insensitive benzene ring breathing band based on AuAgNFs, which is more sensitive at intracellular pH range. (Fig. 2B) The probes based on AuAgNPs possessed a more broad pH sensing range, which could be originated from the higher pKa value of the 4-MBA on AuAgNPs resulted from smaller curvature of the AuAgNPs. Indeed, one can design the pH sensors on-demand according to this finding. Finally we recorded intracellular SERS spectra with different incubation time for A549 cell. The intracellular pH decreased with time went by most likely due to the transfer of 4-MBA-AuAgNFs from endosome to lysosome, indicating it can be used to monitor the pH of live cells. The designed pH nanoprobe should have great potential for single cell analysis on account of the low cytotoxicity and strong SERS enhancement capability.

References
1. J. Shangguan, D. He, X. He, K. Wang, F. Xu, J. Liu, J. Tang, X. Yang and J. Huang, *Anal. Chem.*,**2016**, 88, 7837-7843.
2. B. Fortuni, T. Inose, S. Uezono, S. Toyouchi, K. Umemoto, S. Sekine, Y. Fujita, M. Ricci, G. Lu, A. Masuhara, J. A. Hutchison, L. Latterini and H. Uji-i, *Chem. Commun.*,**2017**, 53, 11298-11301.

Controlled Environment Nano-Imaging Free From Radiation P15

Damage by X-ray Laser Diffraction

Yoshinori Nishino[1], Akihiro Suzuki[1], Yoshiya Niida[1],
Yasumasa Joti[2], Yoshitaka Bessho[3]

[1]*Research Institute for Electronic Science, Hokkaido University, Kita 21 Nishi 10,
Kita-ku, Sapporo 001-0021, Japan, [2]Japan Synchrotron Radiation Research Institute
(JASRI)/SPring-8, 1-1-1 Kouto, Sayo-cho, Sayo-gun, Hyogo 679-5148, Japan, and
[3]Institute of Biological Chemistry, Academia Sinica, 128, Academia Road Sec. 2,
Nankang, Taipei 115, Taiwan*

X-rays are a powerful probe for imaging deep inside thick objects under various environmental conditions due to their high penetrating power. The ultrashort pulse duration of X-ray free-electron lasers (XFELs) adds a new possibility to achieve higher spatial resolution imaging free from radiation damage. Coherent diffractive imaging (CDI) is a lensless nano-imaging technique and is suitable for XFEL. The authors have developed a method to image nanoparticles in solution under controlled environmental conditions, pulsed coherent X-ray solution scattering (PCXSS)[1], using XFELs and image reconstruction algorithms in CDI. By using a tighter focused XFEL beam, higher spatial resolution can be achieved[2]. A unique feature of PCXSS is to keep solution samples under a controlled environment in micro-liquid enclosure array (MLEA) chips fabricated using photolithography techniques in-house at Hokkaido University[3]. We present the basics of PCXSS and examples of PCXSS measurement, for living cells[1] and self-assemblies of gold nanoparticles[4], performed using SACLA. Industrial applications of PCXSS are also described[5,6].
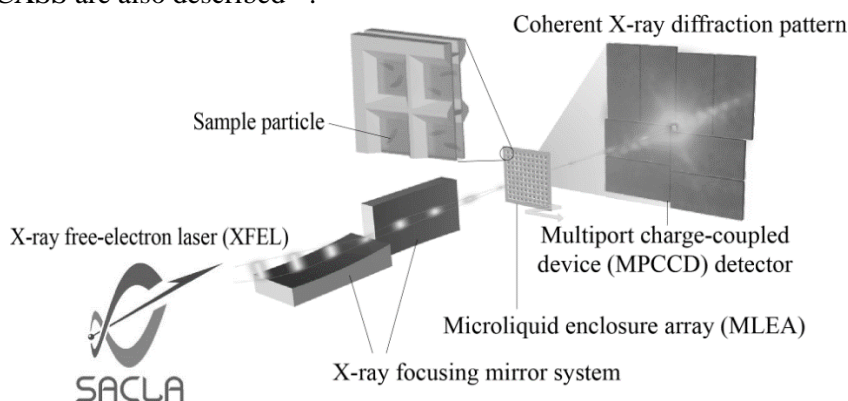
Fig. 1. Pulsed coherent X-ray solution scattering (PCXSS)

References
1. T. Kimura, Y. Joti, A. Shibuya, C. Song, S. Kim, K. Tono, M. Yabashi, M. Tamakoshi, T. Moriya, T. Oshima, T. Ishikawa, Y. Bessho, and Y. Nishino, *Nat. Commun.*, **2014**, *5*, 3052.
2. T. Koyama, H. Yumoto, T. Kimura, A. Suzuki, T. Ka-meshima, Y. Joti, K. Tono, N. Tani, T. Tachibana, Y. Konishi, Y. Bessho, Y. Nishino, M. Yabashi, and H. Ohashi, Microsc. Microanal, **2018**, *24(Suppl 2)*, 294–295.
3. A. Suzuki, T. Kimura, Y. Yang, Y. Niida, A. Nishioka, T. Tachibana, M. Takei, K. Tono, M. Yabashi, T. Ishikawa, T. Oshima, Y. Bessho, Y. Joti, and Y. Nishino, Phys. Chem. Chem. Phys., **2019**, Advance Article.
4. J. Wei, K. Niikura, T. Higuchi, T. Kimura, H. Mitomo, H. Jinnai, Y. Joti, Y. Bessho, Y. Nishino, Y. Matsuo, and K. Ijiro, *J. Am. Chem. Soc.*, **2016**, *138*, 3274-3277.
5. R. Yoshida, H. Yamashige, M. Miura, T. Kimura, Y. Joti, Y. Bessho, M. Kuramoto, J. Yu, K. Khakurel, K. Tono, M. Yabashi, T. Ishikawa, and Y. Nishino, *J. Physics B*, **2015**, *48*, 244008.
6. A. Suzuki *et al.*, **2019**, in preparation.

Design of Extremely Low Background Liquid Cell Arrays toward X-Ray Free-Electron Laser-based Single-particle Imaging

Akihiro Suzuki[1], Hirokatsu Yumoto[2,3], Takahisa Koyama[2,3], Yasumasa Joti[2,3], Yoshitaka Bessho[4], Kensuke Tono[2,3], Makina Yabashi[2,3], Tetsuya Ishikawa[3], Yoshinori Nishino[1]

[1]Research Institute for Electronic Science, Hokkaido University, N21W10, Kita-ku, Sapporo, Hokkaido, 001-0021, Japan, [2]Japan Synchrotron Radiation Research Institute/SPring-8, 1-1-1, Kouto, Sayo-cho, Sayo-gun, Hyogo, 679-5198, Japan, [3]RIKEN SPring-8 Center, 1-1-1, Kouto, Sayo-cho, Sayo-gun, Hyogo, 679-5148, Japan, [4]Institute of Biological Chemistry, Academia Sinica, 128, Academia Road Sec. 2, Nankang, Taipei 115, Taiwan

The research aimed at molecular-scale single-particle imaging (SPI) based on the "diffraction before destruction" concept[1] is in progress at X-ray free-electron laser (XFEL) facilities around the world. One of the challenges in the research is the development of a sample delivery system with sufficiently low background scattering[2]. As a step towards designing fundamentally new liquid cell arrays for molecular-level SPI, we measured the background scattering from support frames and partitions, which are the major components of liquid cell arrays.

A liquid cell array typically consists of a support frame, partitions, and membrane windows (Figure 1). To find the optimum frame aperture size, we fabricated rectangular open apertures ranging from 10×10 μm^2 to 200×200 μm^2 in size on a 150-μm-thick silicon substrate by photolithography. Next, to determine the optimum partition aperture size, circular holes having a diameter from 10 to 200 μm were fabricated using a 200-nm-thick silicon nitride membrane as a candidate for partition material. An XFEL experiment was performed at BL2 of SACLA. Figure 2 shows the circular-averaged intensities of diffraction patterns from the rectangular aperture of the 120×120 μm^2 silicon window frame and the 75 μm circular aperture on the silicon nitride membrane. The circular average of the diffraction pattern obtained without any object at the sample position and a simulated solution scattering profile of ribosome 100S[3] are also shown for comparison. Figure 2 shows that the background intensities from the apertures are as low as those without the sample and thus can be neglected. Though the optimum aperture size will depend on slit configuration etc., we found that 75 μm is the minimum threshold diameter for the size of the circular aperture of silicon nitride membranes for the given experimental setup.
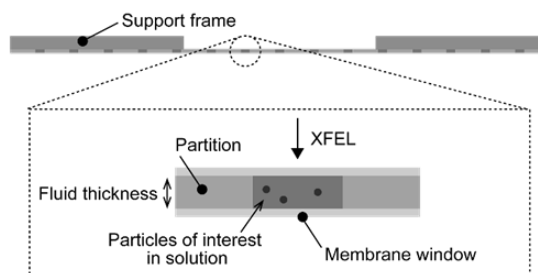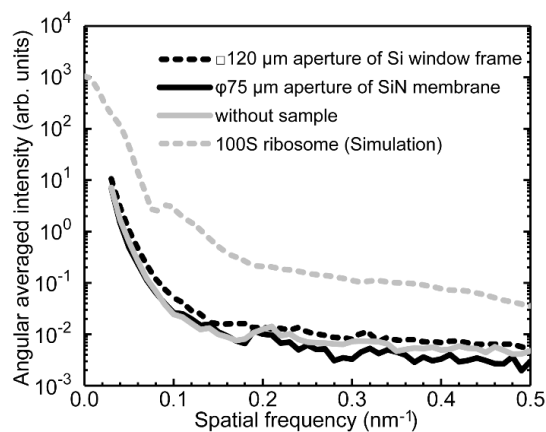

Fig. 1. One design example of a liquid cell for SPI.

Fig. 2. Angular-averaged intensities of diffraction patterns from the apertures.

References

1. Solem & Baldwin, *Science,* **1982**, 218, 229–235.
2. H. N. Chapman, *Annu. Rev. Biochem.*, **2019**, 88, 35–58.
3. T. Kato *et al.*, *Structure*, **2010**, 18, 719–724.

Photon-recycling by Nonradiative Energy Transfer in Piezochemically Synthesized Organic-Inorganic Hybrid Lead Halide Perovskites

Sushant Ghimire,[1] Yuta Takano,[1,2] Vasudevanpillai Biju[1,2]

[1]Graduate School of Environmental Science, Hokkaido University, N10W5, Sapporo, Hokkaido 060-810, and [2]Research Institute for Electronic Science, Hokkaido University, N20, W10, Sapporo, Hokkaido 001-0020, Japan

Perovskites are promising semiconductor materials for efficient and cost-effective solar cells, multicolor LEDs and low threshold lasers. Repeated absorption of emitted photons, also called photon recycling, in large crystals and thick films of perovskites leads to delayed photoluminescence (PL) with decreased PL intensity. The long-range energy transport in large crystals and thick films of lead halide perovskites is facilitated by photon-recycling[1,2] which results in red-shifted and delayed emission from thick perovskite samples. The role of distinct bands, which act as donors and acceptors of energy, and nonradiative energy transfer on such low intensity and delayed emission is yet to be rationalized. In perovskites with close-packed donor-acceptor type states, nonradiative energy transfer should also play an important role on photon-recycling. In this study, we show photon-recycling by nonradiative energy transfer in piezochemically synthesized and close-packed pure and mixed halide methylammonium lead perovskites.[3]
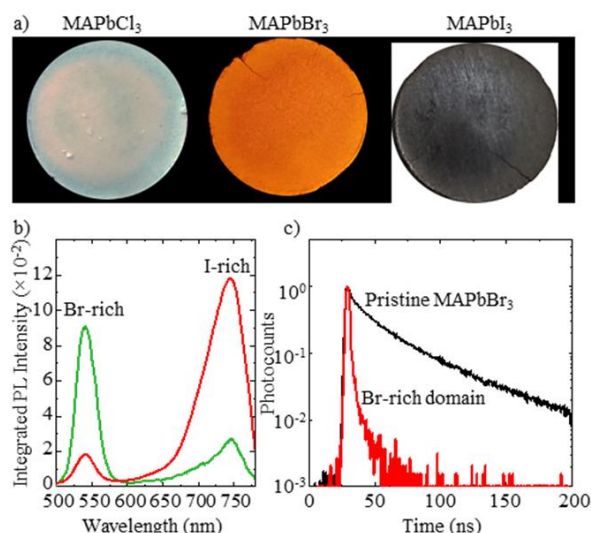
We prepare methylammonium lead halide ($MAPbX_3$; $MA=CH_3NH_3$, X=Cl, Br and I) and mixed halide ($MAPbBr_{3-x}I_x$) perovskites by the piezochemical synthesis, which is by applying a pressure of 2.4 GPa to the thoroughly mixed precursor salts for 30 min (Figure 1a). Here, the piezochemical synthesis helps us to not only synthesize the perovskites but also close-pack the perovskite crystallites into thick pellets, which is essential for nonradiative energy transfer through distributed bands.

The PL spectra (Figure 1b) of mixed halide perovskites show a decrease in intensity of green (500-575 nm) emission from Br-rich domain which is associated with an increase in red (650-800 nm) emission from I-rich domain and vice versa, at different positions. Besides, the PL lifetime (Figure 1c) of a green emitting (500-575 nm) Br-rich domain is much shorter (ca 1.77 ± 0.33 ns) than that of a pristine $MAPbBr_3$ pellet (ca 15.56 ± 3.89 ns). These results suggest that the excited state of Br-rich domain is deactivated by the I-rich domain and thus lowers the PL lifetime, highlighting the role of nonradiative energy transfer from the donor (Br-rich) to the acceptor (I-rich) on photon-recycling.

Fig. 1. (a) Photographs of piezochemically synthesized $MAPbX_3$ (X=Cl, Br, I) perovskites. (b) PL spectra of a mixed halide ($MAPbBr_{3-x}I_x$) perovskite pellet collected from Br-rich and I-rich domains. (c) PL decay profiles of pristine $MAPbBr_3$ and Br-rich (500-575 nm) domains.

In conclusion, by the piezochemical synthesis and close-packing of lead halide perovskites, we find out that nonradiative energy transfer through distributed bands play a central role on photon recycling.[3]

References

1. Y. Yamada, T. Yamada, L. Q. Phuong, N. Maruyama, H. Nishimura, A. Wakamiya, Y. Murata, and Y. Kanemitsu, *J. Am. Chem. Soc.*, **2018**, *137*, 10456-10459
2. Z. Gan, X. Wen, W. Chen, C. Zhou, S. Yang, G. Cao, K. P. Ghiggino, H. Zhang, and B. Jia, *Adv. Energy Mater.*, **2019**, *9*, 1900185.
3. S. Ghimire, K. Takahashi, Y. Takano, T. Nakamura, and V. Biju, *J. Phys. Chem* C, **2019**, DOI: 10.1021/acs.jpcc.9b07003.

Acridinium-based Electron Donor- Acceptor Dyads for Efficient Photothermal Energy Conversion P18

Devika Sasikumar,[1] Yuta Takano,[1,2] Vasudevanpillai Biju[1,2]

[1]*Graduate School of Environmental Science, Hokkaido University, N10W5, Sapporo, Hokkaido 060-810, and* [2]*Research Institute for Electronic Science, Hokkaido University, N20, W10, Sapporo, Hokkaido 001-0020, Japan*

The conversion of solar energy to thermal, chemical, or electrical energy attracts great attention in our daily life.[1] There has been considerable effort for the efficient extraction of photons throughout the entire solar spectrum. In this study, we efficiently harvest light energy using a long-lived photogenerated betaine formed from an acridinium-based electron donor-acceptor dyad. The photothermal energy conversion efficiency of the dyad is significantly enhanced by the simultaneous illumination of blue (420-440 nm) and yellow (480-700 nm) light, which is when compared with the sum of the independent blue and yellow light illuminations. The enhanced photothermal effect is due to the photogenerated betaine that absorbs longer wavelength light than the dyad, which makes the dyad-betaine combination promising for efficient photothermal energy conversion.

The structures of a novel, 9-substituted acridinium ion-based photothermal generator, **1** and a model compound **2** are given in Fig.1. It also shows the pH-dependent absorption spectra of **1**. This molecule undergoes a reversible formation of betaine structure at alkaline pH. The betaine structure shows a new absorption peak around 530 nm, which is attributed to the charge transfer absorption band. Figures 1c and 1e shows the PTEs observed for **1** and **2** at pH 7.4 and under the blue light (420-440 nm, 140 mW cm^{-2}), the yellow light (>480 nm, 440 mW cm^{-2}), or the simultaneous excitation by the two (dual photoexcitation). During the long period of illumination up to 10 min, **1** and **2** show significant increase in the temperature by the blue light illumination and the dual photoexcitation. **1** shows an increase in the temperature up to 11.0 °C at 10 min by the dual photoexcitation, indicating a
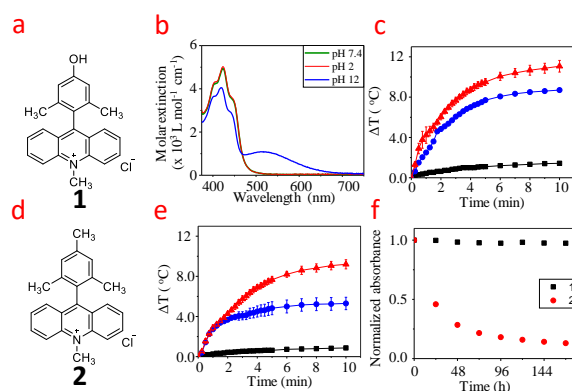

Fig. 1. a, d) The structures of **1** and **2**, b) absorption spectra of **1**. c,e) The photothermal responses induced by **1** and **2** respectively by yellow light (black trace), blue light (blue trace) and dual photoexcitation (red trace) at pH 7.4. f) The photostability study of **1** and **2** at pH 7.4

high PTE from **1**. The PTE observed by blue light illumination of **1** is further enhanced by yellow light irradiation. **1** shows prolonged photostability (Fig. 1f). However, the model compound **2** does not exhibit enhanced PTE under the dual photoexcitation and it suffers from photodegradation on a faster time scale (Fig. 1f). The enhanced PTE by **1** can be explained based on photoinduced betaine generation. At pH 7.4, **1** is in the protonated form in the ground state. By 430 nm illumination, the intramolecular electron transfer in **1** followed by deprotonation and fast intramolecular back electron transfer occurs. Since **1**$_{betaine}$ has the optical absorption in the 480-700 nm region, further excitation of the photogenerated **1**$_{betaine}$ by the yellow light is possible, and it leads to the enhanced PTE. Betaine-type molecules prefer nonradiative relaxation pathway to liberate the excitation energy, which leads to high efficiency PTE. The enhanced PTE by dual photoexcitation and excellent photostability make **1** an efficient candidate for photothermal energy conversion.

Reference
1. G. J. Hedley, A. Ruseckas, and I. D. W. Samuel, *Chem. Rev.* **2017**, *117*, 796-837.

The Role of Iodide Vacancy on Blinking of Lead Iodide P19

Perovskite Single Nanocrystals

Lata Chouhan,[1] Vasudevanpillai Biju[1,2]

[1]*Graduate School of Environmental Science, Hokkaido University, N10W5, Sapporo, Hokkaido 060-810, and* [2]*Research Institute for Electronic Science, Hokkaido University, N20, W10, Sapporo, Hokkaido 001-0020, Japan*

Lead halide perovskites emerge into efficient and cost-effective materials for solar cell, which is owing to their high absorption coefficients and excellent charge carrier mobilities. But perovskites are less stable in the ambient environment. For example, oxygen and moisture affect their chemical structure and optical properties, where the adverse effect of oxygen is through the generation of superoxide[1] which fills the halide vacancies, deprotonates methylammonium cation, and leads to the degradation of perovskite. Therefore, halide vacancy is of an important concern in the field of perovskite. In this work, we fill the iodide vacancies in methylammonium lead iodide ($MAPbI_3$) perovskite nanocrystal (PNC) by adding methylammonium iodide (MAI) to PNCs at the ensemble solution and single particle levels. We find that, by supplementing PNCs with iodide, their PL intensity enhances, and the degradation rate slows down.
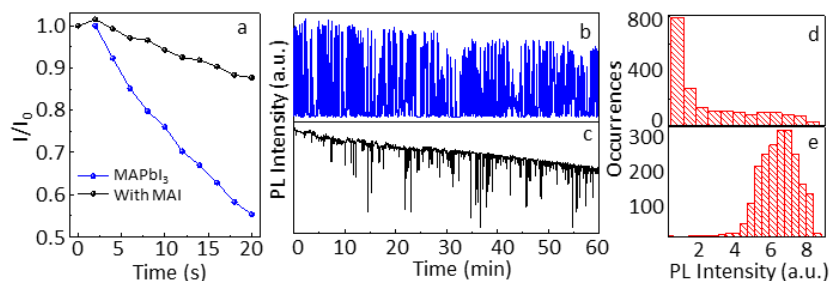
Fig. 1. (a) Relative PL intensities at 750 nm of $MAPbI_3$ PNC solutions with and without the addition of MAI, both under photoirradiation, (b, c) single particle PL intensity trajectories of $MAPbI_3$ PNCs (b) before and (c) after the treatment with MAI, and (d) and (e) the corresponding PL intensity histograms.

To understand the photostability of $MAPbI_3$, we irradiate a $MAPbI_3$ PNC solution with 532 nm laser (50 mW). Fig. 1a shows the relative PL intensities after the photoirradiation, where the PL intensity of a $MAPbI_3$ PNC solution is decreased by 45% and after the treatment with MAI, the PL intensity decreases only to a lesser extent (10%). This implies that the enrichment of $MAPbI_3$ PNCs with iodide fills up the halide vacancies, which enhances the PL and slows down the degradation. To further investigate the role of iodide vacancies on the PL of $MAPbI_3$ PNC, we examine the single particle PL intensity trajectories before (Fig. 1b) and after (Fig. 1c) the treatment of PNCs with a solution of MAI, and the corresponding occurrences of the PL intensity are shown in Fig. 1d and e. Before the treatment with MAI, $MAPbI_3$ PNC shows intense blinking with more OFF events and photodegradation, whereas after the treatment, the blinking is suppressed with more ON events, but photodegradation persists. We have shown that, under the OFF duration, the ionized perovskite is unable to generate superoxide.[1] Thus, photodegradation is suppressed, whereas under the ON duration, the degradation of PNCs continuous due to the continuous generation of superoxide. In this research, the suppression of blinking and decrease in nonradiative relaxation pathways of photoexcited $MAPbI_3$ PNC, which are after the treatment with MAI, show the filling of iodide vacancies.

In conclusion, the PL of PNCs examined at the ensemble and single particle levels shows that $MAPbI_3$ degrades and shows intense blinking. Whereas, after the treatment of PNCs with MAI, the rate of PNC degradation is decreased, and the blinking is suppressed. The MAI treatment fills iodide vacancies in $MAPbI_3$ and improves its photostability.

Reference
1. L. Chouhan, S. Ghimire, V. Biju, *Angew. Chem. Int. Ed.*, **2019,** *58*, 4875 –4879.

Bandgap Modification at Specific Sites of Lead Halide Perovskite   P20

by Local Halide Exchange Reaction under Laser Trapping

Md Shahjahan,[1] Md Jahidul Islam,[1] Ken-ichi Yuyama,[1,2] Vasudevanpillai Biju[1,2]

[1]Graduate School of Environmental Science, Hokkaido University, N10W5, Sapporo, Hokkaido 060-810, and [2]Research Institute for Electronic Science, Hokkaido University, N20, W10, Sapporo, Hokkaido 001-0020, Japan

Organic-inorganic lead halide perovskites attract extensive attention as a new class of semiconductor materials due to excellent optical and electronic properties in addition to low-temperature solution processability. Optical and electronic properties of perovskite crystals can be modified by tuning their bandgaps[1,2]. Halide exchange reaction is a post-synthesis approach for the bandgap tuning. In general, the exchange reaction is induced by exposing a perovskite crystal to the solution containing reactant halide ions, and the bandgap is homogeneously varied in the whole crystals. Here, we demonstrate site-specific halide exchange reaction with the use of a focused laser beam.

Methylammonium lead bromide (MAPbBr$_3$, MA = CH$_3$NH$_3^+$) microrods are synthesized on the cover glass of a sample chamber from the precursor solution (1.3 M) of a mixture of methyl ammonium bromide (MABr) and lead bromide (PbBr$_2$) in a solvent mixture composed of *N,N*-dimethylformamide and γ-butyrolactone (1:1, v:v). Subsequently, a solution of methylammonium iodide (MAI, 250 μM) in a mixture of isopropyl alcohol and hexadecane (1:100, v:v) is added into the chamber. For the halide exchange reaction, 1064-nm near-infrared laser beam is focused onto the surface of a MAPbBr$_3$ micro-rod (Figure 1a). Photoluminescence images of the micro-rod before, during and after the exchange reaction are obtained under the wide-field illumination of 405-nm laser.
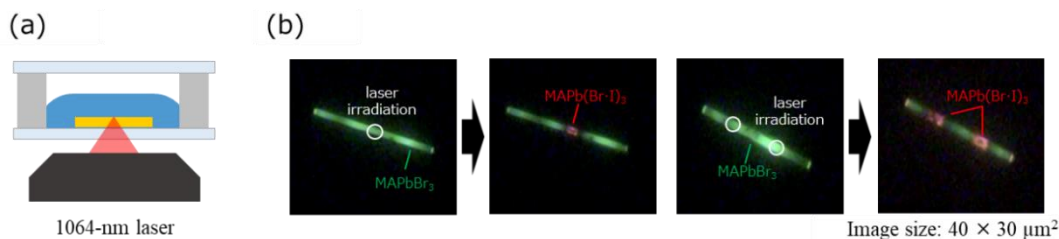
Figure 1 (a) Schematic illustration of the near-infrared laser irradiation into a MAPbBr$_3$ micro-rod. (b,c) Photoluminescence images of MAPbBr$_3$ microrods before and after the laser irradiation

Figure 1b shows photoluminescence images of the microrod before and after the 1064-nm laser irradiation. Before the laser irradiation, the microrod shows green emission throughout, which is due to its intrinsic property [panel (i) of Fig. 1a]. After the laser irradiation at the center of the rod, the green emission is gradually changed into first yellow and finally red [panel (ii) of Fig. 1a]. This is due to local halide exchange reaction of MAPbBr$_3$ with MAI, which leads to the formation of MAPb(Br·I)$_3$ of a lower bandgap. Such a bandgap modification is possible at multiple locations by shifting the laser focus (Fig. 1c). We discuss the possible mechanism of halide exchange from the viewpoint of local concentration increase in MAI under laser trapping.

In conclusion, we successfully demonstrate site-specific band gap tuning of a MAPbBr$_3$ microrod by local halide exchange reaction under the focused laser irradiation. This laser-based approach will offer new methodology for spatially-resolved halide exchange reaction and enable one to control the properties of charge carriers by fabricating heterojunctions in perovskite materials.

References
1. D. M. Jang, K. Park, D. H. Kim, J. Park, F. Shojaei, H. S. Kang, J-P. Ahn, J. W. Lee, and J. K. Song, *Nano Lett.* **2015**, *15*, 5191−5199.
2. Y. Zhang, D. Lu, M. Gao, M. Laia, J. Lin, T. Lei, Z. Lin, L. N. Quan, and P. Yang, *PNAS* **2019**, *116*, 12648-12653.

Photon Recycling through Close-Packed Energy Donor-Acceptor   P21

Interfaces in Perovskite Pellets

Sankaramangalam Balachandran Bhagyalakshmi,[1] Sushant Ghimire,[1] Kiyonari Takahashi,[1,2] Ken-ichi Yuyama,[1,2] Yuta Takano,[1,2] Takayoshi Nakamura,[1,2] Vasudevanpillai Biju[1,2]

[1]*Graduate School of Environmental Science, Hokkaido University, N10, W5, Sapporo, Hokkaido 060-810, and* [2]*Research Institute for Electronic Science, Hokkaido University, N20, W10, Sapporo, Hokkaido 001-0020, Japan*

Perovskites are promising semiconductor materials for efficient and cost-effective solar cells, multicolor LEDs and low threshold lasers. Repeated absorption of emitted photons, also called photon recycling, in large crystals and thick films of perovskites leads to delayed photoluminescence (PL) with decreased PL intensity. The role of distinct bands, which act as donors and acceptors of energy, and nonradiative energy transfer on such low intensity and delayed emission is yet to be rationalized. Here we report delayed emission by nonradiative energy transfer across a distribution of energy states in close-packed crystallites of cesium lead bromide ($CsPbBr_3$), formamidinium lead bromide ($FAPbBr_3$) or mixed halide [$FAPb(BrI)r_3$] perovskite, which are synthesized in the form of thick pellets by the piezochemical method. The PL lifetime of bromide domains in the mixed halide pellet is considerably decreased when compared with that of a pure $FAPbBr_3$ pellet. Here the domains with higher bromide compositions act as the energy donor, whereas the iodide-rich domains are the acceptors. Time-resolved PL measurements of $CsPbBr_3$, $FAPbBr_3$, and $FAPb(BrI)_3$ perovskite pellets with distributed energy states help us to clarify the role of nonradiative energy transfer on photon recycling and delayed emission.[1]

The role of mechanical force on synthesising perovskites is well known. Combined with this fact and the abundance of silicate perovskites in the mantle of the earth, we utilized pressure as the reaction force in the preparation and close-packing of $CsPbBr_3$, $FAPbBr_3$ and $FAPb(BrI)_3$ perovskites. We characterize these perovskite samples by X-ray diffraction (XRD) studies. We characterize the optical properties of these pellets by estimating the bandgaps and recording the PL spectra. The bandgaps are estimated at 2.3 eV for $CsPbBr_3$ and 2.2 eV for $FAPbBr_3$. The PL color is found different at the edge and the center of the pure halide samples. At the edge, the reabsorption of emitted photons is low, and the intensity of green emission is high. On the other hand, away from the edge, the pellets show yellow ($CsPbBr_3$) or orange ($FAPbBr_3$) emission, which suggests efficient photon recycling through closely-spaced energy states in these samples. To examine the existence of crystallites with distributed energy states in pure halide perovskites, we powdered a $FAPbBr_3$ sample and collected the PL from different crystallites. Certain particles show blue-shifted emission (~530 nm), whereas certain other red-shifted (~560nm) maxima. Further, the particles with longer PL lifetime are the ones with the red-shifted PL, while the ones with shorter lifetime show blue-shifted PL. In other words, different PL maxima are accompanied with different PL lifetimes for crystallites isolated from the pellet, and the long PL lifetime associated with the red-shifted emission suggests energy transfer through closely-spaced states in the pellet. To clarify the roles of distinct energy states on energy transfer and photon recycling, we prepared mixed halide $FAPb(Br_3I)_3$ samples. The, we focus PL studies on the bromide-rich (500-575 nm) and iodide-rich (650-800 nm) regions and the bromide/iodide interface. The bromide-rich (500-575 nm) regions in the mixed halide sample show shorter lifetime (2.17 ns) than a pure $FAPbBr_3$ pellet (7.32 ns). This result suggests that the excited state of the bromide-rich part is nonradiatively deactivated by the iodide-rich part. Thus, the role of nonradiative energy transfer on photon recycling is obvious.

Reference

1. S. B. Bhagyalakshmi, S. Ghimire, K. Takahashi, K. Yuyama, Y. Takano, T. Nakamura, V. Biju, *Chem. Eur. J.* **2019**, *25*, in press.

The Control of Bandgap and Exciton Lifetime in Perovskite Crystallites by the Mechanical Deformation

Zhijing Zhang,[1] Sushant Ghimire,[2] Vasudevanpillai Biju,[1,2]

[1]Research Institute for Electronic Science, Hokkaido University, N20, W10, Sapporo, Hokkaido 001-0020, and [2]Graduate School of Environmental Science, Hokkaido University, N10W5, Sapporo, Hokkaido 060-810, Japan

Perovskites show excellent optoelectronic properties such as narrow-band photoluminescence (PL), high carrier mobility, and high structural flexibility. These properties make perovskites promising materials for efficient and cost-effective solar cells, multicolor LEDs and low threshold lasers. The applications of perovskites to such devices can be further expanded by controlling the bandgap, and the dynamics and lifetime of charge carriers or excitons. Herein we show the effect of the mechanical stress on the modulation of PL spectral maxima and lifetime of perovskite microcrystals and nanocrystals, which is due to the structural deformation and change in exciton/carrier confinement. We synthesize formamidinium lead bromide ($FAPbBr_3$) nanocrystals and methylammonium lead bromide ($MAPbBr_3$) microcrystals and investigate the temporally- and spectrally- resolved PL photocounts under the pulsed laser excitation. The nanocrystals are synthesized by a hot injection method wherein the precursor solutions (FABr and $PbBr_2$) are injected into a hot (80 °C) ligand solution (octylammonium bromide and oleic acid dissolved in 1-octadecene).[1] $MAPbBr_3$ microcrystals are prepared by the antisolvent vapor diffusion method wherein the vapor of the antisolvent dichloromethane is diffused into a homogeneous solution of a mixture of MABr and $PbBr_2$ in dimethylformamide.[1]

To examine the role of the mechanical force on the structural deformation and exciton/carrier lifetime of $MAPbBr_3$ microcrystals or $FAPbBr_3$ nanocrystals, we deposited the samples on slide glasses and examined the PL spectra and decay profiles with or without the applied mechanical force. Figure 1 shows the temporally- and spectrally- resolved PL photocounts histograms of $MAPbBr_3$ microcrystals or $FAPbBr_3$ nanocrystals with or without the force. The as prepared microcrystals show the PL maxima ca 560 nm and the PL lifetime ca 12 ns. Interestingly, the PL spectrum is blue-shifted to ca 500 nm upon application of the mechanical stress. The blue-shift was accompanied by decrease of PL lifetime to ca 9 ns. The spectral blue-shift and PL lifetime decrease suggest that the weekly-confined excitons/carriers in the microcrystal become strong upon the mechanically-induced structural deformation. In the case of $FAPbBr_3$ nanocrystals, the PL lifetime is considerably decreased but without much changes to the PL spectral maximum. The decrease of PL lifetime of nanocrystals suggests that the applied mechanical force lowers the dimension of the crystals and strengthens the confinement of excitons/carriers.
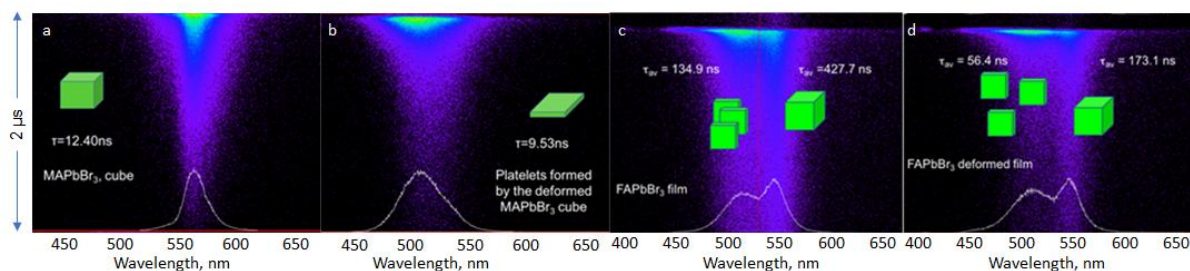
Figure 1. Temporally- and spectrally- resolved photocount histograms of a $MAPbBr_3$ microcrystal and $FAPbBr_3$ nanocrystals (a,c) before and (b,d) after the mechanical deformation. The samples are excited with 400 nm fs pulses (200 KHz).

Reference

1. S. Ghimire, L. Chouhan, Y. Takano, K. Takahashi, T. Nakamura, K.Yuyama, V. Biju, *ACS Energy Letters* **2019,** *4*, 133-141.

# Evaluation of the Coupling between Perovskite Exciton and Gold Plasmon in Films and Cavities

Bhagyashree Mahesha Sachith,[1] Azusa Onishi,[2] Hiroaki Misawa,[2,3]
Vasudevanpillai Biju[1,2]

[1]*Graduate School of Environmental Science, Hokkaido University, N10W5, Sapporo, Hokkaido 060-810, and* [2]*Research Institute for Electronic Science, Hokkaido University, N20, W10, Sapporo, Hokkaido 001-0020, Japan,* [3]*Center for Emergent Functional Matter Science, National Chiao Tung University, Taiwan*

Lead halide perovskite nanocrystals (NCs) attract much attention to the fabrication of devices such as LEDs and solar cells, which is owing to their excellent excitonic and charge carrier properties. Also, owing to their high photoluminescence (PL) quantum yield, narrow and wavelength tunable emission band perovskite NCs become the promising materials for advanced display technology. Post-synthetic chemical transformations of perovskites, such as halide exchange reactions, have proven to be simple and versatile approaches to control the chemical composition and to create new materials which are otherwise not readily accessible by other techniques. Here, we synthesize Cesium lead bromide ($CsPbBr_3$) perovskite nanocrystals by the hot injection colloidal method, and subsequently investigate the exciton lifetime as the function of coupling with the surface plasmon and plasmonic cavities of gold nanoparticles.

We synthesize $CsPbBr_3$ NC by simple hot-injection method. The synthesized nanocrystals are characterized using UV-Vis absorption and fluorescence spectrometers. Thin layers of perovskite NCs are deposited on a cover glass or a thin gold film prepared by the conjugation of 40 nm gold nanoparticles on a cover glass, with or without conjugation using the thiol functional group. The effects of gold nanoparticles on the exciton lifetime and band-gap of $CsPbBr_3$ NCs is examined using spectrally- and temporally- resolved PL spectroscopy.

Figure 1 (A) shows the PL spectra of $CsPbBr_3$ NCs deposited on a cover glass or a thin gold film. Also, the corresponding PL decay profiles are shown in Figure 1B. Interestingly, we find that the PL spectral maximum is shifted to the red by 7 nm on the gold film, which is when compared with that on a bare cover glass. Correspondingly the PL lifetime of the NCs is decreased from 14.6 ns on bare cover glass to 5.6 ns on the gold film. These observations suggest that the excitons in perovskite couples with gold plasmon, and the rate of deactivation of the excited state is increased by the coupling or energy transfer with gold.
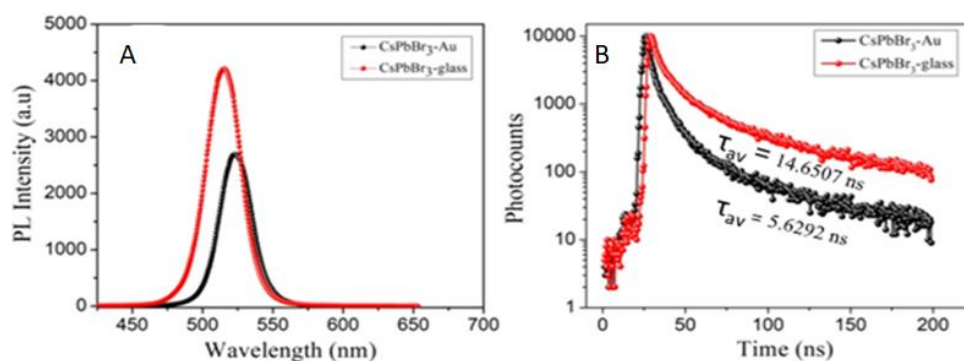
Fig. 1. (A) PL spectra and (B) PL decay profiles of $CsPbBr_3$ NCs on a cover glass or a gold nanoparticle film. The data are collected by exciting the samples with 400 nm fs pulses.
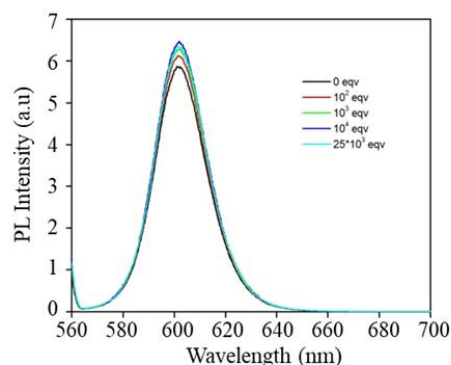
In conclusion, we successfully synthesize $CsPbBr_3$ NCs and demonstrate the change in band-gap and exciton lifetime of $CsPbBr_3$ NCs by gold nanoparticles. Here, the coupling of gold surface plasmon decreases the band-gap of $CsPbBr_3$ and accelerates the relaxation of the photoexcited state.

Quantum Dot-Folic Acid Conjugate for Analyzing Cell-to-Cell Communication *In Vitro*

Sobhanan Jeladhara,[1] Yuta Takano,[1,2] Vasudevanpillai Biju[1,2]

[1]*Graduate School of Environmental Science, Hokkaido University, N10W5, Sapporo, Hokkaido 060-0810,* [2]*Research Institute for Electronic Science, Hokkaido University, N20, W10, Sapporo, Hokkaido 001-0020, Japan*

The size-dependent tunable photoluminescence (PL) color of semiconductor nanocrystals, also called quantum dots (QDs), along with the broad excitation and narrow emission spectra, long fluorescence lifetimes and bright and stable emission make these tiny crystals promising for long-term, multiplexed bioimaging. Also, the large surface to volume ratios and the flexible surface chemistry of QDs are helpful for the conjugation of multiple biomolecules to the QD surface. Among various QDs, group II–VI (CdX, X=S,Se,Te), group IV–VI (PbX; X=S,Se,Te) and group III–V (InP) colloidal QDs are promising for bioanalytical and bioimaging applications *in vitro*. The surfaces CdX QDs are passivated with hydrophobic ligands such as trioctylphosphine and trioctylphosphine oxide, making the as-synthesized QDs incompatible for bioimaging. Although the idea of QDs for biological applications originates from the synthesis of CdX QDs in the aqueous phase, the above hydrophobic-capped QDs are phase-transferred into the aqueous phase by the surface functionalization with molecules such as lipoic acid, thioglycolic acid, amine-based ligands, and polyethylene glycol [1]. However, the ligand exchange reactions of core-only QDs using thiol molecules affect the PL quantum efficiency of QDs. For example, both increase and decrease of PL quantum efficiency are reported for CdS or CdSe QDs. Although an increase in PL quantum efficiency, which is attributed to the passivation of surface defects of QDs, is promising, it is important to consider that the fundamental properties of QDs remain unaffected after the conjugation. Furthermore, the uniform dispersion of QDs in solutions should be maintained after the conjugation.

We conjugate folic acid to QD for cell labeling and imaging and investigating the roles of folic acid and folate receptor on intercellular communication. At first, we examine the effect of thiol conjugation on the PL properties of this QD, which is by recording the PL spectra of a QD solution in the presence of different concentrations of *n*-hexadecane thiol. As shown in Figure 1, the PL intensity of a QD solution is marginally increased with increase in the concentration of the thiol, which is attributed to the surface defect passivation of QD. Nonetheless, we do not rule out the light-induced increase in PL intensity. Importantly, the PL intensity is not decreased in the presence of thiol. However, *n*-hexadecane thiol does not allow for us the

Fig. 1. PL spectra of a QD solution (50 nM) in hexane with different concentrations of *n*-hexadecanethiol.

conjugation of folic acid to QD. Thus, we conjugated dithiolipoic acid to CdSe/CdS/ZnS QD and subsequently 1,11-diamino-3,6,9-trioxaundecane to the carboxylic group. In parallel, we conjugated folic acid to the commercially obtained amino-PEG QD. The QD-folic acid conjugate is folate receptor-specific and helps us with the receptor-selective cell labeling and imaging.

Reference

1. G. Palui, T. Avellini, N. Zhan, F. Pan, D. Gray, I. Alabugin, H. Mattoussi, *J. Am Chem. Soc.* **2012**, *134*, 16370.

The Influence of Bi-Cu Microstructure on the Photoelectrochemical Performance of BiVO$_4$ Photoanode on Water Splitting

Palyam Subramanyam,[1,2] Vasudevanpillai Biju,[2] Ch. Subrahmanyam[1]

[1]*Department of Chemistry, Indian Institute of Technology, Kandi, Hyderabad, India-502285* [2]*Research Institute for Electronic Science, Hokkaido University, N20, W10, Sapporo, Hokkaido 001-0020, Japan*

Recently, photoelectrochemical (PEC) water splitting technology has been receiving much attention for hydrogen production through solar light and counter to greenhouse gas effect. Monoclinic-BiVO$_4$ is one of the most promising photoanodes due to its direct bandgap of 2.4 eV, good photostability and the appropriate band-edge potentials for water oxidation.[1] However, the PEC efficiency is poor because of the fast charge recombination and low carrier mobility in BiVO$_4$. To improve the PEC efficiency, BiVO$_4$ should be modified by the introduction of plasmonic metal nanoparticles. Recently, bimetallic Bi-Cu alloy nanoparticles attract great attention to improve the PEC performance owing to their unique optoelectronic properties. Also, the synergistic effects between the surface plasmon resonance of BiNPs, and the high electrical conductivity and electrocatalytic activity CuNPs supplement the PEC performance.[2] In this work, Bi-Cu/BiVO$_4$ nanocomposite photoanode is fabricated and tested. Impressively, Bi-Cu/BiVO$_4$ photoanode achieves high photocurrent response than pristine BiVO$_4$ photoanode. We conclude that synergistic effects of Bi and Cu help to increase the interfacial charge transfer kinetics in the BiVO$_4$ photoelectrode and improve energy conversion efficiency. Hence, Bi-Cu/BiVO$_4$ provides an opportunity to realize efficient PEC water splitting.
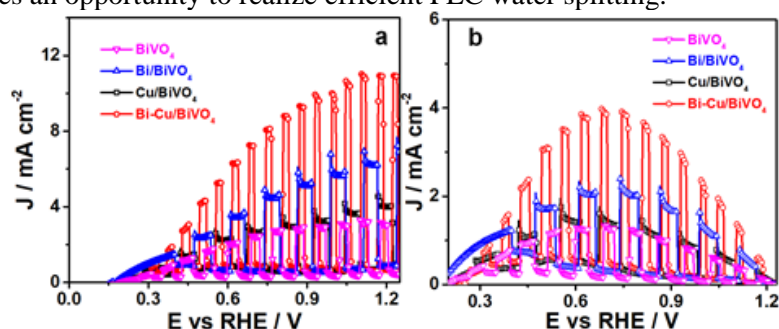

Fig. 1. (a) LSV plots and (b) STH efficiency of fabricated photoanodes.

The BiVO$_4$ photoanode is prepared by the drop-casting. In parallel, BiNPs are synthesized by the chemical reduction method. Subsequently, the BiVO$_4$ photoanode is decorated with BiNPs, which is be the electrophoresis process. Finally, CuNPs are deposited on Bi/BiVO$_4$ photoanode using sonication process.

The PEC activity of as-fabricated photoanodes are evaluated for water splitting by LSV studies (Figure 1a). Upon chopped light illumination, BiVO$_4$, Cu/BiVO$_4$, Bi/BiVO$_4$ and Bi-Cu/BiVO$_4$ composites show photocurrent density of 3.12, 4.95, 6.79 and 10.6 mA/cm^2 at 1.23 V, respectively (Figure 1a). The Bi-Cu/BiVO$_4$ composite shows the highest photocurrent density and exhibits the higher STH efficiency (3.91%) as shown in Figure 1b. These data indicate that Bi-Cu alloy NPs enhance the efficiencies of light harvesting and charge carrier separation of BiVO$_4$.

In summary, we fabricate and characterize Bi-Cu/BiVO$_4$ nanocomposites photoanode and test its PEC performance. Our studies suggest that the reduced exciton recombination and superior PEC performance Bi-Cu/BiVO$_4$ can be promising for high efficiency hydrogen generation.

References
1. E.L. Miller, *Energy Environ. Sci.*, **2015**, *8*, 2809-2810.
2. Q. Wang, J. He, Y. Shi, S. Zhang, T. Niu, H. She, Y. Bi, *Chem. Eng. J.*, **2017**, 326, 411-8.

The Effect of Plasmonic Gold Nanoparticles Embedded in MAPbBr$_3$ PNCs Films

Katta Venkata Seshaiah,[1] Lata Chouhan,[2] Vasudevanpillai Biju,[2,3] Sai Santhosh Kumar Raavi[1]

[1]Department of Physics, Indian Institute of Technology, Kandi, Hyderabad 502285, India, [2]Graduate School of Environmental Science, Hokkaido University, N10W5, Sapporo, Hokkaido 060-810, [3]Research Institute for Electronic Science, Hokkaido University, N20, W10, Sapporo, Hokkaido 001-0020, Japan

Lead halide perovskites are cost-effective materials used for high efficiency solar cell, owing to their high absorption coefficients and excellent charge carrier mobilities. Recent studies on plasmonic gold nanoparticle doped in perovskites show the enhancement in light-harvesting with increase in charge-carrier transport. Here, we investigate the charge carrier dynamics of methylammonium lead bromide (MAPbBr$_3$) perovskite nanocrystals (PNC) film prepared by incorporating the plasmonic gold nanoparticle (Au-NP). We find, the quenching of photoluminescence (PL) and the short lifetime of Au/MAPbBr$_3$ film due to the plasmons results in more non-radiative recombination pathways.
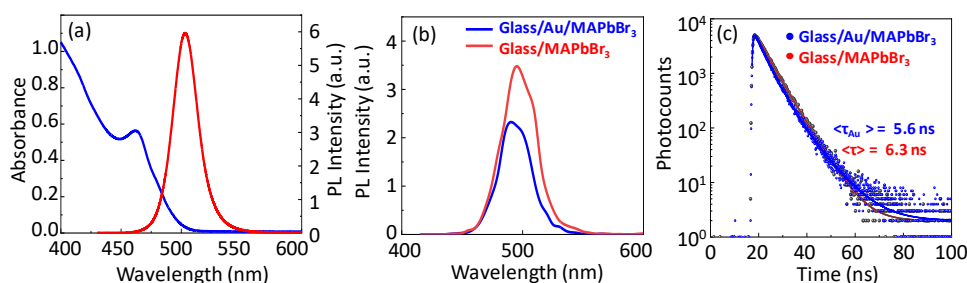
Fig. 1. (a) Absorption (blue trace) and PL spectra (red trace) of MAPbBr$_3$ PNC solution in toluene. (b) PL spectra of MAPbBr$_3$ PNC with (blue trace) and without (red trace) the Au-coating and (c) the corresponding PL decay profiles.

The MAPbBr$_3$ PNCs are prepared by ligand-assisted reprecipitation technique.[1] In this technique, an equimolar ratio of methylammonium hydrobromide and lead bromide are dissolved in dimethyl formamide supplemented with oleic acid and hexadecylamine. In parallel, anhydrous toluene is heated at 60°C into which the above precursor-ligand mixture is quickly injected under vigorous stirring. The reaction is arrested after 15 min of mixing, when the orange-yellow colored precipitation formed which is centrifuged at 10,000 rpm for 5 min. The supernatant obtained after the centrifugation is used for further characterization. The MAPbBr$_3$ PNCs shows broad absorption and narrow PL emission ca. 505 nm as shown in Fig. 1a. For understanding the role of plasmons in MAPbBr$_3$ PNCs, a film of Au/MAPbBr$_3$ is prepared by drop casting 30 µL of Au-NP solution on a glass substrate and annealed at 115°C for 10 min. Subsequently, 30 µL of MAPbBr$_3$ PNCs solution is drop casted on Au-coated substrate and annealed at 90°C for 10 min. As shown in Fig. 1b, the PL of MAPbBr$_3$ PNC quenched after coating on Au-substrate with slight (~6 nm) blue-shift. This is due to the interaction of plasmonic Au-NP and the MAPbBr$_3$ PNCs. To understand the role of charge carrier recombination in this system, the PL decay profiles of MAPbBr$_3$ PNC films with and without Au-coating are recorded (Figure 1c). The PL lifetime of MAPbBr$_3$ PNC film is found to be short (~6.3 ns) which slightly decreased when the PNCs are coated on Au-substrate, indicating the fast charge recombination. As the valence band of Au-NP is above than that of the MAPbBr$_3$ PNCs, the charge accumulates in the metal after the excitation, results in more non-radiative recombination pathways which is responsible for quenching the PL. In conclusion, the direct contact between the plasmonic Au-NP and MAPbBr$_3$ PNCs quenches the charge-carrier properties.

Reference

1. S. Ghimire, L. Chouhan, Y. Takano, K. Takahashi, T. Nakamura, K. Yuyama, V. Biju, *ACS Energy Letters*, **2018**, *4*, 133-141.

Photoresponsive DNA Nanotubes for Nanotechnological

Applications

Ammathnadu S. Amrutha, Nobuyuki Tamaoki*

Laboratory of Smart Molecules, Research Institute for Electronic Science, Hokkaido University, Kita 20, Nishi 10, Kita-ku, Sapporo, Hokkaido 001-0020, Japan

Biological components for instance motor proteins, DNAs, RNAs etc. are often integrated with the non-biological components to generate hybrid bionanodevices. Herein, we demonstrate the construction of a photoresponsive, artificial molecular machine by integrating the photochromic azobenzene molecule and the DNAs. Constructing structures with well-defined nano-scale features has always been an important challenge in nanotechnology. The highly specific pairing of nucleobases facilitates the easy engineering of complex 1D, 2D, and 3D DNA-based nano-structures. Such DNA-based structures are flexible enough to incorporate the non-natural nucleotides.[1] Therefore, we have tried to incorporate a photoresponsive azobenzene-based non-natural nucleotide into the DNA strand and constructed a photoresponsive DNA nanotube. We anticipate that the repetitive *trans* to *cis* and *cis* to *trans* isomerization of the azobenzene unit by light will drive these nanotubes in the solution.

The azobenzene-based non-natural nucleotides (figure 1B) were synthesized according to the earlier reported synthetic procedures.[2] The DNA nanotubes were constructed through single step annealing process (Figure 1A). The formation of DNA nanotubes was confirmed by observing under fluorescence optical microscope (Figure 1C). During the annealing process the DNA strands self-assembled themselves resulting in the crystalline tubular structures. The uniform fluorescence intensity observed throughout the nanotube structure indicated that the dye molecule is uniformly distributed throughout the tubular structure. The successful incorporation of dye molecule into the nanotube structure strongly suggested that similarly, an azobenzene-based DNA monomer has been incorporated in the DNA nanotube.
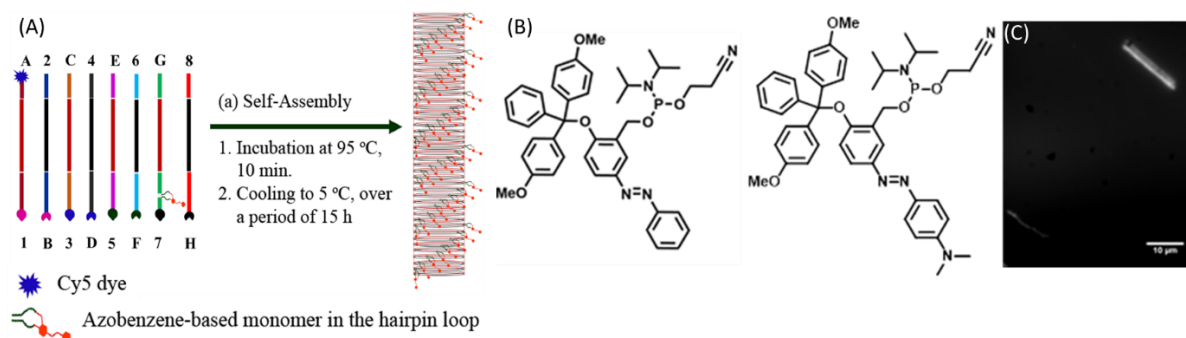
Figure 1. (A) Schematic representation of DNA nanotube formation (B) Azobenzene-based non-natural nucleotides (C) Fluorescence optical microscopy image of azobenzene monomer incorporated DNA nanotube.

A simple method to construct DNA nanotube structures was developed. This method was successfully applied to produce DNA nanotubes with non-natural nucleotides such as Cy5 dye and azobenzene-based DNA monomer. We will further investigate on properties like unidirectional movement and autonomous functioning upon light illumination in near future. The photoresponsive DNA nanotubes are promising in applications where they can be used as cargo delivery vehicles, nanorobots, and bioreactors etc. and offer tremendous opportunities for the development of nanotechnology.

References

1. X. Liang, H. Asanuma, and M. Komiyama, *J. Am. Chem. Soc.* **2002**, *124*, 1877-1883.
2. H. Asanuma, X. Liang, H. Nishioka, D. Matsunaga, M. Liu, and M. Komiyama, *Nat. Protoc.* **2007**, *2*, 203–212.

Development of the Photoswitchable Anti-mitotic Drug P28

Kazuya Matsuo[1], Noushaba Nusrut Mafy[1], Shota Hiruma[2],
Ryota Uehara[2], Nobuyuki Tamaoki[1]

[1]*Research Institute for Electronic Science, Hokkaido University, Kita 20, Nishi 10, Kita-ku, Sapporo, 001-0020, Japan,* [2]*Graduate School of Life Science, Hokkaido University, Kita 21, Nishi 11, Kita-ku, Sapporo, 001-0021, Japan*

The continual unregulated proliferation of cancer cells can be the promising drug target for chemotherapy. For the suppression of the abnormal cell division, many anti-mitotic drugs including microtubules-targeted taxanes or vinca alkaloids have been developed to date. Recently, the new class of anti-mitotic drugs for other proteins than microtubules have been enthusiastically developed. In the dynamic process of mitotic cell division, various biomachines including kinesin and dynein family proteins can concertedly work with high accuracy and precision. However, the malfunction of these biomachines can activate the spindle assembly checkpoint through the misalignment of chromosomes at the metaphase plate. The prolonged mitotic arrest delays the cell-cycle progression, which eventually leads to the apoptotic cell death. Thus, the mitotic biomachines should be the attractive target for anti-mitotic drug.

Herein, we report the novel photoswitchable inhibitor for one of the mitotic kinesin of centromere-associated protein E (CENP-E)[1]. Our photoswitchable CENP-E inhibitor was designed by the introduction of azopyrazole unit into the critical pharmacophore of **GSK923295**[2]. It was successfully demonstrated that the inhibitor enabled to photocontrol CENP-E activity both *in vitro* and in living cells with *ca.* 10-fold change in IC_{50} between *cis-* and *trans*-rich states of the azopyrazole. Using this switching technique of CENP-E functions, the new optochemical system was constructed, where chromosome movement and miscongression on spindle microtubules were photocontrolled in living mitotic cells. The further details and applications will be described in the poster.

References
1. Wood, K. W.; Sakowicz, R.; Goldstein, L. S.; Cleveland, D.W. *Cell* **1997**, *91*, 357-366.
2. Wood, K. W. *et al. Proc. Natl. Acad. Sci. USA* **2010**, *107*, 5839-5844.

A Series of Bisamide-substituted Diacetylenes with a Mechano-Photoresponsive Property for Patterning Applications   P29

Jiajun Qi, Yuna Kim, Nobuyuki Tamaoki

Research Institute for Electronic Science, Hokkaido University
Kita 20, Nishi 10, kita-ku, Sapporo, 001-0020, Japan

Diacetylene (DA) derivatives exhibit solid state polymerization to polydiacetylene (PDA) initiated by UV or γ-ray irradiation and the activation of the photo-induced topochemical polymerization highly relies on the monomer diynes arrangement. To engineer the packing structure of monomeric DA, external stimuli such as heat, light, and mechanical stress can be utilized, but the reports on utilization of mechanical stress are quite rare. Recently, we achieved mechanoresponsive diacetylenes (DAs) exhibiting a crystalline transition of molecular orientation from light-inert to light-active state upon a given pressure (Figure 1).[1] Amide units are introduced to DAs where hydrogen bonding is utilized to control intermolecular interactions. The external pressure (2-150 MPa) resulted in the dramatic crystalline transition from "perfectly off" to "on" state to undergo the light-induced topochemical polymerization of bulk DA crystals. We intended to apply this phenomenon to a new nanoimprinting technique without mechanical deformation of resist materials while phase transition is induced by the mold. In addition, we studied the effect of molecular structure with a series of DA by changing the length of the peripheral alkyl spacers connected to the amide unit systematically.

Fig. 1. Pressure-induced transition of DA from light-inert state to photopolymerable state forming PDA.

Table 1. Polymerization characteristics of DAs upon different condition

	DA-C3	DA-C5	DA-C6	DA-C7	DA-C8	DA-C11	DA-C12	DA-C14	DA-C17	DA-C18
Only UV irradiation	○	○	×	○	×	○	×	×	○	×
Pressure and UV irradiation	○	○	○	○	○	○	○	○	○	○

We observed different photopolymerization phenomena of DA derivatives by changing alkyl spacer lengths (Table 1). In pristine states, DA-C3, 5, 7, 11, 17 could polymerize easily without pressure but only UV irradiation. Meanwhile, DA-C6, 8, 12, 14, 18 showed opposite phenomena that they were inactive upon UV irradiation unless external pressure was given. Photoinduced polymerization behavior of each DA derivative was confirmed by Raman spectra. Raman spectra proved that neither the pristine state nor UV irradiated state shows noticeable trace of PDA formation. Only upon the UV irradiation after external pressure, the DA changed to PDA. DSC and XRD pattern analysis supported the pressure-induced crystalline phase transition of DA derivatives. Results of FT-IR suggested the different intermolecular hydrogen bonding nature of DA crystals.

As a conclusion, we successfully synthesized a series of photo and mechano-responsive DA derivatives. By changing the peripheral alkyl spacers, we could demonstrate that odd/even parity effect: odd numbered DA shows the high light-responsiveness while even numbered DA shows low light-responsiveness in pristine state with ideal pressure-induced crystalline transition enough to be utilized for the imprinting patterning. We could fabricate the pressure-addressed PDA patterns with DA-C8 films which can permit a potential to afford a novel lithography method.

Reference
1. Y. Kim, K. Aoki, M. Fujioka, J. Nishii, N. Tamaoki, *ACS Appl. Mater. Interfaces.* **2018** *10*, 36407-36414.

# Proteorhodopsin Driven by Photoisomerization of Azobenzene   P30

Derivatives

Shariful Haque[1], Takashi Kikukawa[2] and Nobuyuki Tamaoki[1]

[1]*Research Institute for Electronic Science, Hokkaido University, Sapporo, Hokkaido, Japan,* [2]*Faculty of Advanced Life Science, Hokkaido University, Sapporo, Hokkaido, Japan*

We are trying to develop an artificial molecular machine which uses light as a source of energy and continuously executes a particular work such as pumping of proton. Proteorhodopsin (PR), a widely distributed microbial membrane protein is a very efficient molecular machine which acts as light-induced outward proton pump leaded by photoisomerization of retinal[1]. Herein, we report the development and characterization of azo analogues of proteorhodopsin. We designed and synthesized two azo chromophores, 4-[[4′-(*N,N*-dimethylamino)phenyl-1′]azo]benzaldehyde (Az I) and 3-[4-[[4′-(N,N dimethylamino)phenyl-1′]azo]phenyl-1]prop-2-enal (Az II) (**shown in scheme 1**). We characterized the azo analogue of proteorhodopsin, PAz I and PAz II by UV-vis spectroscopy, flash photolysis, pH dependent light-induced proton transfer reaction, light-induced proton pumping function and mutants analysis. We confirmed the formation of PAz I and PAz II from bathochromic shift of UV-vis absorption bands and very slow flash-induced thermal recovery associated with formation of intermediates at shorter and longer wavelengths of azo chromophores. We demonstrated the pH dependent photo-induced proton uptake and release reaction of PAz I and PAz II by reconstitution in phosphatidylcholine (PC) and using indium-tin oxide (ITO) electrode. We successfully expressed the PAz I and PAz II in *E. coli* cells which acquired distinctive yellow and orange pigmentation respectively, indicating interaction of azo chromophore specifically with proteoopsin protein. We described the photo-induced proton pumping function of PAz I and PAz II by expressing in *E*. coli cells and using electrochemical cells made of ITO electrodes. Interestingly, PAz I and PAz II expressing *E. coli* cells suspensions showed the photo-induced potential signal in opposite direction from that of wild proteorhodopsin which indicates their inward proton pumping function. Even, we verified the proton pumping functions of PAz I and PAz II by determining their functional photocyclic reaction pathways. Moreover, we designed three mutants of proteorhodopsin D97N, D227N and E108Q which significantly reduce the proton pumping function of wild PR, and developed the azo analogues of PR mutants. Mutant analogues showed reduction in proton pumping functions which were further proved by their further slower photo reaction cycles, indicating the probable influence of those amino acids on functional properties of PAz I and PAz II. From our findings, we propose a putative model for the inward proton pumping mechanism of our azo analogues of proteorhodopsin. This is the first success of the development of photo-induced proton pumping azo analogues of proteorhodopsin, whose direction of proton pumping is inverted from wild proteorhodopsin.
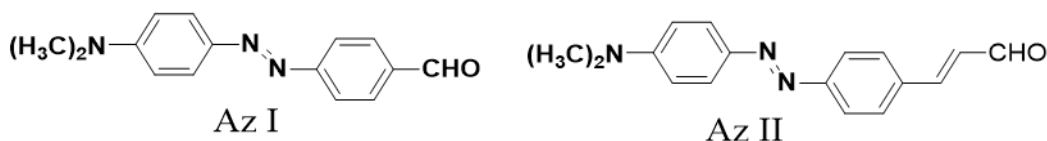
Scheme 1: Molecular structure of azo chromophores Az I and Az II

Reference
1. O. Beja, L. Aravind, E. V. Koonin, M. T. Suzuki, A. Hadd, L. P. Nguyen, S. B. Jovanovich, C. M. Gates, R. A. Feldman, J. L. Spudich, E. N. Spudich, and E. F. DeLong, *Science* **289**, 1902–1906 (2000).

# Tetrazine Derivatives Exhibiting Mesomorphism-dependent Emission Properties

Yuna Kim[1], Clémence Allain[2], Pierre Audebert[2], Nobuyuki Tamaoki[1]

[1]RIES, Hokkaido University, Kita 20, Nishi 10, Kita-ku, Sapporo, Hokkaido, 001-0020, Japan, [2]PPSM , ENS Paris-Saclay, avenue du President Wilson 94230, Cachan, France

Tetrazines are compounds having a deep color ranging from purple to orange to red because of a weak n−π* transition located in the visible region. A large number of tetrazines are fluorescent and are usually utilized for chemosensors[1], fluorescence switching device by interplay of redox chemistry [2] and bio-imaging by inverse electron demand Diels−Alder reaction.[3] Photophysical properties of s-tetrazines in solution state have been widely investigated where each tetrazine is molecularly dispersed. In contrast, little attention has been paid to luminescent tetrazines in the solid and/or liquid-crystalline states.[4] Luminescence tunability in condensed phase are intriguing as they may exhibit unconventional photophysical functions that have never been achieved in solution state.

Herein we report the first examples of tetrazines exhibiting emission color-tunable polymorphism and their attractive features such as solvatochromism, vaporchromism and aggregation-induced emission enhancement. We examined the thermal stimuli-responsive luminescence behaviour of **1**, **2** and **3** in the condensed state. Orange emission color of pristine crystals of tetrazine derivatives ($\lambda_{em,max}$ = 575, 570, 590 nm for **1**, **2** and **3**, respectively) was totally quenched by reaching clearing temperature at around 110 ºC. Upon subsequent cooling process, the thermal stimuli-induced crystalline phase exhibited significant blue shift of the emission band with greenish yellow color for **1** (Fig.1a) and **3**, $\lambda_{em,max}$ of 565 nm and 562 nm, respectively, while **2** showed negligible transition in photoluminescence. In addition, thermally-induced crystalline phase was recovered to original crystalline phase with orange color luminescence by simple solvent exposure such as chloroform or dichloromethane. X-ray diffraction (XRD) patterns clarified the reversible thermal-/vapor-chromic phase transition of the thermodynamically metastable crystalline phases as shown in Fig. 1b.
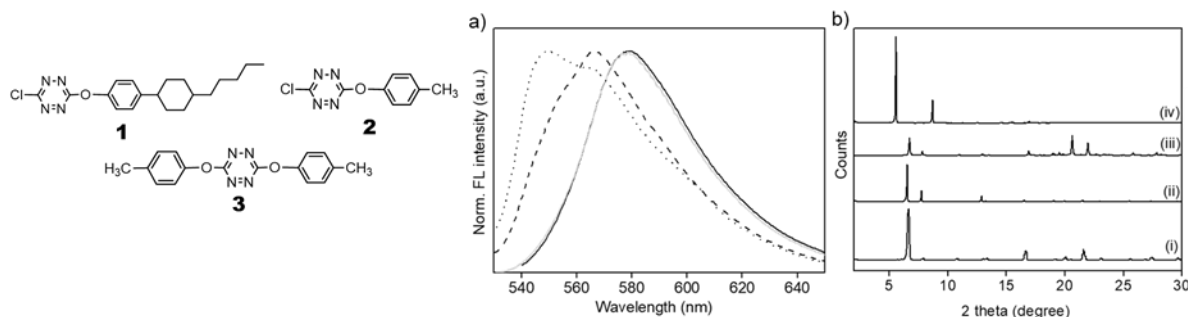
Fig. 1. Molecular structures of tetrazine derivatives from **1** to **3**. (a) Photoluminescence spectra of **1** in pristine crystalline state (orange emission, black solid line), thermally-induced crystalline state (yellow emission, dashed line), dropcasted crystalline state from chloroform solution (greenish yellow emission, dotted line) and single crystal (orange emission, gray solid line). (b) XRD patterns of **1** in the (i) pristine crystalline state, (ii) chloroform-annealed state after iv state (iii) single crystal and (iv) thermally-induced crystalline state.

References
1. G. Clavier, P. Audebert, *Chem. Rev.* **2010**, *110*, 3299.
2. Y. Kim, E. Kim, G. Clavier, P. Audebert, *Chem. Commun*. **2006**, 3612.
3. A. Wieczorek, P. Werther, J. Euchner, R. Wombacher, *Chem. Sci.* **2017**, *8*, 1506.
4. G. Pelzl, H. Zaschke, D. Demus, *Displays*, **1985**, *6*, 141.

Mechanical Simulation for Waveguides for Multi-striped Orthogonal Photon-Photocarrier Propagation Solar Cells

Jiaxing YU, Y. Ohkura[1], N. Sawamura, A. Ishibashi[1]

Nanostructure Physics Laboratory, Research Institute for Electronic Science, Hokkaido University, Sapporo, Hokkaido 001-0021, Japan

So far, many studies have been done in order to improve the efficiency of solar cells, and numerous types of photovoltaic devices have been reported. However, it is still difficult for us to convert the full sunlight spectrum into electricity. In order to solve this problem, our laboratory put out a new solution which may be potential for the development of solar cells industry and greatly improve the efficiency
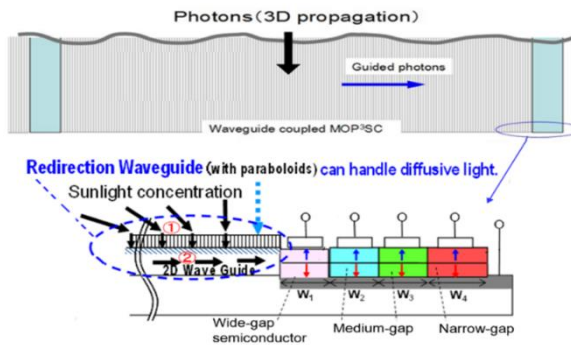
Fig. 1. Waveguide-coupled multi-striped orthogonal photon-photocarrier-propagation solar-cell.

of solar cells. Different from the conventional solar cells in which photons and photocarrier are absorbed parallelly, our new approach is that we make the photon and photocarrier absorbed orthogonally. The conventional solar cells suffer greatly from the light absorption and photo-generated carrier collection, in our propose, the multi-striped orthogonal photon-photocarrier propagation solar cells can absorb more photons, meanwhile, the loss of photocarriers would be less. In our asymmetric waveguide coupled concentrating solar cells, how to make spatially propagating light efficiently convert into wave light

is of vital importance for the research. We found that the space inversion (left and right) in symmetric structure, coupled with time-reversal symmetry, light that has been convert to two-dimensional from three dimensions will go back to three dimensions. In this case, we assume that if we use asymmetric waveguide, the problem will be solved. The waveguide we proposed is asymmetric to achieve better confinement of photons in the waveguide resulting in more photon harvesting. A top view of a prototype of our new concentration solar cell system is shown in Fig.1.

In speaking of redirection waveguide, we are now able to propose a new waveguide. Using the structure showing in the top of Fig.2 for the second layer of the redirection waveguide, we have made simulations, in which thanks to the translational symmetry as well as the first function of the redirection

Fig. 2. The structure of RWG in y-z plane (top) and the simulation result of light-wave propagation (bottom).

waveguide, we can solve the light propagation problem. Simulation of light propagation in new waveguide shown in Fig 2. In order to get the structure as shown in Fig 2, we proposed to use PDMS because of transparency and high material quality, such material is commercially available.
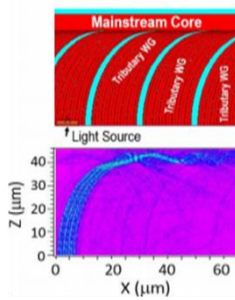
We have shown that good mainstream-to-mainstream and tributary-to-mainstream propagation of photons would be obtained in the redirection waveguide. Also, the light-wave merging can be fulfilled in the waveguide with the discrete translational symmetry. The photons are well conveyed in the new waveguide losslessly for a distance of ~1 mm. The new waveguide with the discrete translational symmetry would serve, in near future, as a key component for excellent concentration photovoltaic systems with high conversion efficiencies.

References
1. A. Ishibashi, N. Kawaguchi, K. Kondo, H. Kaiju, S. White, Proc. 6th Int. Symp. Environmentally Conscious Design and Inverse Manufacturing (Ecodesign2009), 2009, p.55.
2. A. Ishibashi, H. Kobayashi, N. Sawamura, K. Kondo, T. Kasai, IEEE-ICASI, Meen, Prior & Lam (eds.) p. 1477 (2017).

A Study of Topological Hall Effects and Topological Spin Hall Effects Caused by a Skyrmion　　P33

Yuichi Ishida and Kenji Kondo

Laboratory of Nanostructure Physics, Research Institute for Electronic Science,
Hokkaido University, N20, W10, Sapporo, Hokkaido, 001-0020, Japan

Recently, magnetic skyrmions have been paid much attention due to their desirable properties when applying them for spintronics devices such as racetrack memories. One of the above properties is that skyrmions are topological solitons with particle-like nature. Moreover, it is difficult to destroy their structures and deform them to other magnetic structures since their structures are topologically protected. For this reason, one bit of information can be carried by skyrmions. In order to apply skyrmions to the spintronics devices, we need to read information out by detecting the existence of skyrmions. This can be resolved using the topological Hall effect (THE). THE originates from the fact that skyrmions create an emergent magnetic field working on itinerant electrons in ferromagnets. Moreover, the topological spin Hall effect (TSHE) is also caused by the emergent magnetic field. This is because the emergent fields are opposite to each other for itinerant electrons with different spins. In our study, in order to utilize THE and THSE in the spintronics devices, we investigate the above effects for Néel-type skyrmion and Bloch-type skyrmion using the tight binding model, respectively. The Hamiltonian consists of the nearest neighbor hopping and the exchange coupling between spins of itinerant electrons and local magnetizations. Here, we utilize J_H as units of the energy. In the case that the hopping parameter t and the strength of exchange coupling J_H are equal values, figure 1(a) shows density of states (DOS) and figure 2(b) shows topological (spin) Hall angles θ_{THE} (θ_{TSHE}) for different fermi energy ε_f. In both the cases, we consider a Néel-type skyrmion. In addition, it is found that the same results can be also obtained in the case of a Bloch-type skyrmion. As shown in Fig. 1(b), there exists strong dependence of THE and TSHE on the fermi energy of itinerant electrons. Therefore, we consider that the fermi energy is an important factor to apply skyrmions to spintronics devices.
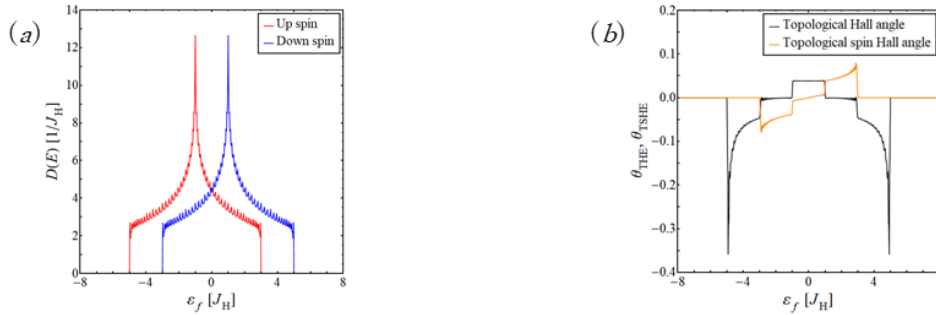

Fig. 1. (a) DOS of a ferromagnetic lead in the case of $t = J_H = 1$. The red and blue lines represent the DOS of the electrons with the up spin and the down spin, respectively. (b) Topological (spin) Hall angles θ_{THE} (θ_{TSHE}) in the case of a Néel-type skyrmion. The black and orange lines represent the Hall angle and the spin Hall angle, respectively.

References

1. Y. Ishida and K. Kondo, *J. Magn. Magn. Mater.* **493**, 165687 (2020).
2. Y. Ishida and K. Kondo, Extended Abstracts of the 2018 International Conference on Solid State Devices and Materials, 1211 (2018).
3. Y. Ishida and K. Kondo, Extended Abstracts of the 2019 International Conference on Solid State Devices and Materials, 945 (2019).
4. N. Nagaosa and Y. Tokura, *Nat. Nanotechnol.* **8**, 899 (2013).
5. A. Fert, V. Cros, and J. Sampaio, *Nat. Nanotechnol.* **8**, 152 (2013).
6. P. B. Ndiaye, C. A. Akosa, and A. Manchon, *Phys. Rev. B,* **95**, 064426 (2017).
7. G. Yin, Y. Liu, Y. Barlas, *et al.*, *Phys. Rev. B,* **92**, 024411 (2015).

Electric Field Thermopower Modulation Analyses of High Mobility Transparent Amorphous SnO₂ Thin Film Transistor

Dou-dou Liang [a,b)], Yu-qiao Zhang [a)], Hai Jun Cho [a)], and Hiromichi Ohta [a)]

[a] *RIES, Hokkaido University, N20W10, Kita, Sapporo 001-0020, Japan*
[b]*University of Science and Technology Beijing, Beijing 100083, China*

Tin dioxide (SnO₂) is an earth-abundant, optically transparent wide-bandgap semiconductor (~3.6 eV), which has been widely used for gas sensing and transparent electrodes. Shin *et al*.[1] showed that a thin (<4.5 nm) SnO₂ film transistor (TFT) exhibited a high field effect mobility of 150 cm² V⁻¹ s⁻¹ at 300K, but a thicker SnO₂ TFT channel did not show off states. It is likely that the oxygen adsorbed on the surface of SnO₂ reduced the Fermi energy and the effective channel thickness, but this mechanism has not been clarified. To clarify the operation mechanism of thin SnO₂-based TFT, we fabricated a bottom-gate-top-contact TFT and examined the thermopower (S), sheet carrier concentration (n_s), and volume carrier concentration (n_{3D}) to extract the effective channel thickness. [2-5]

The SnO₂ TFT (4.2 nm) was tested in air and vacuum. The on-to-off current ratios were >10⁴, the threshold voltage (V_{th}) was −14.7 V in air, and it shifted to −25.25 V in vacuum (**Fig. 1a**). The field effect mobilities (μ_{FE}) were ~20 cm² V⁻¹ s⁻¹ in air and ~30 cm² V⁻¹ s⁻¹ in vacuum (C_i ~58 nF cm⁻²). The -S values as a function of n_s in a logarithmic scale were linear relationships were observed, but the slopes were different in air (~120 μV K⁻¹/decade) and vacuum (~84 μV K⁻¹/decade) (**Fig. 1b**). These are comparable to other reports [6-9] and confirm that the conduction band is parabolic. The deviation observed around ($|S|$, n_s) = (147 μV K⁻¹, 2.5 × 10¹² cm⁻²) in air is attributed to the tail states around the conduction band minimum due to structural defects in the amorphous SnO₂ thin film. With increasing electric field, (S, n_s) was modulated from (–150 μV K⁻¹, 2 × 10¹² cm⁻²) to (–80 μV K⁻¹, 1 × 10¹³ cm⁻²) in air and from (–110 μV K⁻¹, 2.9 × 10¹² cm⁻²) to (–60 μV K⁻¹, 1.3 × 10¹³ cm⁻²) in vacuum, respectively. The effective thickness (n_s/n_{3D}) was always around 1.2 nm both in air and vacuum (**Fig. 2c**). The discrepancy between air and vacuum is attributed to the gas sensor property of SnO₂, which will release the adsorbed O₂ in vacuum.
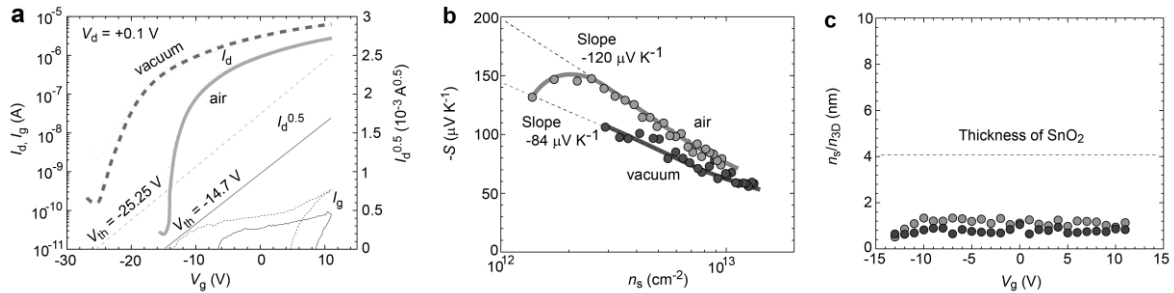
Fig. 1. Electric field dependent thermopower analyses of a SnO₂ TFT in air and vacuum. (a) Transfer characteristics (I_d−V_g) at V_d = +0.1 V. (b) −S as a function of n_s. The slopes in air and vacuum were different (dotted line). (c) The effective channel thickness is < 1.2 nm in air and vacuum at all V_g.

In summary, we demonstrated the operation mechanism of a transparent amorphous SnO₂ channel TFT. The effective channel thickness was clarified (~1.2 nm). A tail state was detected from the S modulation, and the gas sensor characteristic of SnO₂ was found. The present results clarify the operation mechanism of SnO₂-based TFTs and their gas sensing characteristics.

References

[1] C.W. Shih *et al*., *Sci. Rep.* **6**, 19023 (2016). [2] H. Ohta *et al.*, *Appl. Phys. Lett.* **95**, 113505 (2009); *Nat. Commun.* **1**, 118 (2010); *Adv. Mater.* **24**, 740 (2012); *Adv. Sci.* **4**, 1700696 (2017). [3] H. Koide *et al.*, *Appl. Phys. Lett.* **97**, 182105 (2010). [4] A. V. Sanchela *et al.*, *Phys. Rev. Materials* **1**, 034603 (2017). [5] A. V. Sanchela *et al.*, *Small* **15**, 1805394 (2019). [6] A. Papadogianni *et al.*, *Appl. Phys. Lett.* **107**, 252105 (2015). [7] T. T. X. Vo *et al.*, *Phys. Stat. Sol. A* **212**, 2776 (2015). [8] M.N. Islam *et al.*, *J. Phys. D, Appl. Phys.* **18**, 71 (1985). [9] D. F. Morgan and D. A. Wright, *Brit. J. Appl. Phys.* **17**, 337 (1966).

Systematic Investigation of Thermoelectric Properties in Sr$_{1-x}$La$_x$TiO$_3$ Solid-solutions

Kenyu Sugo[1,*], Yu-qiao Zhang[2], Hai Jun Cho[1,2] and Hiromichi Ohta[1,2]

^{1}IST-Hokkaido Univ., N14W9, Kita, Sapporo, 060-0814, Japan
^{2}RIES-Hokkaido Univ., N20W10, Kita, Sapporo, 001-0020, Japan

The performance of thermoelectric materials is estimated by $ZT = S^2 \cdot \sigma \cdot T \cdot \kappa^{-1}$, where ZT is figure of merit, T is absolute temperature, S is thermopower, σ is electrical conductivity, and κ is thermal conductivity. Currently, practical thermoelectric materials are based on expensive heavy-metal elements (i.e. Bi_2Te_3) that have low thermal and chemical stability. Therefore, as an alternative, we focus on $SrTiO_3$ which exhibits high power factors ($\equiv S^2 \cdot \sigma$).[1,2] Recently, our systematic investigation of $SrTi_{1-x}Nb_xO_3$ solid-solutions revealed that that their de-Broglie wavelengths the $SrTi_{1-x}Nb_xO_3$ solid-solutions can be controlled with Nb-substitutions.[3] These were utilized in an artificial $SrTi_{1-x}Nb_xO_3$ superlattice with a long de-Broglie wavelength, which doubled the power factor compared to the bulk.[4] This shows that the importance of systematically studying oxide solid-solutions. Here, we focus on thermoelectric and structural properties of epitaxial $Sr_{1-x}La_xTiO_3$ thin film solid-solutions fabricated on (001) $LaAlO_3$ substrates.

The electron transport properties are summarized in **Fig. 1**. The carrier concentration (n) almost follows the nominal tendency, while the Hall mobility (μ_{Hall}) shows an overall decreasing tendency with x except for a small jump at $x \sim 0.5$. The overall behavior of μ_{Hall} was similar to the Debye relaxation time, indicating an electronic phase boundary induced by the crystal structure evolution. The absolute thermopower ($|S|$) decreases monotonically with x until it slightly increased at $x = 0.7$. The effective mass (m^*) firstly decreases with x until it increases $x \sim 0.7$, which is attributed to a Mott-insulator transition. Two thermoelectric phase boundaries were observed in the system ($x \sim 0.5$ and $x \sim 0.7$).[5]

In this study, $Sr_{1-x}La_xTiO_3$ ($0.01 \leq x \leq 1$) epitaxial films were fabricated and their thermoelectric
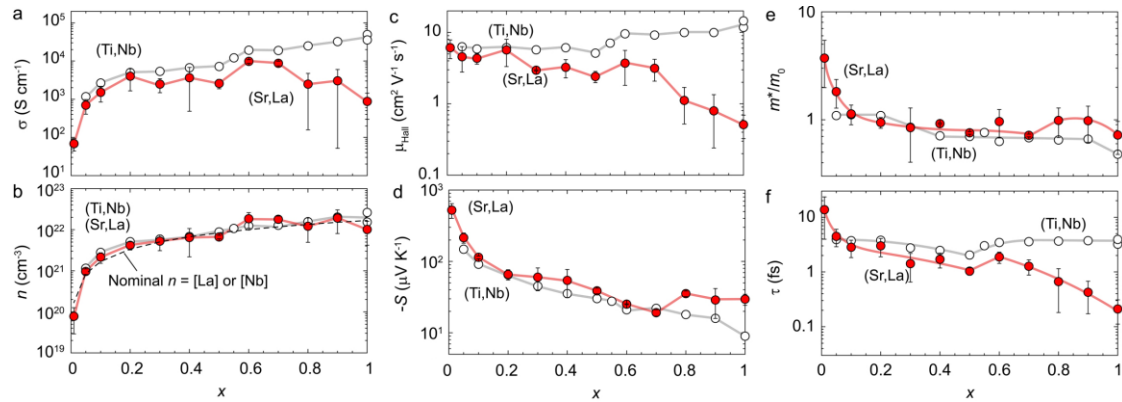
Fig. 1. Room temperature electron transport properties of $Sr_{1-x}La_xTiO_3$ epitaxial films: (a) electrical conductivity (σ), (b) carrier concentration (n), (c) Hall mobility (μ_{Hall}), (d) thermopower (S), (e) effective mass (m^*), (f) relaxation time (τ).

properties were investigated. As a result, we revealed two thermoelectric boundaries ($x \sim 0.5$ and $x \sim 0.7$). The former is attributed to the lattice distortion from cubic to orthorhombic variation, whereas the latter is due to the electronic phase transition from band insulator $SrTiO_3$ to Mott insulator $LaTiO_3$, respectively. The revealed thermoelectric properties in this study will be useful for designing $SrTiO_3$-based thermoelectric conversion materials in the future.

References
[1] H. Ohta, Mater Today **10**, 44 (2007). [2] H. Ohta *et al.*, *Inorg. Chem.* **47**, 8429 (2008). [3] Y. Zhang *et al.*, *J. Appl. Phys.* **121**, 185102 (2017). [4] Y. Zhang *et al.*, *Nature Commun.* **9**, 2224 (2018). [5] Y. Zhang, **K. Sugo** *et al.*, *J. Appl. Phys.* **126**, 075104 (2019).

Fabrication and Thermopower Modulation of Thin Film Transistor using Deep-Ultraviolet Transparent Oxide Semiconductor as Active Layer

Gong Lizhikun[1,*], Dou-dou Liang[1,2], Mian Wei[1], Hai Jun Cho[1,3], Hiromichi Ohta[1,3]

[1]Graduate School of Information Science and Technology, Hokkaido University, Sapporo, Japan, [2]University of Science and Technology Beijing, Beijing 100083, China
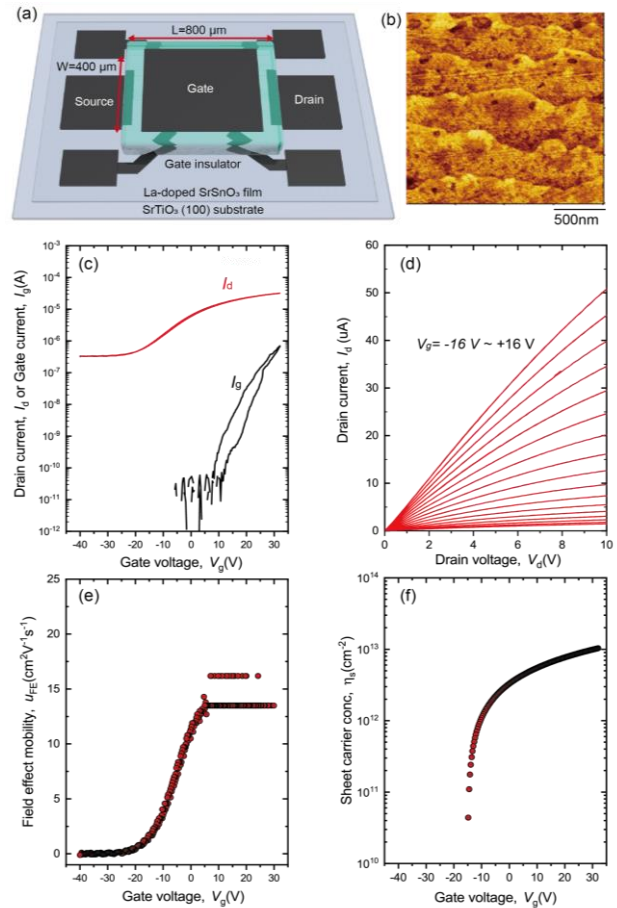[3]Research Institute for Electronic Science, Hokkaido University, Sapporo, Japan

Thin-film transistors (TFTs) with high carrier mobility and deep ultraviolet transparency (<300 nm in wavelength) are crucial for next generation optoelectronics. In this regard, $SrSnO_3$ is one of the most promising materials due to its large bandgap (~4.6 eV [1,2]), and its epitaxial film showed high electrical conductivity (σ = 3000 S cm^{-1}) with high electron mobility (μ_{Hall} ~56 cm^2 V^{-1} s^{-1}) at a carrier concentration of 3.26×10^{20} cm^{-3} [3,4]. A depletion-mode $SrSnO_3$ n-channel MESFET was reported recently.[5] Here we demonstrate a different type of TFT with $SrSnO_3$ channel in metal–insulator–semiconductor (MIS) configuration.

We fabricated La-doped $SrSnO_3$ films on (001)-oriented $SrTiO_3$ substrate by pulsed laser deposition, then fabricated the TFT structure on the $SrSnO_3$ films using 300 nm thick amorphous C12A7 (gate insulator) and metallic Ti (electrodes) (**Fig. 1a**). The resultant TFT showed clear transistor characteristics (**Figs. 1c and d**); the on-to-off ratio was ~10^2, the threshold voltage was ~−15 V, the output characteristic curves showed pinch-off behavior and the field effect mobility was ~16 cm^2 V^{-1} s^{-1} (**Fig. 1e**). The electric field effect thermopower (S) modulation of the TFT showed that the conduction band minimum is parabolic in the reciprocal space.

In summary, we demonstrated a functional $SrSnO_3$-TFT with metal-insulator-semiconductor (MIS) configuration for the first time. The field effect mobility of ~16 cm^2 V^{-1} s^{-1} was observed at the gate voltage of +7 V. The on/off ratio was ~10^3. the threshold voltage was ~−15 V and the output characteristic curves showed pinch-off behavior.

Fig. 1. Resultant $SrSnO_3$ TFT at room temperature [(a) schematic TFT structure, (b) topographic AFM image of the $SrSnO_3$ film surface, (c) transfer characteristics, I_d–V_g at V_d = +3.5 V, (d) output characteristics, I_d–V_d, (e) field effect mobility, μ_{FE}, and (f) sheet carrier concentration, n_s.

References

[1] H. Mizoguchi *et al*,. *Inorg. Chem.* **43**, 1667 (2004). [2] D. J. Singh *et al*., *Appl. Phys. Lett.* **104**, 011910 (2014). [3] L.R. Wang *et al*., *Phy. Rev. Materials* **1**, 061601(R) (2017). [4] M. Wei *et al*., submitted in *Appl. Phys. Lett.* [5] V.R.S.K. Chagnti *et al*., *IEEE Electron Device Lett.* **39**, 1381 (2018). [6] J. Shiogai *et al*., *AIP Adv.* **6**, 065305 (2016).

Epitaxial Film Growth of a Deep-Ultraviolet Transparent Oxide Semiconductor, La-Doped SrSnO₃   P37

Mian Wei[1,*], Anup V. Sanchela[2], Bin Feng[3], Yuichi Ikuhara[3], Hai Jun Cho[1,2], Hiromichi Ohta[1,2]

[1]*Information Science and Technology, Hokkaido University, Sapporo 060−0814, Japan*
[2]*Research Institute for Electronic Science, Hokkaido University, Sapporo 001−0020, Japan*
[3]*Institute of Engineering Innovation, The University of Tokyo, Tokyo 113−8656, Japan*

La-doped SrSnO₃ (LSSO) is known as one of deep-ultraviolet (DUV)-transparent conducting oxides with an energy bandgap of 4.2 eV. However, due to difficulties in growing high-quality LSSO films, their electron transport properties have not been extensively studied compared to the optical properties and electronic structures. The reported electrical conductivities of LSSO films are below 1000 S cm⁻¹, which is much lower than that of commercially available transparent conducting oxide ITO (~7000 S cm⁻¹), most likely due to the low activation of La ion in LSSO.[1,2]
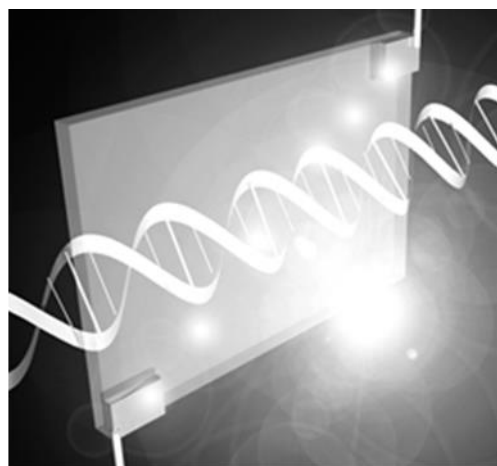
La$_x$Sr$_{1-x}$SnO₃ ($x = 0.005−0.05$) epitaxial films were fabricated on (001) MgO substrates using pulsed laser deposition. The crystalline orientation, lattice parameters, and thickness of the films were analyzed by high resolution X-ray diffraction. Scanning transmission electron microscopy (STEM) was used to observe the microstructures of the films. The electrical transport properties were measured using the conventional dc four-probe method. The thermopower (S) was acquired from the thermos-electromotive force (ΔV) generated by a temperature difference (ΔT). The LSSO films were annealed in vacuum to enhance their electrical properties.

Fig. Schematic illustration of highly conducting (>3000 S cm⁻¹) deep ultraviolet (<300 nm) transparent oxide semiconductor, La-doped SrSnO₃ epitaxial film. The DNA is illuminated the DUV light through the DUV-TOS.

The highest electrical transport properties of as-deposited LSSO films were 1773.7 S cm⁻¹ and 47.7 cm² V⁻¹ s⁻¹ observed from 3% LSSO film. However, after vacuum annealing, great enhancements in the activation rate of La ion and electrical transport properties were observed. The carrier concentration and Hall mobility were improved from 2.32×10^{20} cm⁻³ and 47.7 cm² V⁻¹ s⁻¹ to 3.26×10^{20} cm⁻³ and 55.8 cm² V⁻¹ s⁻¹, respectively. STEM showed that this phenomenon is attributed to the lateral grain growth occurred during the annealing. The carrier effective mass (m^*) of LSSO epitaxial film was also clarified by the thermopower measurements, which turned out to be 0.23 m_0, similar with that of Ba₀.₅Sr₀.₅SnO₃.[3]

In summary, we developed epitaxial La-doped SrSnO₃ thin film showing an excellent conductivity value of 3000 S cm⁻¹. The optical transmission at 260 nm in wavelength was >25 %, clearly demonstrating that the LSSO films are applicable as transparent electrodes for DUV optoelectronic devices such as DUV light emitting diode and DUV detector for biological applications.[4]

References

1. D. Ginley *et al.,* in *Handbook of Transparent Conductors* (Springer, 2011).
2. E. Baba *et al., J. Phys. D. Appl. Phys.* **48**, 455106 (2015).
3. A. V. Sanchela, *et al., Small* **15**, 1805394 (2019).
4. M. Wei *et al.*, submitted to *Appl. Phys. Lett.*

Macroscopic Visualization of Fast Electrochemical Reaction of SrCoO$_x$ Oxygen Sponge

Qian Yang[1], Hai Jun Cho[1,2], Hyoungjeen Jeen[3], Hiromichi Ohta[1,2]

1 Graduate School of Information Science and Technology, Hokkaido University, Japan
2 Research Institute for Electronic Science, Hokkaido University, Japan
3 Department of Physics, Pusan National University, Busan, Korea

Strontium cobaltite (SrCoO$_x$) shows fast topotactic electrochemical redox reactions [1−3] and therefore referred to as 'oxygen sponge'.[4] Although of the oxidation of SrCoO$_{2.5}$ into SrCoO$_3$ is known in atomic scale, it has not been clarified in macroscopic scale yet. Here, we macroscopically visualize the electrochemical oxidation of SrCoO$_x$.[5] SrCoO$_x$ epitaxial films with various oxidation states were prepared. This process was directly visualized using conductive AFM.

The films were heteroepitaxially grown on (001) YSZ single crystal substrate by pulsed laser deposition. During the film deposition, the substrate temperature was kept at 750 °C and the oxygen pressure was kept at 10 Pa. Resistivity of the resultant films was measured by dc four-probe method with van der Pauw configuration. The thermopower was measured by standard steady state method. All measurement was performed in air at room temperature.

The as-grown sample showed insulating $\rho-T$ behavior, which is consistent with a previous study.[3] With increasing the oxidation state, the $\rho-T$ approached to that of SrCoO$_{3-\delta}$. These results confirmed that x in the SrCoO$_x$ films could be modulated from 2.5 to 3. Steep decreases of both resistivity (ρ) and the absolute value of thermopower (S) of the oxidized SrCoO$_x$ epitaxial films resembled percolation theory, which indicate that the columnar oxidation initially occurs normal to the surface then spread parallel to the surface. To visualize this phenomenon directly, we observed the conducting region using the conductive AFM (Figure 1e-h). The topographic AFM images were similar, but the electric current mappings clearly show the evolution of the conducting region, which indeed develops percolation paths.

Figure 1. Topographic AFM images (2 μm × 2 μm) and the respective electric current mapping of (a,e) sample A (24.4 %), (b,f) sample B (34.5 %), (c,g) sample C (60 %) and (d,h) sample D (84.7 %). Evolution of conductivie percolation paths can be observed from (e) to (f).

We successfully visualized the electrochemical oxidation of SrCoO$_x$ at macroscopic scale. The columnar oxidation firstly occurred along the surface normal then spread parallel to the surface. These results will be valuable for developing a SrCoO$_x$ based functional electrochemical device.

References

[1] T. Katase et al., Adv. Electron. Mater. **2**, 1600044 (2016). [2] Q. Y. Lu and B. Yildiz, Nano Lett. **16**, 1186 (2016). [3] N. P. Lu et al., Nature **546**, 124 (2017). [4] H. Jeen et al., Nature Mater. **12**, 1057 (2013). [5] **Q. Yang**, et al., Adv. Mater. Interfaces 1901260 (2019).
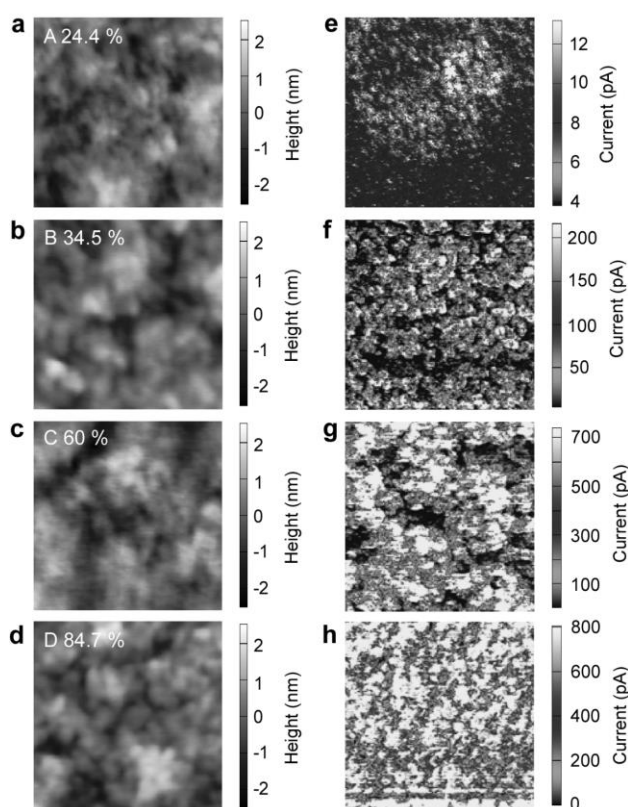
Effect of Heat Treating on Electronic ad Structural Properties of Lightly Doped Epitaxial La$_x$Ba$_{1-x}$SnO$_3$ Films

Takashi Fujimoto[1], Hai Jun Cho[1,2], and Hiromichi Ohta[1,2]

[1]School of Engineering, Hokkaido University, Sapporo 060-0814, Japan
[2]Research Institute for Electronic Science, Hokkaido University, Sapporo 001-0020, Japan

La-doped BaSnO$_3$ (LBSO) is a promising optoelectronic material because LBSO single crystal exhibit a wide band gap (3.1 eV) and very high mobility (320 cm^2 V^{-1} s^{-1}) with a high carrier concentration.[1] However, the mobility of LBSO film is much lower than the single crystal value, and researchers have been focusing on fabricating LBSO films with high mobilities. In one of the studies, Cho *et al.* found that vacuum annealing improves the mobility of LBSO films. The mobility enhancements were attributed to the lateral grain growth, but grain growth only occurred when La doping was greater than 1%. [2] To fully understand the mobility of LBSO films, it is necessary to achieve grain growth in lightly doped ($<$ 1%) LBSO films and examine its effect on the mobility. In this regard, it is necessary to explore the effect of annealing pressure and time on the structural and electronic properties of lightly doped LBSO films since the previous work only looked at the effect of temperature.

LBSO epitaxial films (La = 0.55 %) were fabricated on (001)-oriented MgO substrates using PLD. The films were vacuum annealed at 725 °C at 4 different pressures: 4.0×10^{-4}, 4.0×10^{-3}, 7.0×10^{-2}, and 3.0 Pa. At very low pressures (4.0×10^{-4}, 4.0×10^{-3} Pa), the annealing time was 30 mins. On the other hand, at 7.0×10^{-2} Pa and 3.0 Pa, the annealing times were 1 hour and 3 hours, respectively. The electron transport properties of the films were measured at room temperature by the conventional dc 4-probe method in van der Pauw geometry.

In **Fig. a**, grain growth can be observed only at low pressures ($< 4.0 \times 10^{-3}$ Pa). No grain growth occurred at high pressures although the annealing time was longer. This shows the annealing pressure is more important than the annealing time for grain growth in LBSO films. Hall mobilities increased after annealing (**Fig. b**). Interestingly, the highest mobilities were observed from the film annealed at 7.0×10^{-2} Pa for 1 h although there was no grain growth. While more oxygen vacancy formation at low pressures is possible, these results strongly suggest that threading dislocation are not important in lightly doped LBSO films. The difference in the annealing time indicates that the activation of La dopants and strain relaxation are more important.

In this study, we examined the effect of heat treating pressure and time on the electrical and structural properties of LBSO films. The results show that grain growth at low doping is possible at low pressures, but the mobilities after vacuum annealing were not proportional to the grain sizes. This suggests that understanding lattice strains and dopant activation is more important in lightly doped LBSO films.
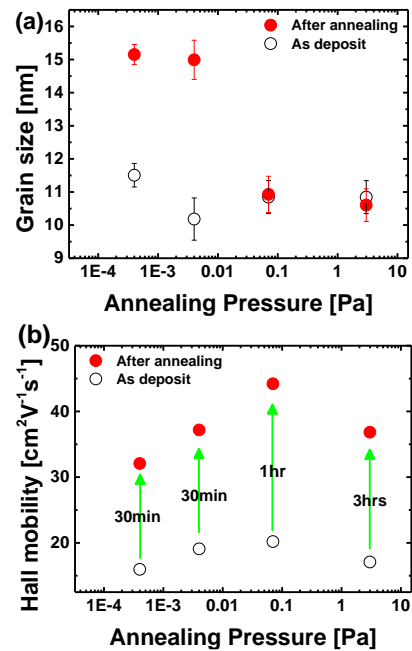

Fig. (a) grain size of as deposit sample and after annealing sample with different pressure annealing. (b) hall mobility of as deposit sample and after annealing sample with different pressure annealing.

References

1. H. J. Kim *et al.*, *Appl. Phys. Express* **5**, 061102 (2012).
2. H.J. Cho *et al.*, *APL Mater.* 7, 022507 (2019).

Thermal Conductivity of Layered Cobalt Oxide Epitaxial Films with Different Crystallographic Orientation

Yugo Takashima[1], Takaki Onozato[1], Hai Jun Cho[1,2], and Hiromichi Ohta[1,2]

[1]IST-Hokkaido University, Sapporo 060-0814, Japan
[2]RIES-Hokkaido University, Sapporo 001-0020, Japan

The layered cobalt oxide, $A_x CoO_2$ (A = Li, Na, Ca, and Sr), has a crystal structure in which the A_x planes and CoO_2 layers composed of a ridge-sharing CoO_6 octahedra are alternately stacked along the c-axis. This structure makes $A_x CoO_2$ highly anisotropic. For example, the electrical conductivity in the ab-plane is orders of magnitude larger than that along the c-axis.[1] Similarly, a large anisotropy is expected for thermal conductivity, but it has not been clarified. In this study, $A_x CoO_2$ epitaxial thin films with two different crystallographic orientations were fabricated on (0001)- and (1-100)-oriented sapphire substrates to clarify the anisotropy of thermal conductivity as well as the effect of A_x ions.

The $Na_{0.8}CoO_2$ epitaxial thin film was fabricated on the (0001) and (1-100) α-Al_2O_3 substrates by reactive solid-phase epitaxy (R-SPE)[2]. The ab-plane is parallel and inclined by 43° to the substrate surface on the (0001) and (1-100) α-Al_2O_3 substrate, respectively[3]. The $A_x CoO_2$ epitaxial thin films (A = Li, Ca, Sr) were fabricated by the ionic exchange of Na^+ to Li^+, Ca^{2+}, or Sr^{2+}. The cross-plane thermal conductivity of thin film was measured by the time-domain thermoreflectance (TDTR) method. The thermal conductivities in the perpendicular direction and the parallel direction were analytically extracted from the observed thermal conductivity.

The XRD pattern of the films found the (0001) Bragg peak of The $A_x CoO_2$ (A = Na, Li, Ca, Sr) films with the (0006) Bragg peak of the sapphire substrates.

Fig. 1 | Thermal conductivity of the $A_x CoO_2$ epitaxial films at room temperature. Both anisotropy and atomic mass (A_x) dependences are clearly seen.

The peak suggests that films have high crystallinity, and we could fabricate epitaxial films. The $A_x CoO_2$ film surface was shown flat and rod-shaped domains on the (0001) and (1-100) α-Al_2O_3 substrate, respectively. Therefore, the change of the deposition direction depending on the substrate was confirmed. Regardless of the type of A ions, the thermal conductivity along $ab_{//}$ was greater than that along $ab_\perp$. We have succeeded in measuring clear thermal conductivity anisotropy (Fig.1). In addition to the orientations, the thermal conductivity values were also significantly affected by the A_x ions between the CoO_2 layers. The thermal conductivity along $ab_{//}$ decreased with increasing A atomic. It is considered that the mass of A ions has some effect on the heat transport properties of the CoO_2 layers.

We measured the anisotropic heat transport properties of $A_x CoO_2$ epitaxial thin films fabricated on the (0001) α-Al_2O_3 and (1-100) α-Al_2O_3 substrates by R-PSE method. In addition to the orientation dependent thermal conductivity, it was also shown that the thermal conductivity decreases with increasing A_x atomic weight (A atomic weight $\times$ x) in both $ab_{//}$ and $ab_\perp$ directions. These results demonstrate the systematic engineering of material properties, where replacing A with heavy metal to decrease the thermal conductivity while maintaining a large power factor (electrical conductivity[2] $\times$ thermopower).

References
1. I. Terasaki *et al.*, *Phys. Rev. B* **56**, R12685 (1997).
2. H. Ohta *et al.*, *Cryst. Growth Des.* **5**, 25 (2005).
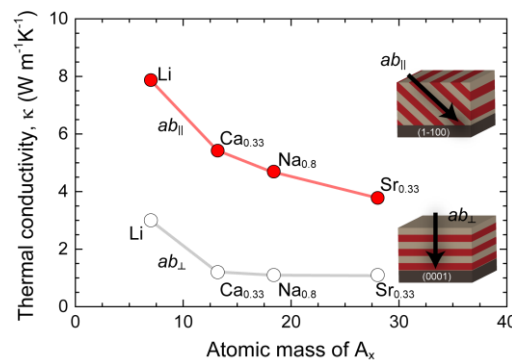3. K. Sugiura *et al.*, *Appl. Phys. Lett.* **94**, 142105 (2009).

Thermal Conductivity of InGaO$_3$(ZnO)$_m$ (m = integer) Natural **P41**

Superlattice

Yuzhang Wu,[1] Hai Jun Cho,[1,2] Bin Feng,[3] Masashi Mikami,[4] Woosuck Shin,[4] Yuichi Ikuhara,[3] Keiji Saito,[5] and Hiromichi Ohta[1,2]

[1]Graduate School of Information Science and Technology, Hokkaido University, Sapporo, Japan, [2]Research Institute for Electronic Science, Hokkaido University, Sapporo, Japan [3]Institute of Engineering Innovation, The University of Tokyo, Tokyo, Japan, [4]Inorganic Functional Materials Research Institute, National Institute of Advanced Industrial Science and Technology (AIST-Chubu), Nagoya, Japan, [5]Department of Physics, Keio University, Yokohama, Japan
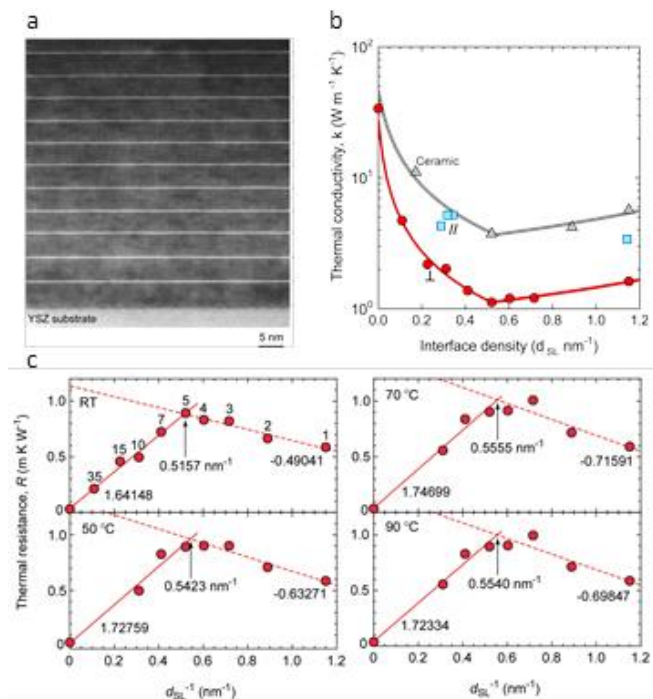
Clarification of heat transport behavior in superlattices is crucial for heat modulation devices technique. However, the intrinsic properties of superlattices are challenging to explore due to the presence of defects in ceramics, polycrystal, and artificial superlattice [1]. To solve this issue, we focus on the homologous phases $InMO_3(ZnO)_m$ (M = In, Fe, and Ga, m = integer), which forms a natural superlattice composed of alternatively stacked InO_2^- layers and $MO_3(ZnO)_m^+$ blocks (**Fig. 1a**). Here we report heat transport behavior of single crystalline $InGaO_3(ZnO)_m$ ($m = 1-35$) fabricated by the Reactive Solid Phase Epitaxy (R-SPE) [2] method and measured their thermal conductivity (κ).

Like other superlattices, we observed the cross plane thermal conductivity was not monotonic as function of interface density d_{SL}^{-1} (**Fig. 1b**). These suggests that phonon propagation change from incoherent ($d_{SL}^{-1} < 0.5$ nm^{-1}) to coherent ($d_{SL}^{-1} > 0.5$ nm^{-1}), and the transition point shift to the right with increasing temperature (**Fig. 1c**). This implies that the phonon coherence length in $InGaO_3(ZnO)_m$ is 2 nm at 300 K, which determines the heat transport properties in superlattices. In addition, the in-plane thermal conductivities were close to those of polycrystalline ceramics, suggesting the in-plane thermal conductivity dominates ceramics.

In this research, we examined the heat transport properties of single crystalline films of $InGaO_3(ZnO)_m$ ($m = 1-35$, integer) natural superlattices and analyzed their thermal conductivities. The results indicate cross-plane phonon propagation is a competition between interface scattering and phonon band folding, and the transition point is at the phonon coherence length. These results would be valuable for heat management technologies.

FIG. 1 | **a.** HAADF-STEM image of $InGaO_3(ZnO)_m$ film grown on (111) YSZ substrate. **b.** Thermal conductivity κ as function of interface density d_{SL}^{-1} in the cross-plane direction (circle), in-plane direction (square) and polycrystalline ceramics (triangle). **c.** Thermal resistance $(1/\kappa)$ as function of d_{SL}^{-1} at RT, 50 °C, 70 °C, and 90 °C.

References
1. J. Ravichandran *et al. Nature Mater.*, **13**, 168 (2014).
2. H. Ohta *et al.*, *Adv. Funct. Mater.* **13**, 139 (2003); K. Nomura *et al.*, *Science* **300**, 1269 (2003).

pH-induced Changes in Gold Nanorod Orientation   P42

on Polymer Brush Substrates

Yu Sekizawa,[1] Hideyuki Mitomo,[2,3] Satoshi Nakamura,[4]
Yusuke Yonamine,[2,3] and Kuniharu Ijiro,[2,3]

[1]*Graduate School of Life Science, Hokkaido University, Japan*
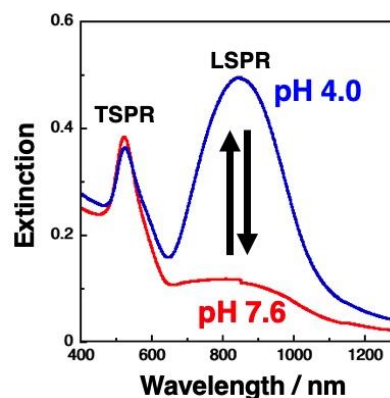[2]*Research Institute for Electronic Science, Hokkaido University, Japan*
[3]*Global Institution for Collaborative Research and Education, Hokkaido University,
Japan,* [4]*National Institute of Advanced Industrial Science and Technology (AIST), Japan*

Gold nanoparticles have attracted attentions in various research fields due to their useful optical properties, known as Localized Surface Plasmon Resonance (LSPR). In particular, rod-shaped gold nanoparticles (gold nanorods: GNRs) show two modes of LSPR due to their anisotropy; One is Transverse LSPR (TLSPR) with absorption at about 500-600 nm, and the other one is Longitudinal LSPR (LLSPR) with absorption in the near-infrared region. As the LLSPR of GNRs possesses much stronger light absorption than the TLSPR of GNRs and LSPR of spherical gold nanoparticles, an effective use of this LLSPR is quite important. On the other hand, this absorption is significantly dependent on the orientation of GNRs toward incident light. Therefore, orientation control of GNRs is of great importance. Further, dynamic orientation control of GNRs must lead to new plasmonic devices with promising functionality. However, the orientation control of GNRs remains challenging. In our previous research, we developed a preparation method for the vertically aligned GNR array on DNA-modified substrates (Fig. 1a) [1]. In this study, we investigated the orientational change of GNRs by pH-induced structural transformation of double-stranded DNA (Fig. 1b), as there are many reports showing the DNA conformation changes depending on the external environment [2].
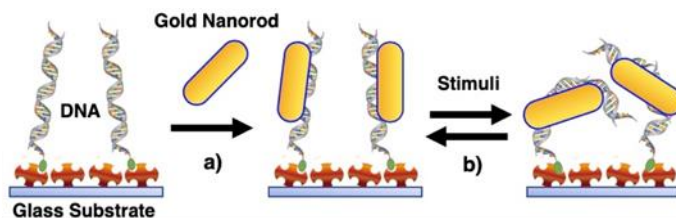
Figure 1. Schematic illustration of the immobilization of cationic GNRs onto the DNA grafted substrates (a) and stimuli-responsive structural changes (b)

DNA brushes were prepared through the immobilization of biotin-modified DNAs (148bp) on streptavidin-coated glasses. The GNRs, which have 36 nm in length and 9 nm in diameter, were prepared and their surface was modified with a cationic and neutral ligands at a mixing ratio of 9:1. Then, cationic GNRs were adsorbed onto the DNA brushes via electrostatic interaction. Extinction spectra of GNRs were measured under various pH conditions. The extinction spectra in a neutral environment (pH 7.6) showed that the GNRs were aligned perpendicular to the glass substrate. When the pH environment was changed to an acidic (pH 4.0), the LLSPR intensity around 800 nm was largely increased (Fig. 2). This result indicates that the orientation of cationic GNRs changed drastically due to the pH changes. When the solution condition was returned to neutral, the increased peak was immediately back to the original position. This peak changes occurred reversibly at least several cycles. Our results suggested reversible GNR orientation changes from conformation changes of DNA as a supporting material on the substrate.

Figure 2. Extinction spectra of GNRs attached on the DNA brush in pH 7.6 (Red) and pH 4.0 (Blue)

Reference

1. S. Nakamura, *et al*, *ACS Omega*, **2**, 2208-2213 (2017)

A Novel Approach for Tuning of Assembly Temperature of Thermo-responsive Gold Nanoparticles

Yier Shi, [1] Hideyuki Mitomo,[2,3] Yusuke Yonamine,[2,3] Kuniharu Ijiro[2,3]

[1]Graduate School of Life Science, Hokkaido University, Japan
[2]Research Institute for Electronic Science, Hokkaido University, Japan
[3]Global Institution for Collaborative Research and Education, Hokkaido University, Japan

Gold nanoparticles (AuNPs) show a unique optical property called localized surface plasmon resonance. Their assemblies, interestingly, show collective or enhanced properties due to plasmon coupling effects. Thus, the assemblies of AuNPs, in particular, stimuli-responsive assembly/disassembly, have attracted much attentions. In our previous study, we found that AuNPs coated with oligo(ethylene glycol) (OEG) derivatives showed thermo-responsiveness [1]. They formed assemblies when the solution was heated over a temperature, which we called assembly temperature. Those assembly temperatures were drastically changed depending on the hydrophobicity at the terminus of the ligand and the size of nanoparticles as a core (Fig. 1). On the other hand, it was hard to tune the assembly temperature precisely using AuNPs with a defined size. In this study, we show a new method to tune the assembly temperature of AuNPs by changing the free volume of the surface ligands instead of a change in AuNP size.
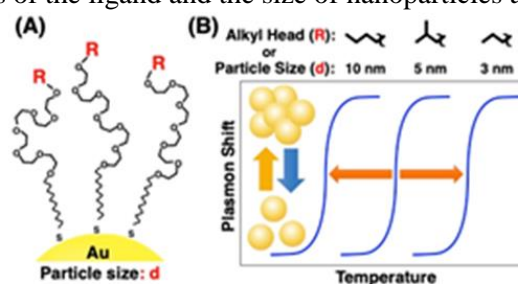

Fig. 1 (A) Illustration of a thermo-responsive gold nanoparticle. (B) Schematic diagram of temperature responsive plasmon shifts coming from nanoparticle assembly
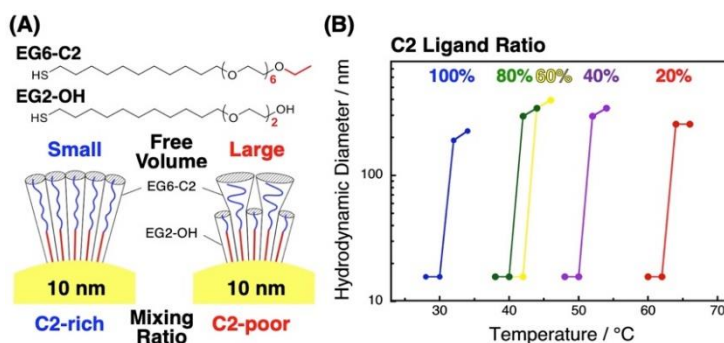
First, 10 nm AuNPs were synthesized and modified with the ligands of **EG6-C2** as thermo-responsive one and **EG2-OH** as a short ligand at various mixing ratios (Fig. 2A). A free volume of the OEG parts in **EG6-C2** changes depending on the ligand mixing ratio. The thermo-responsive behaviors of these AuNPs were analyzed by dynamic light scattering (DLS) and UV-vis spectroscopy. The DLS on heating process showed that AuNPs modified with different mixing ratio of the ligands formed assemblies at different temperatures (Fig. 2B). Spectral analyses also showed these AuNPs had different assembly temperature. These results indicated that the assembly temperature can be tuned by change in mixing ratio of surface ligands with different ethylene glycol length due to the change in the free volume of the OEG parts in thermo-responsive ligands. On the other hand, two different thermo-responsive ligands (**EG6-C2** and **EG6-C1**), which show different assembly temperatures, were mixed and attached on the 10 nm AuNPs. **EG6-C2** (100%) and **EG6-C1** (100%) covered AuNPs showed an assembly temperature to be ca. 34 and 63°C, respectively. However, the mixture (75:25, 50:50, and 25:75 of **EG6-C2**: **EG6-C1**) showed ca. 36, 38, and 38°C, respectively, somehow. These results suggest this free volume-based assembly temperature control is advantageous.

Fig. 2 (A) Chemical structures of surface ligands and schematic illustration of ligands at the nanoparticle surface. (B) Hydrodynamic diameter changes of AuNPs covered with mixed ligands on the heating process.

Reference

1. R. Iida, H. Mitomo, Y. Matsuo, K, Niikura, and K. Ijiro, *J. Phys. Chem. C*. **120**, 15846–15854 (2012).

Enhanced Hot-Electron Transfer under Modal Strong Coupling Conditions with Sacrificial Electron Donors   P44

Yanfeng Cao[1], Tomoya Oshikiri[1], Xu Shi[1], Hiroaki Misawa[1,2]

[1]*Research Institute for Electronic Science, Hokkaido University, Sapporo, Japan.*
[2]Center for Emergent Functional Matter Science, National Chiao Tung University,
Taiwan

Recently, we reported a modal strong coupling between Fabry–Pérot nanocavity (FP-nanocavity) mode and localized surface plasmon resonance (LSPR) enhanced water splitting reaction by optical hybrid modes across a broad range of wavelengths, followed by hot-electron transfer from a plasmonic metal to a semiconductor [1]. In particular, it should be noted that in addition to the absorption increment, the internal quantum efficiency (IQE) is enhanced under strong coupling.

In this study, we investigated the efficiency of hot-electron transfer under modal strong coupling conditions by monitoring the photocurrent generated at a plasmonic photoanode. We fabricated gold nanoparticles/titanium dioxide/Au-film structure that shows a modal strong coupling between FP-nanocavity mode and LSPR and then explored the effect of the strong coupling on the incident photon-to-current conversion efficiency (IPCE) and IQE in the presence of triethanolamine (TEOA) as a sacrificial electron donor to accelerate the surface reaction enough[2].

Silica glass substrates ($10\times10\times1.0$ mm^3) were ultrasonically cleaned for 5 min each in acetone, methanol and deionized water. Then, the substrates were dried with a pure nitrogen flow. A 100 nm Au film and a 2 nm titanium film were sputtered in sequence on the surface of the silica glass using a Helicon sputtering system. Afterward, a 28 nm titanium dioxide (TiO_2) thin film was deposited onto the Au film using a commercial hot-wall flow-type atomic layer deposition (ALD) reactor with titanium tetrachloride ($TiCl_4$) and H_2O as precursors; the chamber was held at 300°C. A 3 nm Au thin film was sequentially evaporated in a thermal evaporator at a deposition rate of 0.1 Å$\cdot$s^{-1}. Finally, the samples were annealed in air at 300 °C for 2 h, and the Au-NPs appeared on the TiO_2 film surface. To fabricate the partially inlaid Au NPs, a 7 nm TiO_2 thin film was also deposited on the Au-NPs/TiO_2/Au-film by ALD. Then, the samples were annealed in air at 300 °C for 2 h.

The typical current-potential curves were achieved using a three-electrode system, with the obtained Au-NPs/TiO_2/Au-film structure as the working electrode (WE), a platinum wire as the counter electrode (CE) and a saturated calomel electrode (SCE) as the reference electrode (RE). For the IPCE calculation, the photocurrent was measured at 0.3 V vs. SCE.

Au-NPs/TiO_2/Au-film photoanode was fabricated according to the previous report [1]. The absorption spectrum showed distinct dual bands, which corresponded to the strong-coupling-induced splitting of energy levels into upper and lower branches. The IPCE was dramatically enhanced as the TEOA concentration increased, and finally, the IPCE reached a maximum of ca. 4%. This maximum IPCE value is twice that of the Au-NPs/TiO_2/Au-film without partially inlaying Au-NPs by TiO_2 whose coupling strength is weaker. Thus, the hot-electron transfer efficiency depends on the strong coupling situations. Additionally, both hybrid modes formed by the modal strong coupling between the FP-nanocavity and LSPR contributed to the hot-electron transfers and photocurrent generation in the presence of TEOA because all spectra can be separated into two peaks. Furthermore, the integrated IQE, which was obtained for wavelengths from 500 to 800 nm, was enhanced by approximately 5 times upon the addition of 1 vol % of TEOA and reached 3%. This large IQE is profitable for solar energy usage because 40% of solar energy is included in this wavelength region.

References
1. X. Shi, K. Ueno, T. Oshikiri, Q. Sun, K. Sasaki, H. Misawa, *Nat. Nanotechnol.*, **2018**,13, 953–958.
2. Y. Cao, T. Oshikiri, X. Shi, K. Ueno, J. Li, H. Misawa, *ChemNanoMat* **2019**, 5, 1008-1014.

Injection Compression Molding of Transmission-Type Fano Resonance Biochips for Multiplex Sensing Applications

Kuang-Li Lee[1], Meng-Lin You[1], Xu Shi[2], Yi-Ru Li[1], Kosei Ueno[3], Hiroaki Misawa[2], Pei-Kuen Wei[1]

[1]Research Center for Applied Sciences, Academia Sinica, Taipei 11529, Taiwan
[2]Research Institute for Electronic Science, Hokkaido University, N21, W10, Kita-ku, Sapporo, Hokkaido 001-0021, Japan, [3]Department of Chemistry, Hokkaido University, Kita-10 Nishi-8, Kita-ku, Sapporo 060-0810, Japan

Nanostructure-based surface plasmon resonance biosensors have attracted considerable attention since the phenomenon of extraordinary light transmission in metallic nanohole arrays was discovered. However, the mass production of uniform metallic nanostructures with a low-cost, rapid, and high-throughput fabrication process remains a key issue for various multiplex sensing applications. We successfully utilized injection compression molding to mass fabricate transmission-type Fano resonance biochips with a feature size of 60 nm for multiplex sensing applications. Two types of metallic nanostructures, aluminum nanoslits and capped aluminum nanoslits with 24 sensing arrays, were made on polycarbonate substrates. The bulk sensitivity and uniformity of the nanostructure arrays were tested. A Fano resonance with a full-width at half-maximum bandwidth of 8 nm was observed in the visible light region for 470-nm-period capped aluminum nanoslit arrays. The refractive index sensitivity was 460 nm/RIU, and a figure of merit of 58 was achieved. Moreover, aluminum nanoslits had a dip resonance with a bandwidth of 25 nm and a refractive index sensitivity of 463 nm/RIU. The coefficients of variation of the refractive index sensitivities for 24 arrays on a biochip and 10 biochips from different fabrication batches were both below 3%, which indicates that uniform nanostructures can be fabricated by injection compression molding and that the reproducibility is controllable. In addition, the multiplex sensing capability of the aluminum nanostructure arrays was demonstrated by simultaneously monitoring 24 water/glycerin solutions with a hyperspectral imaging system. Protein–protein interactions between bovine serum albumin and anti-bovine serum albumin demonstrated proof of concept of the biological detection capability of the chips. To benefit various multiplex sensing applications such as clinical disease diagnosis, drug screening, and protein biomarker discovery, 96-array aluminum nanoslit biochips the same size as a standard 96-wellplate were successfully fabricated. Such a nanostructure-based plasmonic biochip produced by a low-cost, rapid, and high-throughput fabrication method can benefit commercial applications.
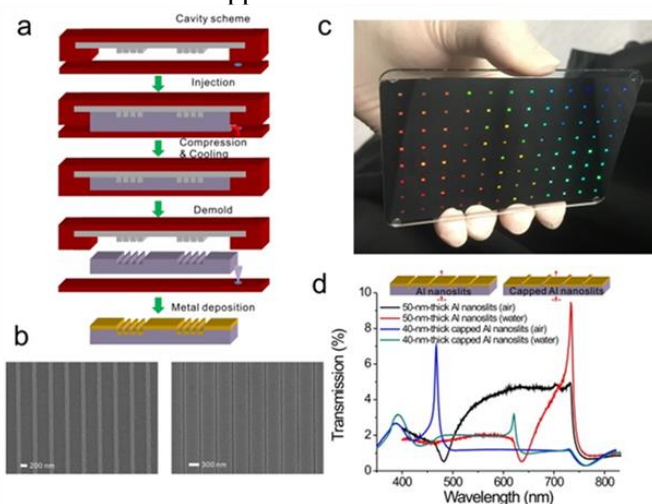
Fig. 1. Fabrication and transmission spectra of capped aluminum nanoslits and aluminum nanoslits.

Reference
1. K. L. Lee, M. L. You, X. Shi, Y. R. Li, K. Ueno, H. Misawab, and P. K. Wei, *Appl. Mater. Today*, **2019**, 16, 72-82.

Influence of Particle Density on Modal Strong Coupling between Localized Surface Plasmon and Fabry-Perot Nanocavity Modes   **P46**

Yen-En Liu,[1] Xu Shi,[1] Quan Sun,[1] Tomoya Oshikiri,[1] Kosei Ueno,[2] Hiroaki Misawa[1,3]

[1]*Research Institute for Electronic Science, Hokkaido University, Japan*
[2]*Faculty of Science, Hokkaido University, Japan*
[3]*Center for Emergent Functional Matter Science, National Chiao Tung University, Taiwan*

Modal strong coupling between the Fabry–Pérot nanocavity and localized surface plasmon resonance (LSPR) has recently been demonstrated to be helpful for improving the quantum efficiency of the photoelectrochemical (PEC) reaction.[1] In order to further investigate the mechanism of modal strong coupling enhanced hot electron production, in this study, we employed well-designed Au nanodisks (Au-NDs) to further study the key parameters of the modal strong coupling between the nanocavity resonance and LSPR and its effect on the PEC reaction efficiency.

The photoelectrode consists of a sandwich structure of Au-NDs/TiO_2/Au-film (ATA). The Au-film was deposited on silica glass by helicon sputtering following with a 2-nm Ti deposition. The TiO_2 thin-film was fabricated on the Au-film using atomic layer deposition (ALD) to form a nanocavity. Well-designed Au-NDs with hexagonal arrangement were fabricated using electron beam lithography and lift off techniques. For the incident photocurrent conversion efficiency (IPCE) measurement, we fabricated an ATA photoelectrode consisted of a large area (~2 x 2 mm) of Au-NDs array with an inlaid depth of 7 nm. The IPCE measurement was performed using a three-electrode system in 0.1 M $KClO_4$ solution with 1 vol% triethanolamine as a sacrificial electron donor. The ATA photoelectrode was used as working electrode, a saturated calomel electrode and Pt wire were used as reference and counter electrode, respectively. Dephasing time measurement was carried out in a time resolved photoemission electron microscopy (TR-PEEM).[2]

An obvious absorption band splitting for the ATA structures to an upper and a lower branch was observed due to the modal strong coupling between LSPR and cavity resonance. The dispersion curves were plotted as a relationship between the cavity resonance energy and the upper/lower absorption band energy. By fitting the dispersion curve by a coupled harmonic oscillator model, the splitting energy of the ATA with the coverage ratio (CR) of Au-NDs of 0.403 was calculated to be 380 meV, where the CR is obtained by dividing the gold coverage area by the total surface area. To control the strong coupling strength, we varied the CR of Au-NDs from 0.074 to 0.580 with corresponding splitting energies from 90 to 510 meV. We performed PEC measurement by employing the ATA structures with different CR as a photoanode to investigate how the modal strong coupling enhances the charge generation. For the Au-NDs with a lower CR, the absorption band and the IPCE band show only a single band at around 700 nm. For the Au-NDs with a higher CR, strong coupling induced two absorption bands exhibiting at the wavelength region of 550-900 nm. Remarkably, the IPCE action spectrum also presents two bands corresponding to the absorption bands closely. From the experiment and fitting of the photoemission signal of Au-NDs with high and low CR, we found that Au-NDs with high CR exhibits a relatively short decay (~ 4.5 fs), while the low CR shows a longer decay (~9 fs). Based on the IPCE and dephasing measurements, we consider that a larger number of hot-electron is generated and injected from Au-NDs into TiO_2 under the modal strong coupling conditions with the larger coupling strength.

References

1.   X. Shi, K. Ueno, T. Oshikiri, Q. Sun, K. Sasaki and H. Misawa, *Nat. Nanotechnol.*, 2018, 13, 953-958.
2.   J. Yang, Q. Sun, K. Ueno, X. Shi, T. Oshikiri, H. Misawa, Q. Gong, *Nat. Commun.*, 2018, 9, 4858.

Revealing Plasmon Coupling in Plasmonic Dimers and One-Dimensional Chains Directly from the Near Field

Quan Sun[1, †], Yaolong Li[1,2], Shuai Zu[1], Xu Shi[1], Oshikiri Tomoya[1], Kosei Ueno[1,†], Qihuang Gong[2], and Hiroaki Misawa[1,3]

[1]*Research Institute for Electronic Science, Hokkaido University, Sapporo 001-0021, Japan,* [2]*School of Physics, Peking University, Beijing 100871, China*
[3]*Center for Emergent Functional Matter Science, National Chiao Tung University, Hsinchu 30010, Taiwan,* [†]*Present address: Department of Chemistry, Faculty of Science, Hokkaido University, Sapporo 060-0810, Japan*

Plasmonic dimers and one-dimensional (1-D) nanochains are the simplest coupled plasmonic systems. Here, we study the near-field properties of plasmon coupling in these two systems using photoemission electron microscopy (PEEM), which has been proved to be a powerful and promising approach to probe the near field of plasmonic nanostructures[1-3].

For the plasmonic dimers, it has been well known that much stronger near-field enhancement can be obtained in dimers compared to single nanoparticles. However, the correlation between near-field enhancement and dephasing time has not been clearly addressed so far. We experimentally reveal such correlation with time-resolved PEEM. The correlation is found to depend on the dimer gap size and polarization of the excitation light[4]. Compared with isolated particles, dimers with small gap size show much stronger near-field enhancement and much shorter dephasing times. The experimental results are well reproduced by finite-difference time-domain (FDTD) simulations and further explained by coupled dipole approximation (CDA) model calculations. The roles of near-field and far-field coupling and plasmon localization are unveiled in balancing near-field enhancement and dephasing time. We also reveal that the near-field enhancement of dimers may be weaker than that of isolated structures if the gap size is not sufficiently small.

For 1-D nanochains, the near field mapping is obtained at high spatial resolution. By tuning the excitation laser wavelength, we can obtain the near-field spectra, from which the energy splitting between longitudinal (L) and transverse (T) plasmon modes can be revealed. In particular, the L-mode red shifts and the T-mode blue shifts with increasing chain length. The red shift of the L-mode is highly dependent on the gap distance. In contrast, the T-mode almost remains constant within the range of gap distance we investigated. This energy splitting between the L-mode and the T-mode of metallic chains is in good agreement with the far-field measurements. Our results provide direct experimental proof of the near-field plasmon coupling in nanochains. In addition, we explore the energy transport along the gold nanochains under excitation at oblique illumination *via* PEEM measurements together with numerical simulations[5].

In conclusion, we have studied plasmon coupling in plasmonic dimers and 1-D nanochians directly from the near field with PEEM. We explore the correlation between near-field enhancement and dephasing time in plasmonic dimers. The roles of near-field and far-field coupling and plasmon localization are unveiled in balancing near-field enhancement and dephasing time. For the 1-D Au nanochains, we prove the plasmon coupling directly at near field. Energy transport along the nanochains are also explored, making possible applications for plasmonic waveguides.

References
1. Q. Sun, K. Ueno, H. Yu, A. Kubo, Y. Matsuo, and H. Misawa, *Light: Sci. Appl.* **2013**, 2, e118.
2. Q. Sun, H. Yu, K. Ueno, A. Kubo, Y. Matsuo, and H. Misawa, *ACS Nano* **2016**, 10, 3835−3842.
3. H. Yu, Q. Sun, K. Ueno, T. Oshikiri, A. Kubo, Y. Matsuo, and H. Misawa. ACS Nano, **2016**, 10, 10373−10381.
4. Y. Li, Q. Sun, and H. Misawa, et al., under review in *Phys. Rev. Lett.*
5. Q. Sun, H. Yu, K. Ueno, S. Zu, Y. Matsuo, and H. Misawa, *Opto-Electron. Adv.* **2019**, 2, 180030.

Plasmon-induced Photocurrent Generation on Ga_2O_3 Loaded with Gold Nanoparticles   P48

Yaguang Wang,[1] Xu Shi,[1] Tomoya Oshikiri,[1] Kosei Ueno,[2] Hiroaki Misawa[1,3]*

[1]*Research Institute for Electronic Science, Hokkaido University, Sapporo, Japan.*
[2]*Faculty of Science, Hokkaido University, Sapporo, Japan*
[3]*Center for Emergent Functional Matter Science, National Chiao Tung University, Hsinchu, Taiwan*

Ga_2O_3 is a promising photocatalyst with the more negative conduction band compared to commonly used TiO_2 which is beneficial to improving efficient water splitting. However, the wide bandgap makes it inactive in the visible light region [1]. In our proposal, gold nanoparticles (Au-NPs) are utilized to increase the photocatalytic activities in the visible light region due to the localized surface plasmon resonance. And the separation of plasmonically excited electron-hole pairs is achieved by the Schottky junction constructed at the interface between Au and semiconductor [2]. The electrons on the conduction band of Ga_2O_3 could take part in the reduction of water to produce H_2. Meanwhile, the oxidation process is conducted by holes to achieve the evolution of O_2. Therefore, the interface between Au-NPs and Ga_2O_3 plays important role for efficient energy conversion. In this work, the size effect of Au-NPs was investigated and an interfacial modification with thin TiO_2 layer was applied to improve the photochemical performance of Au-NPs/Ga_2O_3 based plasmonic photoelectrode taking advantage of the strong holes-trapping ability of TiO_2.

Different sizes of Au-NPs were obtained from Au film with various thicknesses deposited onto Ga_2O_3 (Sn-doped, (-201)) upon annealing process under 800°C in N_2 for 1h. Then a thin TiO_2 layer with several nanometers was deposited on the Au-NPs/Ga_2O_3 by atomic layer deposition (ALD) under 300°C. PEC performance was measured under the conventional three-electrode photoelectrochemical measurement system with a saturated calomel electrode as reference electrode, a Pt wire as a counter electrode and an aqueous electrolyte solution of $KClO_4$ (0.1 M).

To improve the oxidation process in the water splitting, TiO_2 was applied on Au-NPs/Ga_2O_3 system taking advantage of the holes capture ability. The incident photon-to-current efficiency (IPCE) and absorption spectra of the Au-NPs/Ga_2O_3 system showed an increment compared with samples without the interface modification. When 1 nm TiO_2 was deposited, the IPCE decreased because 1 nm is too thin to form smooth layer which would act as recombination centers. Deposition of 2 nm TiO_2 showed the highest IPCE which was 1.6 times larger compared with samples without TiO_2. It meant that the modification by TiO_2 showed positive effect on Au-NPs/Ga_2O_3 as a result of the hole-trapping ability of TiO_2 decreasing the recombination between holes and electrons.

References

1. K. Maeda, K. Domen, *J. Phys. Chem. C*, 111 (**2007**) 7851-7861.

2. Y. Nishijima, K. Ueno, Y. Yokota, K. Murakoshi, H. Misawa, *J. Phys. Chem. Lett.* 1 (**2010**) 2031-2036.

Plasmon-induced Energetic Electron Transfer in Modal Strong Coupling Regime　　　P49

X. Shi[1], G. He[1], T. Oshikiri[1], Q. Sun[1], K. Ueno[2], H. Misawa[1,3]

1 Research Institute for Electronic Science, Hokkaido University
2 Department of Chemistry, Faculty of Science, and Graduate School of Chemical Sciences and Engineering, Hokkaido University
3 Center for Emergent Functional Matter Science, National Chiao Tung University

Plasmon-induced charge generation has been demonstrated for the solar energy conversions. [1] However, the solar energy conversion efficiency is limited by the insufficient absorption on monolayer of metallic nanoparticles and the low quantum efficiency of the reactions. Aiming at this problem, we have developed an efficient solar-to-fuel energy conversion system based on an Au nanoparticle (Au-NP)/TiO_2 thin-film/Au-film photoelectrode. [2] The Au-NP/TiO_2 thin-film/Au-film photoelectrode shows modal strong coupling between the localized surface plasmon resonance (LSPR) and the cavity mode and the quantum efficiency of plasmon-induced water oxidation on the ATA photoelectrode is enhanced under the strong coupling conditions. The plasmon-induced charge transfer at the interface of Au-NPs/TiO_2 is considered to be a critical factor for this efficient energy conversion system. In this study, we explored the dynamics of the plasmon-induced charge transfer at the interface of Au-NPs/TiO_2 using femtosecond pump-probe transient reflection spectroscopy.

Photoelectrodes consist a sandwich structure of Au-NP on top, TiO_2 thin-film in middle and an Au or Al metal thin film at bottom, represented as Au-NP/TiO_2 thin-film/Au-film (ATA(Au)) and Au-NP/TiO_2 thin-film/Al-film (ATA(Al)). Strong coupling between the Fabry–Pérot nanocavity mode of TiO_2 thin-film/Au-film and the localized surface plasmon resonance (LSPR) mode of Au-NPs is induced when their resonant frequencies overlap. To increase the coupling strength in this strong coupling regime, we partially inlaid the Au-NPs into the TiO_2 nanocavity film by several nanometers. The strong coupling properties between the LSPR and cavity modes were demonstrated in our previous experiments.[2] Obviously, strong coupling induced hybrid states were observed. The IPCE action spectrum of ATA(Au) and ATA(Al) photoelectrodes are almost correspond to the absorption spectrum. Notably, the IPCE of ATA(Al) is extraordinarily enhanced 2.5 times than that of ATA(Au) at strong coupling wavelength region.

To understand the IPCE enhancement on ATA(Al), we measured the dynamics of the plasmon-induced energetic electrons by femtosecond pump-probe transient reflection spectroscopy. Under the photon excitation, plasmon-induced electron transfers from Au-NPs to TiO_2 conduction band, and the electrons in the TiO_2 conduction band shows intra-band absorption from visible to IR region. Therefore. the lifetime of electrons injected from the photon-excited Au-NPs to TiO_2 can be detected by femtosecond pump-probe transient reflection spectroscopy. The time profiles of the transient spectra of ATA(Au) and ATA(Al) photoelectrodes at 3500 nm after excitation by 580 nm and 650 nm femtosecond pulses were recorded. Interestingly, the lifetime of plasmon-induced electrons in ATA(Al) exhibit remarkably longer than ATA(Au) under both 580 and 650 nm excitation. Under the convolved fitting using a three-phase model, the lifetime of ATA(Au) and ATA(Al) are calculated to be 0.3 and 2.8 µs under 580 nm excitation, 0.4 and 9.0 µs under 650 nm excitation, respectively. The long lifetime of plasmon-induced carriers might contribute to the high photocurrent conversion efficiency, corresponding to our photoelectrochemical measurements.

In summary, ATA(Au) and ATA(Al) show similar strong coupling induced hybrid states in visible wavelength region. The IPCE of ATA(Al) exhibits 2.5 times enhancement as compared with ATA(Au) in the strong coupling wavelength region. Furthermore, the lifetime of the plasmon-induced energetic electrons on ATA(Al) was demonstrated to be more than 9 times longer than ATA(Au) under the femtosecond pump-probe transient reflection measurements. The long lifetime of plasmon-induced carriers contributes to the high photocurrent conversion efficiency of ATA(Al).

References
1. K. Ueno, T. Oshikiri, Q. Sun, X. Shi, H. Misawa, *Chem. Rev.*, 118, 2955–2993 (2018).
2. X. Shi, K. Ueno, T. Oshikiri, Q. Sun, K. Sasaki, H. Misawa, *Nature Nanotechnol.*, 13, 953-958 (2018).

Surface Enhanced Raman Scattering Using Modal Strong　　　P50

Coupling

Zang Xiaoqian[1], Kosei Ueno[2], Xu Shi[1], Tomoya Oshikiri[1], Hiroaki Misawa[1,3]

[1]Research Institute for Electronic Science, Hokkaido University, Sapporo, Japan.
[2]Department of Chemistry, Faculty of Science, Hokkaido University, Sapporo, Japan.
[3]Department of Applied Chemistry, National Chiao Tung University, Hsinch, Taiwan

Surface-enhanced Raman scattering (SERS) is a surface-sensitive technique that enhances Raman scattering by adsorbing molecules on rough metal surfaces or nanostructures. It has been widely used for chemical detection [1]. SERS intensity relates to the contributions of electromagnetic enhancement (EM) and chemical enhancement (CM) [2]. The EM describes the electromagnetic field enhancement by plasmon, while CM is a kind of resonance Raman effect that is induced by the interaction between an incident light field and a charge transfer state formed when a molecule having a lone pair is coordinated to the metal surface. Spontaneous Raman scattering is typically very weak and suffered from stability and reproducibility problems [3]. Thus, the development of SERS substrates with high sensitivity, stability and reproducibility remains an active area of research. In the present study, we fabricated a modal strong coupling system, [4] which composes of Au nanoparticles (AuNPs) showing localized surface plasmon and titanium dioxide/gold film (TiO_2/Au-film) nanocavity, for versatile SERS chips and elucidated SERS properties on the structures in detail.

Silica glass substrates with a size of $10 \times 10 \times 1$ mm^3 were rinsed with acetone, methanol and deionized water in an ultrasonic bath for 5 min and then dried with a pure nitrogen flow. A layer of gold film (100 nm) was coated onto glass substrate by Helicon sputtering system with 3-nm Ti as adhesion layer. A 3-nm titanium was additionally deposited on the gold film for the following TiO_2 thin film deposition. A 30 nm TiO_2 film was deposited by atomic layer deposition (ALD) system. The Au nanoparticles (AuNPs) were manufactured on the TiO_2 film by electron beam (BE) evaporation system and annealing procedure. ATA structures were soaked in crystal violet (CV) water solution for 1 hour, and dried immediately after taking out from the solution. Then a certain number of CV molecules were decorated on to the structure. Raman spectra were obtained using a micro-Raman spectroscope system with 532 nm and 785 nm excitation.

SERS spectra (532 nm excitation) of CV molecules at different laser power have been obtained from ATA and AuNPs/TiO_2-film structures. The intensity of SERS signals of CV is linearly increased with the excitation laser intensity. The Raman spectra of CV show a distinct Raman peaks related to the CV spectral feature, and compared with CV on AuNPs/TiO_2-film structures, the intensity of the peaks obtained from ATA structure is significantly enhanced with an enhancement factor about 11. The SERS spectra (532 nm excitation) of CV molecules with different concentration are obtained from ATA. The lowest detectable concentration of CV is taken as 10^{-7} M. The intensity of SERS signals of CV is linearly increased with the logarithm of CV concentration in a certain range.

References
1. F. A. Harraz, A. A. Ismail, H. Bouzid, S. A. Al-Sayari, A. Al-Hajry, and M. S. Al-Assiri, *Appl. Surf. Sci.* **331**, 241–247(2015).
2. M. Inoue, K. Ohtaka, *J. Phys. Soc. Jpn.* **3853**, 52(1983).
3. Y. Yokota, K. Ueno, H. Misawa, *Small* **7**, 252−258(2011).
4. X. Shi, K. Ueno, T. Oshikiri, Q. Sun, K. Sasaki, H. Misawa, *Nat. Nanotechnol.* **13**, 953−958(2018).

Thermal Stability of Proton Conductive Phosphate Glasses Containing Rare Earth Elements　　P51

T. Fang[1,3], T. Tatebayashi[1], M. Fujioka[1], H. Kaiju[2,5], Y. Ren[1,3], G. Zhao[3], M. Jeem[1], M. Ono[1,4], and J. Nishii[1*]

[1]Research Institute for Electronic Science, Hokkaido University, Hokkaido 001-0020 Japan, [2]Faculty of Science and Technology, Keio University, Kanagawa 223-8522, Japan [3]Department of Materials Physics and Chemistry, Xi'an University of Technology, Xi'an 710048, China, [4]Materials Integration Laboratories, AGC Inc., 1150 Hazawa-cho, Kanagawa-ku, Yokohama-shi, Kanagawa 221-8755, Japan, [5]Center for Spintronics Research Network, Keio University, Kanagawa 223 -8522, Japan

Intermediate temperature (200-500°C) fuel cell (IT-FC) is attractive for the future power generation system. In this research, the phosphate glasses containing alkali, alkaline earth and rare earth elements were prepared by the melt-quench method, and then subjected to the alkali-proton substitution technique (APS) to replace Na^+ with H^+ [1]. The influence of alkaline earth and rare earth ions on the thermal stability of the glasses after APS was investigated.

Phosphate glasses of $35NaO_{1/2}$-$2RO$-$5REO_{3/2}$-$5GeO_2$-$53PO_{5/2}$ (R=Mg, Ca, Sr, Ba; RE=La, Gd, hereinafter referred to as 2R5RE) were fabricated by the conventional melting and annealing method[2]. After deposition of Pd film of 500 nm^t on one side, the glass plate was placed on a molten Sn in a H_2 atmosphere, and applied the DC voltage of +35V to the Pd electrode at 340-380°C for 28 hrs. During the voltage application, the alkali ions more than 90% in the glass are replaced to protons and discharged into the molten Sn. The volatile elements from 2R5RE glass after APS were measured in N_2 atmosphere of ambient pressure under the heating rate of 80°C/h using a quadrupole mass spectrometer (QMS; BELMass, MicrotracBEL Corp.)

Figure 1 shows the QMS curves of each sample after APS. The desorption peaks of H_2O were clearly recognized above 450°C. As shown in figure 1, the 2Mg5La and 2Ba5Gd exhibited the higher resistivity against the H_2O desorption. Then we evaluated the prolonged proton conductivities for these samples. The measurement method was described in our last paper[2]. The measurement temperature was set at 310°C. Figure 2 represents the measurement results. Neither crystallization nor phase separation occurred longer than 500 h for 2Ma5La and 600 h for 2Ba5Gd. After these points, the phase separation accompanied with the precipitation of H_3PO_4 was caused in the samples[3]. Further extension of stable proton conductivity is expected by the improvement of glass composition.
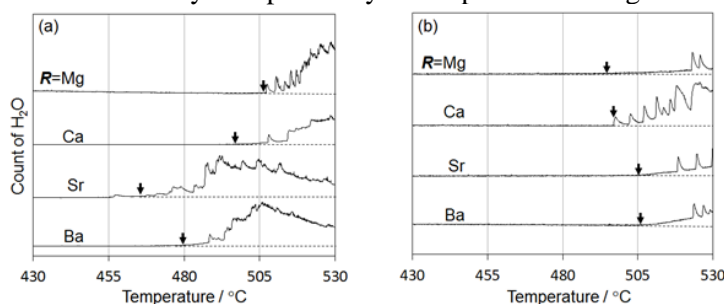

Fig.1 H_2O desorption curves of 2R5RE after APS; (a)La (b)Gd.
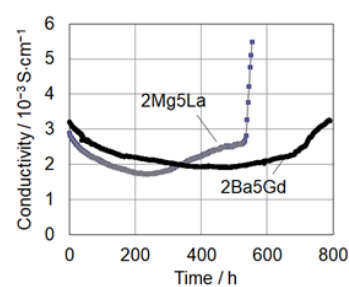
Fig.2 Prolonged proton conductivities for 2Mg5La and 2Ba5Gd after APS.

Reference
1. T. Ishiyama et al., J. Electrochem. Soc. 160 (2013) E143−E147. [2] T. Kinoshita et al. Appl. Surf. Sci. 428 (2018) 718–722. [3] K. Kawaguchi et al. Phys. Chem. Chem. Phys. 17 (2015) 22855–22861.

Junction Area and Bias Voltage Dependence of MR Ratio in $Ni_{78}Fe_{22}$/Mq$_3$ (M=Al, Er)/$Ni_{78}Fe_{22}$ Nanoscale Junction Devices Utilizing Magnetic Thin-film Edges

Yuma Sasaki[1,2], Robin Msiska[1,2], Takahiro Misawa[1], Sumito Mori[1], Takashi Komine[3], Norihisa Hoshino[4], Tomoyuki Akutagawa[4], Masaya Fujioka[1], Melbert Jeem[1], Madoka Ono[1,5], Junji Nishii[1], Hideo Kaiju[2,6]

[1]Research Institute for Electronic Science, Hokkaido University, Hokkaido 001-0020, Japan, [2]Faculty of Science and Technology, Keio University, Kanagawa 223-8522, Japan, [3]Graduate School of Science and Engineering, Ibaraki University, Ibaraki 316-8511, Japan, [4]Institute of Multidisciplinary Research for Advanced Materials, Tohoku University, Miyagi 980-8577, Japan, [5]Materials Integration Laboratories, AGC Inc., Kanagawa 221-8755, Japan, [6]Center for Spintronics Research Network, Keio University, Kanagawa 223-8522, Japan

Long spin coherent length in molecules, which realizes large magnetoresistance (MR) ratio, has attracted considerable interest in spintronics [1,2]. Recently, we have proposed nanoscale junction devices, which consist of molecules sandwiched between crossed edges of two magnetic thin films [3]. In this study, we fabricate $Ni_{78}Fe_{22}$/Mq$_3$ (M = Al, Er, q = 8-hydroxyquinolinato) /$Ni_{78}Fe_{22}$ junction devices and investigate electric and magnetic properties.

$Ni_{78}Fe_{22}$ (permalloy, Py in the following) thin films were deposited on low-softening-point (LSP) glass substrates using ion beam sputtering. Then, LSP glass substrates with the same composition were stacked on the fabricated Py films at 513°C and 0.25–1.0 MPa using the thermal pressing technique. The obtained samples were cut in half, and their cross-sectional surfaces were polished. Finally, an Mq$_3$ thin film with a thickness of 20 nm was spin-coated on the polished glass/Py/glass surface, and another glass/Py/glass sample was orthogonally stacked on the Mq$_3$ film with two Py edges crossed. The current-voltage characteristics and MR effect of the devices were evaluated by a four-probe method at room temperature.

Fig. 1 shows typical MR effects of (a) Py/Alq$_3$/Py and (b) Py/Erq$_3$/Py devices at room temperature. In the both cases of Py/Alq$_3$/Py and Py/Erq$_3$/Py devices, the bias voltage dependence of MR ratio agreed well with calculation results performed using Zhang's theory [4]. This means that spin flips mainly occur due to hot electrons in parallel magnetization of devices. Our theoretical and experimental works will provide new understanding on molecular spintronic devices.

Fig. 1 MR effect of (a) Py/Alq$_3$/Py and (b) Py/Erq$_3$/Py at room temperature.

References
1. C. Barraud et al., Nat. Phys. **6**, 615 (2010).
2. Z. H. Xiong et al., Nature **427**, 821 (2004).
3. H. Kaiju et al., J. Appl. Phys. **117**, 17C738 (2015).
4. S. Zhang et al., Phys. Rev. Lett. **79**, 3744 (1997).

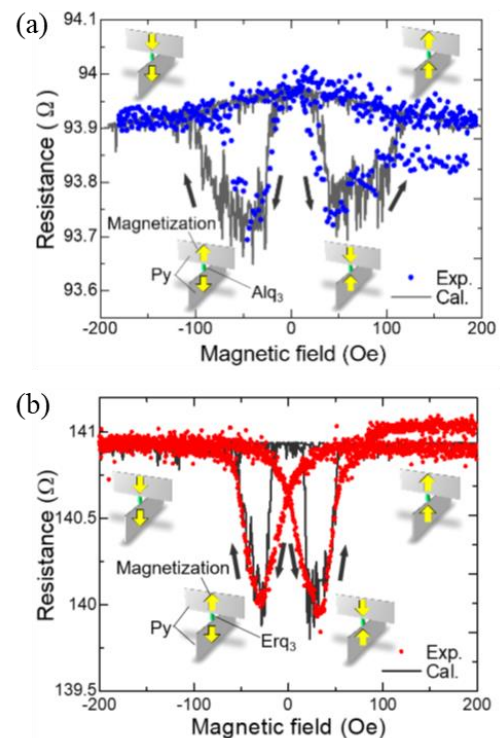# Synthesis, Structure, and Characterization of Dodecaazatrinaphthylene Derivatives

Qin Ji[1], Ichiro Hisaki[1,2], Kiyonori Takahashi[1,2], Takayoshi Nakamura[1,2]

[1]Graduate School of Environmental Science, Hokkaido University, N10W5, Sapporo, Hokkaido 060-810, and [2]Research Institute for Electronic Science, Hokkaido University, N20, W10, Sapporo, Hokkaido 001-0020, Japan

Organic porous frameworks composed of a two-dimensional network of a C_3-symmetric π-conjugated system can exhibit interesting physicochemical properties, such as selective gas sorption and storage, chemical luminescent sensors and optoelectronics. Furthermore, introducing N atoms into the π-conjugated gives the framework multiple active sites, which can interact and/or coordinate with cations species such as metal cations and proton to achieve external stimuli-responsive frameworks. Introduction of N atoms also is capable of fine-tuning of frontier orbital levels, which enables to control optoelectronic properties of the frameworks.
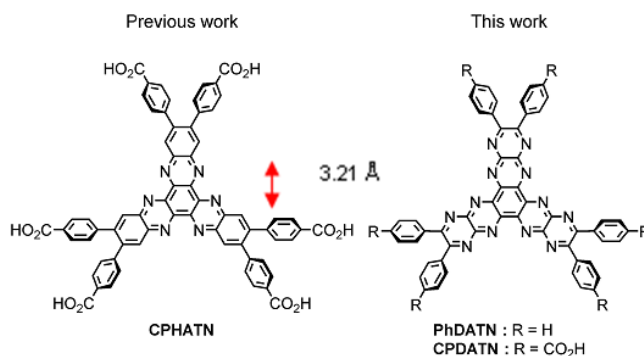

Fig. 1 Hexa- and dodeca-azatrinaphthylene derivatives (HATN and DATN, respectively).

In connection with this, we have synthesized N-contained C_3-symmetric π-conjugated systems such as a hexaazatrinaphthylene derivative (CPHATN) [Fig. 1(left)] and constructed the corresponding porous hydrogen-bonded organic frameworks (HOFs) responsive to acid.[1,2]

In this study, to construct dodecaazatrinaphthylene (CPDATN)-based HOFs, [Fig. 1(right) a phenyl derivative (PhDATN) was explored as a preliminary reference compound. PhDATN was successfully synthesized via condensation between the corresponding diamine derivative and triquinoyl. The structure was precisely revealed by single-crystalline X-ray diffraction analysis. PhDATN crystallize in the P-1 space group. Chloroform molecules used as a recrystallization solvent are included in the crystal. PhDATN forms a π-stacked dimer with interplanar distances between the stacked DATN cores of 3.21 Å (Fig. 2a). The DATN core has a twisted conformation due to packing force (torsion angle is 8.04°). The dimer is then packed without significant interaction between the cores as shown in Fig. 2b.
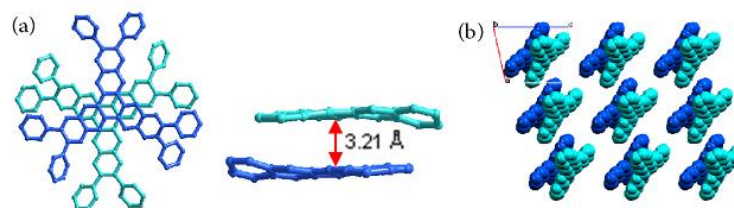
The present results indicate the feasibility of framework construction based on DATN, laying a foundation for further synthesis of CPDATN.

Fig. 2 a) Crystal structure of PhDATN dimer (left) and side view of the stacking (right). b) Packing diagram of the PhDATN dimers, where the peripheral phenyl groups are omitted for clarity.

References

1. I. Hisaki, Y. Suzuki, E. Gomez, B. Cohen, N. Tohnai, A. Douhal, *Angew. Chem., Int. Ed.,* **2018**, *57*, 12650−12655.
2. Hisaki, Y. Suzuki, E. Gomez, Q. Ji, N. Tohnai, T. Nakamura, A. Douhal, *J. Am. Chem. Soc.,* **2019**, *141*, 2111−2121.

Crystal Polymorphs and Physical Properties of (4-aminopyridinium)(dibenzo[24]crown-8)[Ni(dmit)$_2$]$^-$

Simin Li[1], Kiyonori Takahashi[1,2], Jiabing Wu[1], Ichiro Hisaki[1,2], and Takayoshi Nakamura[1,2]

[1]*Graduate School of Environmental Science, Hokkaido University, N10W5, Sapporo, Hokkaido 060-810, and* [2]*Research Institute for Electronic Science, Hokkaido University, N20, W10, Sapporo, Hokkaido 001-0020, Japan*

We report two supramolecular polymorphs which have the same formula (4-aminopyridinium)(DB[24]crown8)[Ni(dmit)$_2$](H$_2$O) （where DB[24]crown8= dibenzo-24-crown-8 and dmit^{2-} = 1,3-dithiole-2-thione-4,5-dithiolate） but different structure (Fig. 1). The dehydrated configuration of both cases can be obtained with the formula of (4- aminopyridinium)(DB[24]crown8)[Ni(dmit)$_2$].

Crystals were obtained by slow evaporation over a period of a few days, then washed with acetonitrile and methanol. Hydrated crystal **1** was obtained in a mixed solvent of acetonitrile : acetone = 6 : 1. Crystal **2** was synthesized in acetone solution by using the same proportion of raw materials. The dehydrated crystals almost maintain the structure configuration of hydrated crystals. In both hydrated crystals **1** and **2**, DB[24]crown8 formed a columnar structures, in which 4-aminopyridinium molecules were completely included and the columns were aligned in the *b* and *−a+c* axis, respectively. Amino group of 4-aminopyridinium was coordinated by oxygen atoms of DB[24]crown8. The pyridyl ring was parallel to the phenyl rings of DB[24]crown8 having chair configuration. In the crystal **1**, 4-aminopyridinium molecule was also coordinated by oxygen atoms of water molecules and disordered between two positions. [Ni(dmit)$_2$]$^-$ anions adopted two-dimensional layer structure. In the crystal **2**, 4-aminopyridinium molecules was ordered.

In both crystals **1** and **2**, [Ni(dmit)$_2$]$^-$ showed antiferromagnetic interaction in the temperature dependence of the magnetic susceptibility measurements. The Curie-Weiss model was applied to the crystal **1** with C = 0.378 emu K mol^{-1} and Θ = -19.6 K.
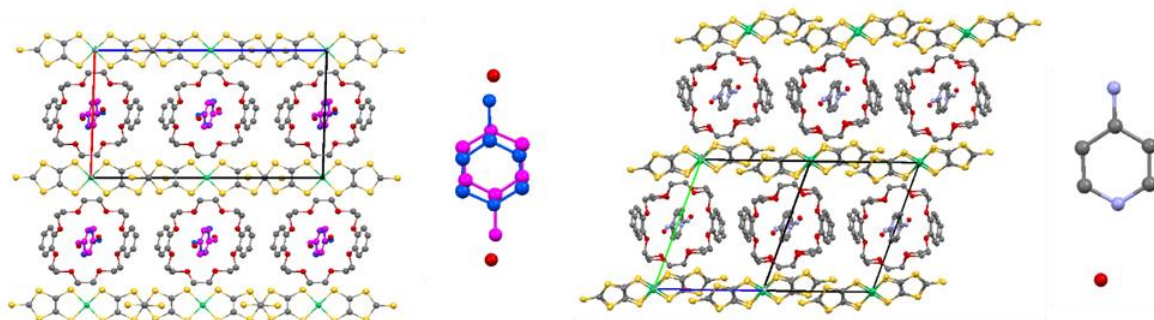

Fig. 1. Crystal structures and inorganic parts of hydrated polymorphs **1**(left) and **2**(right).

Reference
1. T. Akutagawa et al., *Nature Materials*, **2009**, 8, 342.

Interplay between Epidermal Stem Cell Dynamics and Dermal Deformation   P55

Yasuaki Kobayashi[1], Yusuke Yasugahira[2], Hiroyuki Kitahata[3], Mika Watanabe[4], Ken Natsuga[4], Masaharu Nagayama[1]

[1]Research Institute for Electronic Science, Hokkaido University, Sapporo, Japan,
[2]Graduate School of Science, Hokkaido University, Sapporo, Japan, [3]Department of Physics, Chiba University, Chiba, Japan, and [4]Department of Dermatology, Graduate School of Medicine, Hokkaido University, Sapporo, Japan

Tissue growth is a driving force of morphological changes in living systems. Whereas the buckling instability is known to play a crucial role for initiating spatial pattern formations in such growing systems, little is known about the rationale for succeeding morphological changes beyond this instability. In mammalian skin, the dermis has many protrusions toward the epidermis, and the epidermal stem cells are typically found on the tips of these protrusions. Although the initial instability may well be explained by the buckling involving the dermis and the basal layer, which contains proliferative cells, it does not dictate the direction of these protrusions, nor the spatial patterning of epidermal stem cells. Here we introduce a particle-based model of self-replicating cells on a deformable substrate composed of the dermis and the basement membrane and investigate the relationship between dermal deformation and epidermal stem cell pattering on it.

We performed numerical simulations of our model, starting with an initially flat basement membrane on which 64 stem cells were placed in a certain arrangement. As time evolves, TA cells are continually produced first by stem cells and then by themselves, spreading over the surface of the basement membrane and soon entirely cover it to form the basal layer, while the basement membrane starts to deform in the regions where it is covered with TA cells. Then many outward (upward in this case) protuberances are produced, which can be regarded as dermal protrusions. During this process, stem cells also spread over the basement membrane. Noticeably, stem cells tend to be located on the tips of the dermal protrusions. These observations show that our model reproduces basic features of the membrane shape and stem cell distributions observed in real skin.

The results of the previous section indicate that the strength of adhesion to the basement membrane is crucial for the observed patterns. Now the following argument explains why protuberances of the basement membrane direct outwards. Let us consider a small membrane segment on which cells are attached. When a cell division occurs and the surface of the segment becomes crowded, either a cell has to detach from the segment or the segment has to deform so that it can accommodate all attached cells, depending on the energy cost for detachment and deformation. If deformation is energetically more preferable than detachment, the resulting shape of the segment will be convex so as to minimize the stretching energy. Thus, from a local point of view every place has a tendency to create outward protuberances, resulting in dermal protrusions. This energetic argument also explains why stem cells prefer the tips of the dermal protrusions: Cells feel the stronger pressure to push them out of the basal layer in the concave regions such as the bottom of the basement membrane than in the convex regions such as the top, which means that the larger cost is required to remain in the basal layer in the former case. In such situations the total cost can be minimized when strongly bound cells such as stem cells occupy the top and TA cells fill the remaining space.

Reference
1. Y. Kobayashi et al., npj Comp. Mat. 4, 45 (2018)

Mathematical Model for the Epidermis P56

Kota Ohno[1]

[1]*Research Institute for Electric Science, Hokkaido University, N12W7, Kita-Ward*
Sapporo, Hokkaido

Skin is composed of epidermis, dermis and subcutaneous tissue. Especially, the epidermis is the boundary of the body from the environment and has some significant function for maintaining the life. The epidermis has the layer structure that is stratum basal (SB), spinosum (SS), granulosum (SG) and corneum (SC) (Fig. 1). The epidermal cells are produced at SB. These cells move to upper layer with differentiation into prickle cell and granular cell, become part of SC by cornification, and finally get removed from the surface. This turnover is occurred repeatedly and the period is about 45 days in human 1. Moreover, the epidermis has the barrier function. When the cells undergo cornification, lamellar bodies are secreted into intercellular space and their components form intercellular lipid that helps the barrier function in SC. This barrier has the role of water retentivity. In SG, there is tight junction barrier that control ion permeation. Even if the epidermis repeats turnover, the epidermis has the homeostasis, i.e., the layer structure and barrier function are not lost.

We study to understand this epidermal structure using mathematical model. Our model is considered particle-based model and we focused the calcium. Ca^{2+} was localized just under SC and calcium wave was propagated in epidermal cells when exposed to air 23. This implies the relationship between calcium signaling and the damage of the skin. From this reason, we consider the control from upper layer based on calcium dynamics. When the cells undergo cornification, we assumed that materials promoting the differentiation are produced and diffused into SG45. By this assumption, we observe the numerical result that have the homeostasis for layer structure (Fig. 1). Moreover, by considering intercellular dynamics and model for tight junction, we can consider the homeostasis for the barrier function. In this study, we will show the result applying our model to some skin disease.
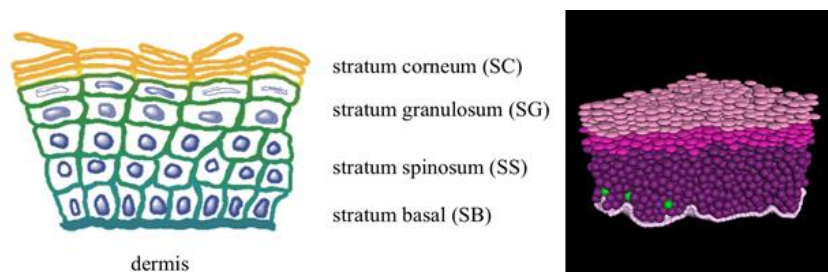

Fig. 1 (Left) Schematic illustration for the epidermal structure. (Right) The example of numerical simulation result with homeostasis. Each color indicates light-pink: corneum cell, dark-pink: granular cell and purple: prickle cell.

References
1. 清水宏, 新しい皮膚科学, 中山書店, (2018).
2. M. Denda, J. Hosoi, and Y. Asida, Biochem. Biophys. Res. Commun. 272, 134–137, (2000).
3. M. Denda, and S. Denda, Skin Res. Technol. 13, 195–201, (2007).
4. Y. Kobayashi, Y. Sanno, A. Sakai, Y. Sawabu, M. Tsutsumi, M. Goto, H. Kitahata, S. Nakata, J. Kumamoto, M. Denda, and M. Nagayama, PLoS ONE, 9(3) e92650, (2014).
5. Y. Kobayashi, Y. Sawabu, H. Kitahata, M. Denda, and M. Nagayama, Journal of Theoretical Biology, 397, 52-60, (2016)

Inverse Source Problems for Time-Fractional Evolution Equations   P57

Yikan Liu[1]

[1]*Research Institute for Electronic Science, Hokkaido University, N12, W7, Kita-Ward, Sapporo, Hokkaido 060-0812, Japan*

Within the last decade, evolution equations with fractional derivatives have gathered considerable attention among both theoretical and applied disciplines due to their feasibility in modeling physical processes such as anomalous diffusion. In this talk, we consider initial-boundary value problems for time-fractional diffusion(-wave) equations represented by

$$(\bigstar) \quad \begin{cases} (\partial_t^\alpha - \Delta)u(\boldsymbol{x},t) = F(\boldsymbol{x},t), & \boldsymbol{x} \in \Omega, 0 < t < T, \\ \begin{cases} u(\boldsymbol{x},0) = 0 & \text{if } 0 < \alpha \le 1, \\ u(\boldsymbol{x},0) = u(\boldsymbol{x},0) = 0 & \text{if } 1 < \alpha \le 2, \end{cases} & \boldsymbol{x} \in \Omega, \\ u(\boldsymbol{x},t) = 0, & \boldsymbol{x} \in \partial\Omega, 0 < t < T, \end{cases}$$

where ∂_t^α $(0 < \alpha \le 2)$ denotes the Caputo derivative. We investigate the following three inverse source problems (ISP) on determining some components in the inhomogeneous term F.

ISP-1 Provided that $F(\boldsymbol{x},t) = g(\boldsymbol{x})\rho(t)$ and ρ is known, determine the spatial component g by the partial interior observation of u in $\omega \times (0,T)$ $(\omega \Subset \Omega)$.

ISP-2 Provided that $F(\boldsymbol{x},t) = g(\boldsymbol{x})\rho(t)$ and g is known, determine the temporal component ρ by the single point observation of u at $\{\boldsymbol{x}^0\} \times (0,T)$ $(\boldsymbol{x}^0 \in \Omega)$.

ISP-3 Provided that $F(\boldsymbol{x},t) = g(\boldsymbol{x} - \boldsymbol{\gamma}(t))$ and g is known, determine the orbit $\boldsymbol{\gamma}$ by the multiple point observation of u at $\{\boldsymbol{x}^j\}_{j=1}^N \times (0,T)$ $(\boldsymbol{x}^j \in \Omega)$.

The starting point for all above problems is a fractional Duhamel's principle, which represents the solution to $(\bigstar)$ in form of a convolution

$$u(\boldsymbol{x},t) = \int_0^t D_t^{\lceil\alpha\rceil-\alpha} v(\boldsymbol{x},t;s)\mathrm{d}s, \quad 0 < t < T,$$

where $\lceil\alpha\rceil$ denotes the smallest integer larger or equal to α, D_t^β stands for the Riemann-Liouville derivative, and $v(\boldsymbol{x},t;s)$ satisfies the corresponding homogeneous equation with a parameter $s \in (0,T)$:

$$\begin{cases} (\partial_t^\alpha - \Delta)v(\boldsymbol{x},t;s) = 0, & \boldsymbol{x} \in \Omega, s < t < T, \\ \begin{cases} v(\boldsymbol{x},s;s) = F(\boldsymbol{x},s) & \text{if } 0 < \alpha \le 1, \\ v(\boldsymbol{x},s;s) = 0, \partial_t v(\boldsymbol{x},t;s)|_{t=s} = F(\boldsymbol{x},s) & \text{if } 1 < \alpha \le 2, \end{cases} & \boldsymbol{x} \in \Omega, \\ v(\boldsymbol{x},t;s) = 0, & \boldsymbol{x} \in \partial\Omega, s < t < T, \end{cases}$$

For ISP-1, we prove the uniqueness by utilizing a newly established weak unique continuation property. For ISP-2, the uniqueness and the stability of multiple logarithmic type follow from the applications of a strong maximum principle and a reverse convolution inequality, respectively. For Problem 3, we derive a Lipschitz stability estimate in the case of a localized moving source with the minimum possible observation points, and the uniqueness for the general case is verified with more observations.

References
1. G. Hu, Y. Liu, and M. Yamamoto, arXiv:1906.12014, **2019**.
2. D. Jiang, Z. Li, Y. Liu, and M. Yamamoto, *Inverse Problems*, **2017**, *33*, 055013.
3. Y. Liu, W. Rundell, and M. Yamamoto, *Fract. Calc. Appl. Anal.*, **2016**, *19*, 888−906.

Classification Bandit from the Numbers of Bad and Good Arms   P58
with Imperfect Loss Feedbacks

Koji Tabata,[1,3] Atsuyoshi Nakamura,[2] Tamiki Komatsuzaki[1,3]

[1]*Research Center of Mathematics for Social Creativity, Research Institute for Electronic Science Hokkaido University, N20, W10, Sapporo, Hokkaido 001-0020, and* [2]*Graduate School of Information Science and Technology, Hokkaido University, N14, W9, Sapporo, Hokkaido 060-0814, and* [3]*Institute for Chemical Reaction Design and Discovery, N21, W10, Japan*

In the area of inspections such as fault diagnosis of machines and pathological diagnosis, there is a demand for a task of determining whether the number of defective parts is more than a certain number. In our research, we especially treat the cases where we must spare several times of measurement to obtain the exact value for defectiveness of one part due to uncertainties such as noise. In this setting, by regarding parts to be check as arms in multi-armed bandit problem, the algorithm can be applied to the above tasks in order to minimize the number of required measurements.

The multi-armed bandit is an area of machine learning researches that solve dilemma of exploration and exploitation. The multi-armed bandit problem is frequently explained using multiple slot machines. Let's assume that there are 10 slot machines in front of a gambler, and he has 1000 coins and he can play one slot machine of them by one coin, so he can play 1000 times. Each machine, called as an arm in the term of multi-armed bandit, has its own fixed average reward distribution. The objective of multi-armed bandit problem is constructing the best strategy to maximize the rewards from slot machines. In order to maximize the cumulative reward, he has to estimate the best machine and play it (exploitation), but simultaneously has to play less-played machine to for better estimation of the best machine (exploration).

By defining the defective parts as the arm with expected reward higher than a given threshold, the measurement process can be formulated as multi-armed bandit setting. The algorithms to find the arm with expected reward higher than given threshold is proposed so far [1, 2, 3]. In our problem setting, there is no need to identify arms with higher expected reward than a threshold, but it is enough if there is more than a certain number. Murphy sampling [4] can decide only whether at least one arm with expected reward higher than a threshold.

In conventional research, it is assumed that the measured value is directly linked to the actual nature, and that the average rewards are expected to be show the presence or absence of abnormality correctly. In practice, however, this property is not always guaranteed, and false positives and false negatives are unavoidable due to the nature of the measurement.

Therefore, in this paper, we deal with the classification problem based on the number of arms whose expected reward is greater than or equal to the threshold when the misidentification is not 100%. While considering the limit of accuracy, we develop algorithm to decide whether there are m arms with higher expected reward than given threshold for given integer m with as few measurements as possible.

References
1. Andrea Locatelli, Maurilio Gutzeit, Alexandra Carpentier, "An optimal algorithm for the thresholding bandit problem", ICML, 2016.
2. Hideaki Kano, Junya Honda, Kentaro Sakamaki, Kentaro Matsuura, Atsuyoshi Nakamura and Masashi Sugiyama, "Good arm identification via bandit feedback", Machine Learning, **2019**, 108, 721-745.
3. Koji Tabata, Atsuyoshi Nakamura, Junya Honda and Tamiki Komatsuzaki, "A bad arm existence checking problem: How to utilize asymmetric problem structure?", Machine Learning, accepted for publication.
4. Emilie Kaufmann, Wouter M Koolen and Aurelien Garivier, "Sequential test for the lowest mean: From Thompson to Murphy sampling", Advances in Neural Information Processing Systems, **2018**, 6332-6342.

A Computational Method for Reaction Tubes based on Trajectory Calculation and Voronoi Tessellation

Mikoto Takigawa[1], Saki Miyashita[1],
Yuta Mizuno[2,3,4], Hiroshi Teramoto[2,3,5], Tamiki Komatsuzaki[2,3,4]

[1]*Department of Chemistry, Faculty of Science, Hokkaido University,*
[2]*Research Institute for Electronic Science, Hokkaido University,*
[3]*Institute for Chemical Reaction Design and Discovery, Hokkaido University,*
[4]*Graduate School of Chemical Sciences and Engineering, Hokkaido University,*
[5]*Department of Mathematics, Graduate School of Science, Hokkaido University*

In conventional chemical reaction theory, chemical reactions are assumed to proceed along the minimum energy pathway connecting the reactant and the product via a saddle point on the potential energy surface. The reaction rates are calculated from the energy at the saddle point, etc., according to transition state theories. This conventional framework has succeeded to elucidate mechanisms and kinetics of a lot of reactions in gas and condensed phases.

However, the conventional framework has the drawback that it neglects effects of molecular motions, i.e. dynamic effects. Recently, a lot of computational and experimental studies have reported chemical reactions that cannot be explained without considering dynamic effects, from textbook organic reactions to biological reactions. Thus, it is necessary to update chemical reaction theory so that we can elucidate mechanisms and kinetics of such dynamical chemical reactions.

Phase space geometry provides a mathematical basis for dynamical chemical reaction theory. A phase space is a space whose axes are positions and momenta of atoms. Molecular motions are represented by trajectories in the phase space of molecular systems. In the phase space of reaction systems, there are tube-like structures that divide the destiny of the trajectories[1]. All reactive trajectories going from the reactant to the product go through the inside of the tube. In this sense, the tubes correspond to dynamical reaction pathways. Considering these geometrical structures in the phase space, it is possible to construct reaction kinetic models including dynamical effects[1].

Although the concept of the reaction tube is mathematically clear and may be useful for chemistry, it is not straightforward especially for chemists to calculate reaction tubes due to complicated mathematics used in the conventional methods. Thus, we are developing a fast and accurate computational method for reaction tubes based on more intuitive techniques, that is, classical trajectory calculation and Voronoi tessellation which is a computational geometric method.

In this poster presentation, I will explain the details of our method and show numerical demonstrations for a model reaction system of two degrees of freedom.

Reference

1. N. De Leon *et al.*, *J. Chem. Phys.* **94**, 8310 (1991).

Physical Mechanisms Behind High Speed Jump of Nematode   P60
Caenorhabditis Elegans

Takuya Chiba[1] , T. Sugi[3] , Y. Nishigami[2] , T. Nakagaki[2] , K. Sato[2]

[1]Graduate School of Life Science, Hokkaido University, N10W8, Sapporo, 060-0811, Japan and [2]Research Institute for Electronic Science, Hokkaido University, N20W10, Sapporo, 001-0020, Japan, and [3]Molecular Neuroscience Research Center, Shiga University of Medical Science, Otsu, Shiga, 520-2192, Japan

The nematode *Caenorhabditis elegans* is a major model species that is used in a number of biological research. In the adult hermaphrodite, their total cell number is 959, and in the adult male, it is 1031. Moreover, the developmental fate of every single somatic cell has been mapped[1], [2].

The researches on behaviors of *C. elegans* also have beed carried out. For example, it is known that *C. elegans* shows chemotaxis and thermotaxis. When environmental conditions are stressed for them, (i.e., food insufficiency, excessive population density, or high temperature), *C. elegans* can become a stress-resistant life stage called the dauer stage. The dauer larva shows dauer characteristic behavior "nictation," in which they stand on their tails and wave their heads in the air[3]. This activity is thought to aid in attachment of the dauer larva to other organisms like insects.

Through the observation of this nictating behavior, our group found that *C. elegans* dauer larva jumps at a high speed. The measured jump speed is 1.11 ± 0.35 m/s. Considering that the length of the dauer larva is about 0.4 mm, it is an extremely high speed. Now we are attempting to reveal the high-speed jump mechanisms, how they can jump so fast while their body is so small.

In this research, we first attempted to measure the jump speed to characterize this jumping behavior. *C. elegans* shows two type jump, single worm jump, and multi worm jump. Single worm jump is a dominant jump, at which nematode jumps alone. At multi worm jump, some nematodes accompany jumping worm. The number of accompanying nematodes occasionally reaches one hundred. By utilize multi worm jump, we examined the relationship between the center of mass and jump speed of nematodes, in the different numbers of cells. Additionally, we also measured jump speed at different surface tension of surrounded water, which prevented the detachment between the nematode and a surface.
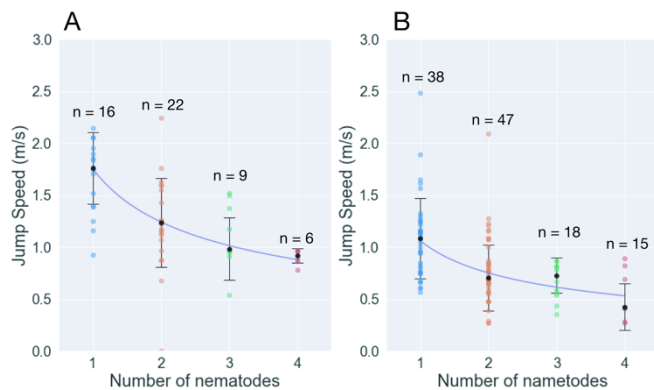

Figure 1 Relationship between number of jumping nematode and jump speed
A) Adding detergent, B) Only pure water

References
1. J. E. Sulston, E. Schierenberg, J. G. White, and J. N. Thomson, "The embryonic cell lineage of the nematode *Caenorhabditis elegans*," *Dev. Biol.*, vol. 100, no. 1, pp. 64–119, 1983.
2. J. Kimble and D. Hirsh, "The postembryonic cell lineages of the hermaphrodite and male gonads in *Caenorhabditis elegans*," *Dev. Biol.*, vol. 70, no. 2, pp. 396–417, 1979.
3. H. Lee *et al.*, "Nictation, a dispersal behavior of the nematode *Caenorhabditis elegans*, is regulated by IL2 neurons," *Nat. Neurosci.*, vol. 15, no. 1, pp. 107–112, 2012.

Asymmetric Patterns Appearing in Collective Photobehavior of *Chlamydomonas*

Kosuke Iizuka[1,2], Ken-ichi Wakabayashi[3], Ritsu Kamiya[4], Yukinori Nishigami[2], Toshiyuki Nakagaki[2], Katsuhiko Sato[2]

[1]*Graduate School of Life Science, Hokkaido University, N10W8, Sapporo 060-0810, and* [2]*Research Institute for Electronic Science, Hokkaido University, N20W10, Sapporo, Hokkaido 001-0020, and* [3]*Department of Life Science, Tokyo Institute of Technology, Nagatsuta-cho 4259, Midori-Ku, Yokohama 226-8501, and* [4]*Department of Biological Sciences, Faculty of Sciences and Engineering, Chuo University, 1-13-27 Kasuga, Bunkyo-ku, Tokyo 112-8551, Japan*

Chlamydomonas reinhardtii has been used as a model organism mainly for studies of photosynthesis and flagella. However, its collective motion has not been much investigated. It has been known that when irradiating a part of the *Chlamydomonas* cell suspension, cells aggregate at the edge of the irradiated region. We focused on such a collective photobehavior of *Chlamydomonas* cells and observed the aggregation pattern of cells when using some types of irradiation pattern. Then we found that cells show the left-right asymmetric aggregation pattern under some symmetric irradiation patterns (Fig. 1). To understand the mechanism underlying this phenomenon, we performed two experiments.

Fig. 1. Asymmetric aggregation patterns

The aggregation pattern of cells was obtained by irradiating the cell suspension from above with the halogen lamp through the specific type of irradiation mask. Irradiation time was about 1 minute. First, to check the effect of light irradiation angle on the asymmetry of the aggregation pattern, we observed the patterns by changing the irradiation angle. And we performed the image analysis of obtained pattern images to numerically check the asymmetry of patterns. Second, to check the behavior of individual cells during the pattern formation, we observed individual cells by using the inverted microscope. In the image analysis of those data, we automatically tracked the trajectory of cells and analyzed the swimming direction of cells.

Fig. 2. The effect of irradiation angle on the asymmetry of the aggregation pattern

As the result of the first experiment, the asymmetry of the aggregation pattern was increased with the increase of the light irradiation angle (Fig. 2). We can think that the increase of the irradiation angle enables cells to swim toward the bright area in higher degree, and this effect enhances the left-right asymmetry of the aggregation pattern. As the result of second experiment, there was the significant difference between the behavior of cells in the two types of dark area (Fig. 3). When the bright area existed on the left side, swimming direction of cells faced the bright-dark boundary in higher degree than when the bright area existed on the right side. From this result, we can think that cells tend to respond to the left bright area more easily than to the right bright area. *Chlamydomonas* cells are known to always rotate in the same direction during forward swimming, so individual cells have left-right asymmetry in their swimming. We think that the asymmetry of their swimming is an origin of the macroscopic asymmetric aggregation patterns. To clarify how the microscopic asymmetry of *Chlamydomonas* is related to the macroscopic asymmetry of their aggregation, we are now making a mathematical model that describes *Chlamydomonas*' swimming behavior and trying to extract the source of the left-right asymmetric patterns.
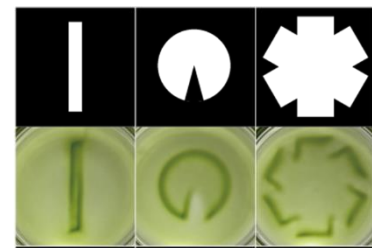

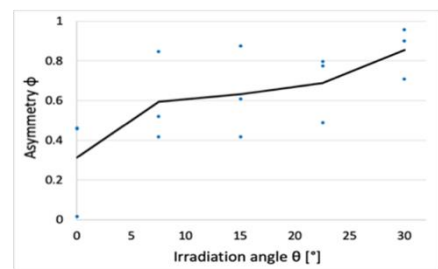Fig. 3. Difference of the cells' swimming direction between the two types of dark area

Semiconductor Single Photon Source with a Metal Reflector   P62

Satoru Odashima[1], Hirotaka Sasakura[2], Yasutaka Matsuo[1]

[1]Research Institute for Electronic Science, Hokkaido University, Sapporo 001-0020, Japan, [2]Division of Applied Physics, Hokkaido University, Sapporo 060-8628, Japan

The optical communication technology based on a single-photon is well expected from points of views of the downsizing and integration of devices, and highly secure quantum cryptography[1]. Among some candidates for a single photon source, the semiconductor quantum dots (QDs) are quite promising[2-5]. This is because the QD density and the photon energy are tunable, and present semiconductor technologies are available for fabricating suitable optical devices.

Fig. 1. (a) Schematic diagram of the sample structure. (b) Top view of the metal embedded pillar array.

In this research, we fabricate a semiconductor pillar array, in which each pillar contains a few numbers of InAs QDs. Those InAs QDs are grown by Molecular Beam Epitaxy (RIBER, MBE32P). A GaAs buffer layer of 300 nm and a subsequent GaAs of 170 nm are grown on GaAs (001) substrate at 600 ℃ and 565 ℃, respectively. InAs QDs are grown at 446 ℃, then covered by a GaAs of 200 nm at 565 ℃. A pillar array structure is fabricated by using electron beam lithography (ELIONIX, ELS-F125-U) with HSQ negative resist (Dow Corning Toray, Fox-15), and reactive ion etching (SAMCO, RIE-101iHS) with Cl_2/Ar gas. Pillars have a diameter of 300 nm, and the array has a square lattice structure with a lattice constant of 2.5 µm. Pillars are covered by SiO_2 of 100 nm by plasma CVD (SAMCO, PD-220ESN) and Ag of 1.5 µm by helicon plasma sputtering (ULVAC, MPS-4000C1/HC1),

then transferred to the Ag metal side by cleavage (Fig. 1). This metal embedded structure provides the directivity of photon flow, and possibly contributes to the high extraction efficiency of photons from the present InAs/GaAs QD array. Photoluminescence (PL) measurements are performed to this sample with a non-resonant excitation of 632 nm at 4.2K. Figure 2 shows the two examples of our trial PL measurements. The upper part of Fig. 2 shows the well-defined single peak at around 1,100 nm.

In conclusion, the metal embedded InAs/GaAs QD pillar array is prepared. The metal reflector in which pillars are embedded provides the directivity of photon flow. The present structure is promising as a single photon source and the metal embedded structure contribute to the high extraction efficiency of photons originating from QD. This work is supported by KAKENHI Grant Nos. 16H03817 and 17K06396.

Fig. 2. PL spectra of the metal embedded pillar with a non-resonant excitation of 632 nm at 4.2K.

References
1. N. Gisin, G. Ribordy, W. Tittel, and H. Zbinden, *Rev. Mod. Phys.,* **2002***, 74*, 145-195.
2. H. Kumano, H. Nakajima, H. Iijima, S. Odashima, Y. Matsuo, K. Ijiro, and I. Suemune, *Appl. Phys. Express*, **2013**, *6*, 062801-1/4.
3. H. Sasakura, X. Liu, S. Odashima, H. Kumano, S. Muto, and I. Suemune, *Appl. Phys. Express*, **2013**, *6*, 065203-1/3.
4. H. Sasakura, S. Muto, H. Kumano, *Appl. Phys. Express*, **2015**, *8*, 112002-1/4.
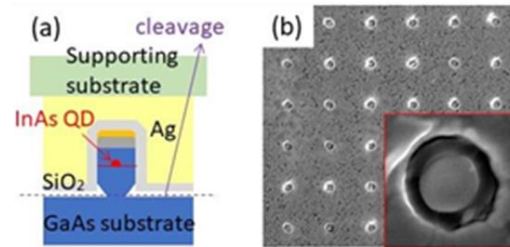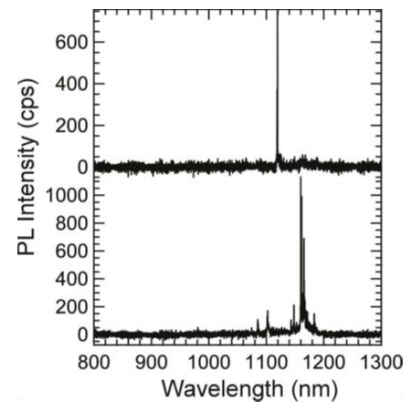5. S. Odashima, H. Sasakura, H. Nakajima, and H. Kumano, *J. Appl. Phys.*, **2017**, *122*, 223104-1/6.